

Ultrafast Quantum State Generation and Measurement in Nonlinear Nanophotonics

Thesis by
James Williams

In Partial Fulfillment of the Requirements for the
Degree of
Doctor of Philosophy

The logo for the California Institute of Technology (Caltech), featuring the word "Caltech" in a bold, orange, sans-serif font.

CALIFORNIA INSTITUTE OF TECHNOLOGY
Pasadena, California

2025
Defended February 18th, 2025

© 2025

James Williams

ORCID: 0000-0001-9073-5745

All rights reserved

ACKNOWLEDGEMENTS

My biggest acknowledgment goes out to my advisor, Prof. Alireza Marandi. Alireza was kind enough to let me mess around with FPGAs in his lab in the summer of 2019, and that led to a fruitful PhD. Alireza has always been very supportive of and patient with me, and most importantly has taught me how to do research, how to analyze the problem, and how to figure out what comes next. This has had a large impact on my personal and professional growth, and I am grateful for it. Prof. Axel Scherer has kindly allowed me to work in his lab and use his instruments, and has shared many valuable insights and ideas concerning relevant problems in my field. This advice has helped me contextualize my work and decide what to do next. Prof. Kerry Vahala and Prof. Mohammad Mirhosseini taught the classes that built my understanding of the nonlinear and quantum physics in my work. I often found myself referring to my notes from their classes when writing this thesis.

I would like to thank Elina Sendonaris for all of her mathematical insights and collaboration on the projects discussed in this thesis. Gordon Li, my labmate, office mate, roommate and most prolific collaborator in terms of number of papers, has always offered intriguing discussion and analysis of the work that we do and the broader implications it holds. I also thank Prof Rajveer Nehra. Raj put us on the path to success with his advice, and guided much of my experimental learning journey along with Robert Gray who's alignment help was a necessity for our experiments. I thank Prof Midya Parto for his technical and professional advice as well as the discussions we've had along the way. I thank Christian Leefmans for all his mentorship during my WAVE program and the time he took to explain the theory behind the experiments we were doing.

I have also had many interesting technical and non-technical discussions and collaborations with Thomas Zacharias, Nicolas Englebert, Benjamin Gutierrez, Rahul Chawlani, Selina Zhou, Ryoto Sekine, Maximillian Shen, Rithvik Ramesh, Mingchen Liu, Luis Costa, Arkadev Roy, Saman Jahani, Joon Hwang Bahng, Myoung-Gyun Suh, Arda Deger, Justin Widjaja, Shivam Mundhra and Jennifer Solgaard, all of whom I am grateful for. I also acknowledge the personal friendships I have shared with each and every one of you. The people I have had the pleasure of working with at Caltech have always been friendly and welcoming, and I feel quite lucky to have done my PhD in such a positive workplace environment.

Finally, I want to thank my family and friends who have provided nothing but unwavering emotional support along the way. Caltech is a mere 45 minute drive from where I grew up, and I have been fortunate to visit my mother, father, and grandmother quite often. They have always been by my side, and I could not have finished this degree without them. I dedicate this thesis to them.

Of course, no acknowledgment of mine would be complete without talking about the most important thing I did outside of my research: the Union. For a long time, students would complain about their working conditions. We would say "I should be paid more", or "I shouldn't be abused in my workplace", or "I should have enough time off to go renew my visa". And for a long time, the administration would say that "It's just not possible, we just can't do it because [insert vague and inscrutable reason here]". To address these challenges, the graduate students and postdoctoral scholars banded together and voted to form a labor union. Soon after, we learned that it was not in fact impossible to change things, it was just that we didn't have the political leverage to change them until now! Through our union, we've won better pay, better benefits, guaranteed time off for visa renewal, workplace protections, vacation days, and more. Working to build our union has had a fundamental impact on my world view, and I have become the person I am today because of lessons learned through this experience. I am forever grateful for it and for the wonderful and courageous people I met along the way who didn't just give up and go back to research when the going got tough, but instead stuck it out and fought the good fight. Two important themes stand out. First, we've established a formal system through which the students can use their power as a collective to demand and win change. Second, appeals within this system eventually end up in arbitration, which means that the administration is no longer the final decision maker. The administration understands this, and they will try to claw back these wins. They will try to undermine our power simply because their jobs would be easier if they didn't have to answer to the students and postdocs in a legally-binding framework. So to the students and postdocs at Caltech, I leave you with this advice. Protect your union, make sure that its leadership is strong and competent, and that the membership is engaged and understands what is at stake. Remain vigilant, and **don't squander the victories of the revolution.**

ABSTRACT

While many physical systems, including superconductors, trapped atoms, molecules, and acoustic resonators can process quantum information, photonics holds several fundamental advantages. Most photonics systems not only offer the convenience of room temperature operation but also shed the scalability limitations imposed by cryogenic and high vacuum environments. Integrated photonics has shrunk room-sized experiments to a chip-scale device while improving performance and versatility. Operating at optical frequencies offers information bandwidths orders of magnitude larger than what is achievable with microwave or trapped atom experiments.

In this thesis, we propose nanophotonic optical parametric amplifiers (OPAs) on a thin-film lithium niobate (TFLN) chip-scale platform for quantum information processing. Through dispersion-engineering, we achieve the distortion-free propagation of ultrafast pulses necessary for information clock rates above 1 THz. We investigate OPAs as ultrashort entangled pair sources and generate biphotons with a 165-fs temporal duration. We show that their generation efficiency and signal-to-noise performance is state-of-the-art at 2 μm and on-par with contemporary telecom-band sources. We explore OPAs as quantum measurement devices, and demonstrate all-optical single-photon level detection with a dead time of 75 fs. Finally, we show that OPAs can be used to recover continuous-variable quantum information by reconstructing the Wigner function of a 2.41 dB squeezed state encoded in a 154-fs pulse. This technique is loss-tolerant and offers a maximum clock speed of 6.5 THz. TFLN hosts a variety of high-performance optical devices including filters, modulators, resonators, III-V gain media, all of which are compatible with OPAs. Our results highlight ultrafast OPAs as the fundamental building blocks needed to realize large-scale circuits for all-optical quantum information processing.

PUBLISHED CONTENT AND CONTRIBUTIONS

- [1] Robert M Gray, Ryoto Sekina, Maximilian Shen, Thomas Zacharias, **James Williams**, Selina Zhou, Rahul Chawhani, Luis Ledezma, Nicolas Englebert, and Alireza Marandi. “Two-optical-cycle pulses from nanophotonic two-color soliton compression”. In: *arXiv preprint arXiv:2501.15381* (2025).
J.W. assisted with experiment design and setup.
- [2] **James Williams**, Elina Sendonaris, Rajveer Nehra, Robert Gray, Ryoto Sekine, Luis Ledezma, and Alireza Marandi. “Ultrafast All-Optical Measurement of Squeezed Vacuum in a Lithium Niobate Nanophotonic Circuit”. In: *arXiv preprint arXiv:2502.00518* (2025).
J.W. designed the experiment, derived the theory, collected and processed all data, and wrote the manuscript.
- [3] Gordon HY Li, Midya Parto, Jinhao Ge, Qing-Xin Ji, Maodong Gao, Yan Yu, **James Williams**, Robert M Gray, Christian R Leefmans, Nicolas Englebert, et al. “All-optical computing with beyond 100-GHz clock rates”. In: *arXiv preprint arXiv:2501.05756* (2025).
J.W. assisted with experiment design and setup.
- [4] Midya Parto, Christian Leefmans, **James Williams**, Robert M Gray, and Alireza Marandi. “Enhanced sensitivity via non-Hermitian topology”. In: *Light: Science & Applications* 14.1 (2025), p. 6.
J.W. assisted with experiment design and setup.
- [5] Midya Parto, Gordon Li, Ryoto Sekine, Robert Gray, Luis Ledezma, **James Williams**, Arkadev Roy, and Alireza Marandi. “Ultrafast neuromorphic computing with nanophotonic optical parametric oscillators”. In: *arXiv preprint arXiv:2501.15381* (2025).
J.W. assisted with experiment design and setup.
- [6] Thomas Zacharias, Robert Gray, Ryoto Sekine, **James Williams**, Selina Zhou, and Alireza Marandi. “Energy-Efficient Ultrashort-Pulse Characterization using Nanophotonic Parametric Amplification”. In: *arXiv preprint arXiv:2501.11152* (2025).
J.W. assisted with experiment design and setup.
- [7] **James Williams**, Rajveer Nehra, Elina Sendonaris, Luis Ledezma, Robert M Gray, Ryoto Sekine, and Alireza Marandi. “Ultrashort pulse biphoton source in lithium niobate nanophotonics at 2 μm ”. In: *Nanophotonics* 0 (2024).
J.W. designed the experiment, derived the theory, collected and processed all data, and wrote the manuscript.
- [8] Christian R Leefmans, Midya Parto, **James Williams**, Gordon HY Li, Avik Dutt, Franco Nori, and Alireza Marandi. “Topological temporally mode-

- locked laser”. In: *Nature Physics* (2024), pp. 1–7.
J.W. assisted with experiment design and setup.
- [9] Gordon HY Li, Christian R Leefmans, **James Williams**, Nicolas Englebert, Midya Parto, and Alireza Marandi. “All-Optical Recurrent Neural Network Using Ultrafast Nonlinear Optics”. In: *CLEO: Science and Innovations*. Optica Publishing Group. 2024, STu3P–6.
J.W. assisted with experiment design and setup.
- [10] Gordon HY Li, Christian R Leefmans, **James Williams**, Robert M Gray, Midya Parto, and Alireza Marandi. “Deep learning with photonic neural cellular automata”. In: *Light: Science & Applications* 13.1 (2024), p. 283.
J.W. assisted with experiment design and setup.
- [11] Shivam Mundhra, Elina Sendonaris, Robert M Gray, **James Williams**, and Alireza Marandi. “Optimizing for a Near Single-Mode Type-0 Optical Parametric Amplifier in Nanophotonics”. In: *arXiv preprint arXiv:2412.07004* (2024).
J.W. assisted with the theory and manuscript.
- [12] Midya Parto, Gordon HY Li, Ryoto Sekine, Robert M Gray, Luis L Ledezma, **James Williams**, and Alireza Marandi. “An Optical Neural Network Based on Nanophotonic Optical Parametric Oscillators”. In: *CLEO: Science and Innovations*. Optica Publishing Group. 2024, STu3P–7.
J.W. assisted with experiment design and setup.
- [13] Elina Sendonaris, **James Williams**, Rajveer Nehra, Robert Gray, Ryoto Sekine, Luis Ledezma, and Alireza Marandi. “Ultrafast single-photon detection using nanophotonic parametric amplifiers”. In: *arXiv preprint arXiv:2410.18397* (2024).
J.W. designed and build the experment, and collected the data.
- [14] Thomas Zacharias, Robert Gray, **James Williams**, Luis Ledezma, and Alireza Marandi. “Femtosecond Pulse Characterization using Nanophotonic Parametric Amplification”. In: *2024 Conference on Lasers and Electro-Optics (CLEO)*. IEEE. 2024, pp. 1–2.
J.W. assisted with experiment design and setup.
- [15] Qiushi Guo, Benjamin K Gutierrez, Ryoto Sekine, Robert M Gray, **James Williams** A, Luis Ledezma, Luis Costa, Arkadev Roy, Selina Zhou, Mingchen Liu, et al. “Ultrafast mode-locked laser in nanophotonic lithium niobate”. In: *Science* 382.6671 (2023), pp. 708–713.
J.W. assisted with automation of data collection.
- [16] Qiushi Guo, Ryoto Sekine, **James Williams** A, Benjamin Gutierrez, Robert M Gray, Luis Ledezma, Luis Costa, Selina Zhou, and Alireza Marandi. “Actively mode-locked laser in nanophotonic lithium niobate”. In: *CLEO: Science and Innovations*. Optica Publishing Group. 2023, SF1K–3.
J.W. assisted with automation of data collection.

- [17] **James Williams**, Rajveer Nehra, Elina Sendonaris, Luis Ledezma, Robert M Gray, Ryoto Sekine, and Alireza Marandi. “High Brightness Broadband Photon-Pairs at $2\ \mu\text{m}$ in Lithium Niobate Nanophotonics”. In: *2023 Conference on Lasers and Electro-Optics (CLEO)*. IEEE. 2023, pp. 1–2.
J.W. designed the experiment, derived the theory, collected and processed all data, and wrote the manuscript.
- [18] Christian Leefmans, Nicolas Englebert, **James Williams**, Nathan Goldman, Simon-Pierre Gorza, Alireza Marandi, et al. “Dissipative Cavity Solitons at the Boundaries of a Topological Lattice”. In: *CLEO: Fundamental Science*. Optica Publishing Group. 2023, FM2B–7.
J.W. assisted with experiment design and setup.
- [19] Christian R Leefmans, Nicolas Englebert, **James Williams**, Robert M Gray, Nathan Goldman, Simon-Pierre Gorza, François Leo, and Alireza Marandi. “Cavity Soliton-Induced Topological Edge States”. In: *arXiv preprint arXiv:2311.04873* (2023).
J.W. assisted with experiment design and setup.
- [20] Gordon HY Li, Christian R Leefmans, **James Williams**, Robert M Gray, Midya Parto, and Alireza Marandi. “Photonic Neural Cellular Automata for Self-Organized Image Classification”. In: *2023 Conference on Lasers and Electro-Optics (CLEO)*. IEEE. 2023, pp. 1–2.
J.W. assisted with experiment design and setup.
- [21] Gordon HY Li, Christian R Leefmans, **James Williams**, and Alireza Marandi. “Photonic elementary cellular automata for simulation of complex phenomena”. In: *Light: Science & Applications* 12.1 (2023), p. 132.
J.W. assisted with experiment design and setup.
- [22] Midya Parto, Christian Leefmans, **James Williams**, and Alireza Marandi. “Non-Hermitian Topologically Enhanced Sensing”. In: *CLEO: Fundamental Science*. Optica Publishing Group. 2023, FM4B–4.
J.W. assisted with experiment design and setup.
- [23] Midya Parto, Christian Leefmans, **James Williams**, Franco Nori, and Alireza Marandi. “Non-Abelian effects in dissipative photonic topological lattices”. In: *Nature Communications* 14.1 (2023), p. 1440.
J.W. assisted with experiment design and setup.
- [24] Elina Sendonaris, Rajveer Nehra, **James Williams**, Robert Gray, Luis Ledezma, Ryoto Sekine, and Alireza Marandi. “Toward Single Photon Detection using Nanophotonic Parametric Amplifiers”. In: *CLEO: Fundamental Science*. Optica Publishing Group. 2023, FTh3A–5.
J.W. assisted with experiment design and setup.
- [25] Christian Leefmans, Avik Dutt, **James Williams**, Luqi Yuan, Midya Parto, Franco Nori, Shanhui Fan, and Alireza Marandi. “Topological dissipation in a time-multiplexed photonic resonator network”. In: *Nature Physics* 18.4

(2022), pp. 442–449.

J.W. assisted with experiment design and setup.

- [26] Christian Leefmans, Midya Parto, **James Williams**, Avik Dutt, Franco Nori, and Alireza Marandi. “Topological Mode-Locked Laser with Intracavity Couplings”. In: *CLEO: QELS_Fundamental Science*. Optica Publishing Group. 2022, FTu5J–2.
J.W. assisted with experiment design and setup.
- [27] Midya Parto, Christian Leefmans, **James Williams**, Franco Nori, and Alireza Marandi. “Measuring Topological Invariants within Dissipatively-Coupled Lattices”. In: *CLEO: QELS_Fundamental Science*. Optica Publishing Group. 2022, FTu4J–1.
J.W. assisted with experiment design and setup.
- [28] Anna Soper, Christian Leefmans, Midya Parto, **James Williams**, and Alireza Marandi. “Experimental realization of a 64th order exceptional point on a time-multiplexed photonic resonator network”. In: *Optical and Quantum Sensing and Precision Metrology II*. SPIE. 2022, PC1201619.
J.W. assisted with experiment design and setup.
- [29] Christian Leefmans, Avik Dutt, **James Williams**, Luqi Yuan, Shanhui Fan, and Alireza Marandi. “Topological Behaviors in Networks of Time-Multiplexed Optical Resonators”. In: *CLEO: QELS_Fundamental Science*. Optica Publishing Group. 2020, FW3A–3.
J.W. assisted with experiment design and setup.

TABLE OF CONTENTS

Acknowledgements	iii
Abstract	v
Published Content and Contributions	vi
Table of Contents	ix
List of Illustrations	xii
List of Tables	xviii
Nomenclature	xix
Chapter I: Introduction	1
1.1 Quantum Advantage	1
1.2 Lithium Niobate Nanophotonics	2
1.3 Ultrafast Computing and Dispersion Engineering	2
1.4 Optical Parametric Amplifiers	3
Chapter II: A Very Brief Introduction to Quantum Optics	9
2.1 A Quantum Description of the Electromagnetic Field	9
2.2 Quadratures and Continuous Variable Quantum Optics	10
2.3 Defining Quantum Ultrafast Pulses	12
2.4 The $\chi^{(2)}$ Nonlinearity and Hamiltonian	12
2.5 Multimode Quantum Optics	13
Chapter III: Spectrotemporal Modes	16
3.1 Mode Structure	16
3.2 Continuous Variable Cluster States from Parametric Oscillators	16
3.3 Parametric Amplifiers as Sources of Quantum Light	18
Chapter IV: Ultrashort pulse biphoton source in lithium niobate nanophotonics at 2 micron	26
Abstract	27
4.1 Introduction	28
Biphoton Generation from OPAs	30
Device Design and Fabrication	32
4.2 Spectrotemporal Modes	34
4.3 Determining Losses via Parametric Generation	35
4.4 Experimental Setup	37
4.5 Measurement and Data Processing	38
4.6 Comparison and Discussion	42
Detailed Comparison Table	44
4.7 Conclusion	46
4.8 Acknowledgments and Disclosures	46
Chapter V: Ultrafast single-photon detection using nanophotonic parametric amplifiers	54
Abstract	55

5.1	Main	56
5.2	Conclusion	64
5.3	Methods	64
	Experimental setup	64
	Quantum detector tomography	65
	Homodyne OPAD	66
5.4	Data availability	67
5.5	Code availability	67
5.6	OPAD POVM	67
5.7	Chip dimensions and characterization	68
	Extracting g/κ from OPG measurements	69
5.8	High-gain OPA simulations	71
5.9	Detector tomography regularization constant	72
5.10	Acknowledgments	72
5.11	Author information	73
	Contributions	73
5.12	Ethics declarations	74
	Competing interests	74
Chapter VI: Ultrafast All-Optical Measurement of Squeezed Vacuum in a Lithium Niobate Nanophotonic Circuit		81
Abstract		82
6.1	Introduction	83
6.2	Parametric Amplifiers as Quantum Measurement Devices	84
	Quadrature Measurement	85
	Multimode Cascaded Squeezing in the Heisenberg picture	87
	Dispersion Engineering	90
	Calculation of the Joint Spectral Intensity and its Modes	92
	Pump Depletion	93
	Pump Depletion in Simulation	94
	Pump Depletion and Multimode Amplification in Experiment	94
6.3	Experimental Setup	96
6.4	Data Analysis	97
	Shot-noise Calibration	97
	Slow Photodetector Measurements	98
	Pulse-to-pulse Measurements	100
6.5	Conclusion	102
6.6	Acknowledgements	103
Chapter VII: Outlook		108
7.1	Challenges with TFLN and the Future of Nonlinear Photonics	108
7.2	Lifting the Electronic Bandwidth	109

LIST OF ILLUSTRATIONS

<i>Number</i>	<i>Page</i>
2.1 A) A schematic of homodyne detection with a as the measured field and b as the local oscillator. B) A phasor diagram plotting a with respect to the quadratures of b	10
2.2 A) The energy conservation of the pump laser plotted as a function of the signal and idler frequencies. This is for a 75-fs transform-limited mode locked laser centered at 1045nm. B) The phase matching condition of a thin-film periodically poled lithium niobate waveguide in the type-0 configuration. The waveguide design can be found in [1]. Yellow areas are where parametric down-conversion from a pump photon to a signal and idler photon are supported. C) The joint spectral intensity function computed as the product of the pump and phase matching. D) A plot of the mode occupancy vs mode number of the JSI in panel C. E) Plots of the first 6 modes composing the JSI.	14
4.1 A diagram of the source operation. Femtosecond pump pulses are injected into a dispersion-engineered periodically poled lithium niobate (PPLN) waveguide to produce an ultrafast photon pair via type-0 spontaneous parametric down-conversion (SPDC). A) An illustration of the SPDC process used to generate photon pairs. B) 2-photon microscopy image of the poled region and an SEM of a representative device. C) The theoretical and measured SPDC spectra.	30
4.2 A) The quasi-TE waveguide mode for pump light at 1.045 μm . Arrows at the top right denote the ordinary and extraordinary material axes. B) The quasi-TE waveguide mode for signal light at 2.09 μm . C) Dispersion profile for the pump wavelength. D) Dispersion profile for the signal wavelength. E) Group velocity mismatch at different signal wavelengths relative to 1.045 μm	33
4.3 A plot of the average number of photons per pulse vs input pump power.	36

4.4	A) The experimental setup used to characterize the source. MLL is a 250-MHz 75-fs mode-locked laser centered at 1.045 μm . HWP is a half-wave plate. PBS is a polarizing beam splitter. VND is a variable neutral density filter. Obj is a reflective objective. FC is a freespace to fiber coupler. LP is a low-pass filter. BP is a band-pass filter. SNSPDs are superconducting nanowire single photon detectors. 50/50 are balanced fiber beamsplitters. H, S, and I denote the heralding, signal, and idler channels respectively. B) Measurement setup for performing the Hanbury Brown-Twiss (HBT) experiment. C) Measurement setup for determining $g_H^{(2)}(0)$. The SEM image inset is of a representative device [37].	37
4.5	A) Example histogram from an HBT experiment taken at 11 μW of on-chip pump power. The main coincidence peak, caused by the detection of a signal/idler pair from the same generation event, is centered at 0-ns delay while accidentals peaks, caused by signal and idler photons created from consecutive and hence uncorrelated generation events, are present to the left and right at ± 4 ns. B) Count rates for the signal and idler channels compared with the fitted linear model.	38
4.6	A) Coincidence-to-accidentals ratio (CAR) as a function of on-chip pump power. The fitted model is taken from [19]. B) On-chip pair generation rate as a function of on-chip pump power. This is the rate of pair generation at the output of the poled region of the waveguide. Pump input coupling losses are calculated based on a parametric gain measurement detailed in the supplementary.	39
4.7	Heralded $g_H^{(2)}(0)$ of our source as a function of on-chip pump power. .	42
4.8	A comparison plot of relevant photon pair sources. Horizontal error bars represent the reported source bandwidth. Data for efficiency, wavelength, and bandwidth are taken from [12, 16, 14, 61] are PPLN ridge waveguides, similar to our device. [13, 62, 63] are larger ($>1\text{-}\mu\text{m}$ tall) PPLN waveguides. [19] is a bulk PPLN crystal. [22] is a bulk AlGaS2 crystal. [18] is a nanophotonic AlN ring resonator. [64] is a bulk LBO crystal. [65] is an InGaP ring resonator.	43

- 5.1 Detecting single photons with an OPA and a macroscopic detector. (a) The concept of the single photon OPAD. A microscopic quantum state is amplified in a waveguide OPA to levels detectable by a macroscopic detector. A threshold is applied to the detected pulse to categorize the signal as single photon or vacuum. (b) Photocurrent distribution from a photodetector when the input to the OPA is vacuum (dark blue) or a single photon (red). An example click threshold is shown. (c) Pump homodyne result distribution of vacuum (dark blue) and a single photon (red) as a function of the homodyne measurement result of the pump's squeezed quadrature. Inset: schematic of the homodyne detection scheme. (d) Efficiency and dark count rate as a function of photocurrent threshold. The specific threshold is dependent on the OPA gain and photodetector, and thus is left unlabeled. (e) Efficiency and dark count rate as a function of lower homodyne result threshold, with an upper threshold of 2. 58
- 5.2 Experimental quantum tomography of an OPA-based detector. (a) Experimental setup for quantum tomography, including Wigner functions of the generated coherent and coherent squeezed states (not to scale). BPF: band-pass filter; LPF: low-pass filter; PD: photodetector; FC: fiber coupler; OSA: optical spectrum analyzer. (b) Average photocurrent of pulses as a function of coherent state angle. Shaded regions indicate the standard deviation of the pulses' photocurrent distribution. (c) Histogram of the pulse photocurrents for amplified and de-amplified coherent states and vacuum. 60
- 5.3 Detector tomography results and analysis. (a) The POVM elements of the OPAD, reconstructed through detector tomography (first and second rows) and theoretically calculated using QuTiP (third row). The theoretical POVM elements are real. (b) Experimentally reconstructed Wigner functions of the no click and click POVM elements. (c) The efficiency and dark count rate of the detector for both experimentally reconstructed and theoretically calculated POVMs as a function of the threshold photocurrent or photon number. (d) The fidelity with a single photon state after one mode of the Bell state $(|00\rangle + |11\rangle)/\sqrt{2}$ is measured with an OPAD vs. the threshold photocurrent or photon number, for both experimental and theoretical POVMs. Inset: diagram of the measurement scheme. 61

5.4	Using a pump homodyne OPAD to create a kitten state. (a) Diagram of the scheme. The first OPA creates squeezed vacuum and the second OPA is followed by a homodyne measurement on the depleted pump, triggering a click. The Wigner function of the kitten state is shown on the upper right. (b) The detection probability as a function of the pump homodyne measurement result, with the detection window considered to create the kitten state shaded.	63
5.5	OPG power as a function of pump power. We use a subset of the data which is in the undepleted pump regime and also has a high enough power to clear the electronic noise floor of the detector, shown in blue. The average power is shown as the green line for illustration purposes. The fit equation with the parameters we found is shown in red.	70
5.6	The performance of OPAs with different levels of gain. (a) The efficiency vs. dark count rate of OPADs with OPAs with various levels of gain with Gaussian noise proportional to the gain. The points were generated by sweeping the threshold photon number. (b) Click probability vs. OPA gain for vacuum, single photon, and an $\langle N \rangle = 1$ coherent state, for vacuum click probability (dark count rate) of 2.5%. Note the constant click probabilities over a wide amplification range.	72
5.7	A plot of dark count rate and efficiency as a function of the regularization constant γ	73
6.1	A) Layout of the measurement procedure. Δt represents the relative time-delay between the pump and squeezed vacuum generated on-chip where a 0.775 fs delay corresponds to a measurement phase of $\phi = \frac{\pi}{2}$. B) Measured photon number distributions for squeezing ($\phi = \frac{\pi}{2}$), anti-squeezing ($\phi = 0$) and vacuum. C) Wigner function recovered for vacuum. D) Wigner function recovered for squeezed vacuum.	83
6.2	A) Pump dispersion and group-velocity mismatch (calculated at degeneracy and plotted at the pump wavelength) for our OPA. B) Signal dispersion vs wavelength. C) Parametric generation (vacuum amplification) spectra of our measurement and squeezer OPAs.	85
6.3	A diagram of the squeezer and measurement OPA circuit.	87

6.4	A) Joint-spectral intensity function of the squeezed vacuum produced by our OPA. B) The first four modes of the JSI calculated via the Bloch-Messiah decomposition. C) Plot of the mode number vs proportion of mode present in the JSI.	89
6.5	A) Signal spatial mode within our waveguide. Text on the right denotes the material stack-up with air, poly methyl methacrylate (PMMA), lithium niobate (LN) and silicon dioxide (SiO ₂). Dimensions are indicated by the vertical and horizontal measurements. The ordinary and extraordinary crystal axes are denoted at the top right. B) Pump spatial mode. C) OPA gain versus measurement pump energy. Error bars are calculated from pump and signal coupling stability measurements taken before gain measurements. The depleted pump theory is taken from the Gaussian limit defined in [38].	91
6.6	A) Simulated photon number distributions for unfiltered detection across different pump energies. B) Simulated photon number distributions for 20-nm bandpass filtered detection across different pump energies. C) A plot of the remaining pump energy after pulse propagation (lower remaining energy is a more depleted pump), and the peak histogram bin for the unfiltered and filtered simulations.	92
6.7	A) Photon number distributions for a 2-mm OPA with no filtering. B) Photon number distributions for a 2-mm OPA with bandpass filtering. C) Photon number distributions for a 5-mm OPA with no filtering. D) Photon number distributions for a 5-mm OPA with bandpass filtering. E) Mode number vs measurement (input) pulse energy for the 4 cases shown above as well as the measurement OPA used for tomography.	95
6.8	Experimental setup. MLL: Titanium:sapphire tunable mode-locked laser. PBS: polarizing beamsplitter. VND: variable neutral density filter. SH: mechanical shutter. Obj: reflective objective. FC: reflective fiber collimator. LP and SP: long-pass and short-pass wavelength filters. 90/10: fiber splitter with 90% going to the fast detector and 10% going to the slow detector. PD: photodetector. Fast Osc: 80 GSPS 40 GHz oscilloscope. Slow Osc: 100 MSPS 10 MHz oscilloscope.	96

- 6.9 A) Squeezing measurement taken on the OSA. The black curve is the amplification fringe produced from squeezed vacuum amplified in the measurement OPA. The grey curve is the baseline shot noise at the pump power used to measure the black curve. The red and blue curves are the corrected shot-noise levels to account for pump interference in the measurement OPA. B) Variance relative to vacuum vs squeezer pulse energy with a measurement pulse energy of 30 pJ. C) Variance relative to vacuum vs measurement pulse energy. Error bars are calculated from shot-noise variations during each measurement. 98
- 6.10 A) Sample photon number distributions from fast measurements at different ϕ . Red points are data, and the blue curve is a 2-mode fit. B) Photon number variance vs ϕ for slow, fast (pulse-to-pulse) measurements and the 1st mode of a 2-mode fit. Solid lines are the expected cosine dependence taken from [30]. C) Recovered squeezed vacuum Wigner function. Solid and dashed white lines lie along the $1/(e\pi)$ contours. D) Expected density matrix (ρ) based on measured squeezing and anti-squeezing. E) Recovered ρ . F) Absolute difference between expected and recovered ρ 101
- 7.1 A demultiplexing circuit used to transition from a clock rate f to a clock rate $\frac{f}{N}$ 109

LIST OF TABLES

<i>Number</i>		<i>Page</i>
4.1	x = did not report. † = estimated based on reported data. * = units of per mW^2	45

NOMENCLATURE

- GVD.** Group velocity dispersion.
- GVM.** Group velocity mismatch.
- ICP-RIE.** Inductively coupled plasma reactive ion etching.
- OPA.** Optical parametric amplifier.
- OPG.** Optical parametric generation.
- OPO.** Optical parametric oscillator.
- PMMA.** Poly(methyl methacrylate).
- PND.** Photon number distribution.
- PNR.** Photon number resolving.
- POVM.** Positive operator valued measure.
- SFG.** Sum Frequency Generation.
- SHG.** Second harmonic generation.
- SPDC.** Spontaneous parametric down-conversion.
- SV.** Squeezed vacuum.
- TFLN.** Thin-film lithium niobate.

Chapter 1

INTRODUCTION

"If you think you understand quantum mechanics, you don't understand quantum mechanics." - Richard Feynman

1.1 Quantum Advantage

Understanding and engineering quantum phenomena can create performance advantages unattainable through classical means in three key fields: communication, sensing, and computing [1, 2, 3]. In quantum key distribution (QKD), measurements of the entanglement between two or more systems verify the security of a communications channel and can detect the pretense of eavesdroppers. The quantization of the magnetic field underpins the operation of highly-sensitive SQUID detectors [4] while quantum tunneling of electrons can image individual atoms [5]. Universal quantum computing has been realized across many physical platforms including superconducting qubits [6] and trapped atoms [7].

We investigate quantum advantage in the context of continuous-variable quantum optics with a focus on states generated by spontaneous-parametric down-conversion (SPDC) such as squeezed vacuum (SV) and biphotons. SV is a quantum state in which the noise in one field quadrature is compressed below the shot-noise limit. This allows for optical measurements which exceed the noise limits imposed by quantum mechanics. SV has most famously been used to extend the range of the LIGO experiments by lowering the noise floor of the large interferometers used to measure gravitational waves [8]. Independent pulses of squeezed light can be interfered to create large-scale entanglement known as a cluster state. These states, along with non-Gaussian measurements, can be realized in fiber-based systems and used to build a universal quantum computer [9, 10]. Biphotons are pairs of entangled photons created through SPDC whose non-classical correlations can be leveraged to achieve quantum advantage. By measuring these correlations, entangled pairs can offer increased sensitivity in interferometric [11] and spectroscopic measurements [12, 13]. Similar to SV, multiple biphoton sources have been used to create a quantum computational advantage [14].

1.2 Lithium Niobate Nanophotonics

Integrated photonics has proved to be a promising quantum information processing platform for several reasons. First, the room temperature operation enjoyed by most platforms greatly simplifies system complexity and allows for more rapid scaling of computational power compared to superconducting systems requiring cryogenic temperatures or trapped-atom systems requiring high vacuum environments. Platforms such as thin-film lithium niobate (TFLN) exhibit a large second-order optical nonlinearity ($\chi^{(2)}$), a necessary ingredient to manipulate and measure quantum information, as well as ferroelectric domains which support poling [15]. Poling enables the phase-matching necessary for efficient nonlinear conversion in integrated waveguides. Conversion efficiency can be increased further through the use of ridge waveguides which increase intensity as well as mode overlap [16]. These properties have enabled the creation of nonlinear waveguides with record-breaking interaction strengths [17].

TFLN can also host a variety of other high-performance optical devices [18]. Its strong electro-optic effect has been used to implement optical modulators with bandwidths beyond 100 GHz [19]. Low-loss ridge waveguides have enabled resonators with Q factors exceeding 10^8 [20]. These resonators can be used to build a range of useful circuits including wavelength filters and soliton microcombs [21]. Significant progress has been made in integrating short pulse sources on chip, especially in LN nanophotonics, with a 4.8-ps 10-GHz chip-scale mode-locked laser demonstrated in [22] and a chip-scale electro-optic comb source with a 520-fs duration and a 30-GHz repetition rate demonstrated in [23]. Heterogeneous integration has brought additional optically useful materials to TFLN including III-V gain media [24] and quantum dots [25]. Such a library of passive and active devices capable of being integrated into a single monolithic platform has made TFLN an attractive solution for creating large-scale nonlinear and quantum circuits.

1.3 Ultrafast Computing and Dispersion Engineering

For information processing in the optical domain, time-multiplexing is a technique commonly deployed to increase computational speed and volume through the use of pulsed light. Each pulse stores information, and time-multiplexed architectures take advantage of these pulses by packing them tightly together in the time domain to scale up system size. Shorter pulses translate to a denser encoding and hence a higher effective clock rate. Pulses are often used to represent nodes in fiber-based optical computers and reduce the number of fiber components needed in exchange for time

complexity [26, 27, 28]. These same benefits extend to quantum measurements and cluster state computing. This is particularly advantageous in integrated platforms where device size is a density constraint as an $O(N^2)$ scaling in 2-D cluster state size can be achieved with just $O(N)$ modulators.

We achieve ultrafast operation by engineering our waveguide to minimize the group velocity dispersion (GVD) near the signal and pump wavelengths as well as their mutual walk-off or group-velocity mismatch (GVM). By changing the height and width of our ridge waveguides, we can tune the dispersion to a low-GVM-GVD regime. This allows ultrafast pulses to propagate and interact with our waveguides without becoming distorted and spreading out in time. Operation with femtosecond pulses also increases nonlinear interaction strength thanks to higher peak powers for a given energy, and maximum clock speeds increase as the inverse of the pulse length. We show in this thesis that dispersion-engineered ridge waveguides can achieve clock speeds beyond 1 THz, exceeding what is currently possible with electronics.

1.4 Optical Parametric Amplifiers

The cornerstone of the quantum technologies we present in this thesis is the $\chi^{(2)}$ optical parametric amplifier (OPA). OPAs use a pump at 2ω to perform phase-sensitive amplification on a signal at ω . In later chapters, we will investigate the physical underpinnings of why phase-sensitive amplification makes OPAs ideal devices for generating, manipulating, and measuring quantum states. We fabricate our OPAs on the TFLN platform using standard techniques compatible with the majority of other TFLN devices.

In **Chapter 2**, we review the mathematics necessary to understand the behavior of quantum states under the SPDC Hamiltonian. We start from the quantized description of the electromagnetic field and introduce the concept of field quadratures to help us connect OPA-based measurements with the underlying theory. We then introduce the mathematical notion of ultrafast quantum pulses and the Hamiltonian implemented by $\chi^{(2)}$ nonlinear optics. We conclude this chapter with a discussion of multimode behavior and show how spectrotemporal modes arise naturally from the entanglement generated by OPAs.

In **Chapter 3**, we elaborate our discussion of spectrotemporal modes. These modes are an important consideration as they have a profound impact on measurements we investigate throughout the thesis. We discuss the challenges imposed by multimode

behavior and perform a literature review of various experiments which utilize OPAs as well as optical parametric oscillators (OPOs) as sources of quantum light. We then review techniques for achieving single-mode output for OPAs and examine the current state of the field.

In **Chapter 4**, we investigate ultrafast OPAs as sources of entangled pairs. We show that with dispersion engineering, we can generate biphotons with a temporal width of just 165 fs, the shortest entangled wavepacket from an integrated source demonstrated to date. We discuss the quantum theory behind the operation of our device and how dispersion and our pump laser work to limit temporal duration. We delve into the impact of multimode behavior on our measurement and discuss mitigation strategies. We then review the experiments used to characterize source performance, analyze collected data, and undertake a thorough literature review in which we contextualize the features of our source and examine its place among the variety of other source designs.

In **Chapter 5**, we show that OPAs can act as room-temperature ultrafast single photon detectors. By thresholding output measurements, we achieve a 26.5% detection efficiency and a 2.2% dark count rate. While these values are not competitive with state-of-the-art detectors based on superconducting circuits or semiconductor devices, our OPAs set the record for effective dead time as we are solely constrained by the dispersion of our device and not by electronics. We review the theoretical conception of detector measurements and show that the quantum behavior of our OPA can be uncovered by using known coherent states as an input probe. We then review the experimental setup and the data processing used to reconstruct the positive operator-valued measure (POVM). We take time to explore the theoretical limitations of our technique and show how performance can be enhanced by employing more sophisticated photodetection techniques. We also begin our initial discussions of pump depletion in this chapter, a phenomena with a profound effect on our measurements which can potentially help us exceed the theoretical maximum detection efficiency derived from the undepleted pump case.

In **Chapter 6**, we extend our analysis of OPAs to measure continuous-variable information and ultimately deduce the underlying quantum information of a SV state. Pioneered in [29], we initially showed that the macroscopic signal at the output of our OPA can be used to infer squeezing levels at the microscopic input. We now extend this technique further by resolving each individual pulse, allowing us to measure photon number statistics and recover the Wigner function, a full

description of the input quantum state. Through dispersion engineering, we achieve a maximum measurement clock rate of 6.5 THz. We first conduct a literature review of OPAs as detectors and derive their measurement behavior from first principles. We discuss in detail the impact of both multimode behavior and pump depletion on our measurements and show how these problems can be mitigated. We then review the experimental setup, discuss how shot-noise is calibrated, and analyze our collected data to show that our recovered Wigner function has a fidelity of 0.9998 relative to the expected Wigner function given the measured squeezing levels.

Finally in **Chapter 7**, we discuss the fabrication challenges facing TFLN and how these engineering problems motivate future directions. We also discuss how OPAs can be used as ultrafast classical switches to demultiplex THz information down to clock speeds suitable for electronics. From the discussions and analysis presented in this thesis, we conclude that lithium niobate nanophotonics has opened a viable route to ultrafast quantum information processing in a room-temperature chip-scale platform.

References

- [1] Christian L Degen, Friedemann Reinhard, and Paola Cappellaro. “Quantum sensing”. In: *Reviews of modern physics* 89.3 (2017), p. 035002.
- [2] Nicolas Gisin and Rob Thew. “Quantum communication”. In: *Nature photonics* 1.3 (2007), pp. 165–171.
- [3] Horowitz Mark, Grumbling Emily, National Academies of Sciences Engineering, Medicine, et al. *Quantum computing: progress and prospects*. The National Academies Press, 2019.
- [4] JR Kirtley, MB Ketchen, KG Stawiasz, JZ Sun, WJ Gallagher, SH Blanton, and SJ Wind. “High-resolution scanning SQUID microscope”. In: *Applied Physics Letters* 66.9 (1995), pp. 1138–1140.
- [5] Gerd Binnig and Heinrich Rohrer. “Scanning tunneling microscopy—from birth to adolescence”. In: *reviews of modern physics* 59.3 (1987), p. 615.
- [6] Göran Wendin. “Quantum information processing with superconducting circuits: a review”. In: *Reports on Progress in Physics* 80.10 (2017), p. 106001.
- [7] Hannah J Manetsch, Gyohei Nomura, Elie Bataille, Kon H Leung, Xudong Lv, and Manuel Endres. “A tweezer array with 6100 highly coherent atomic qubits”. In: *arXiv preprint arXiv:2403.12021* (2024).
- [8] L McCuller, C Whittle, D Ganapathy, K Komori, M Tse, A Fernandez-Galiana, L Barsotti, Peter Fritschel, M MacInnis, F Matichard, et al. “Frequency-

- dependent squeezing for advanced LIGO”. In: *Physical review letters* 124.17 (2020), p. 171102.
- [9] Warit Asavanant, Yu Shiozawa, Shota Yokoyama, Baramée Charoensombutamon, Hiroki Emura, Rafael N Alexander, Shuntaro Takeda, Jun-ichi Yoshikawa, Nicolas C Menicucci, Hidehiro Yonezawa, et al. “Generation of time-domain-multiplexed two-dimensional cluster state”. In: *Science* 366.6463 (2019), pp. 373–376.
- [10] Mikkel V Larsen, Xueshi Guo, Casper R Breum, Jonas S Neergaard-Nielsen, and Ulrik L Andersen. “Deterministic generation of a two-dimensional cluster state”. In: *Science* 366.6463 (2019), pp. 369–372.
- [11] Ayman F Abouraddy, Magued B Nasr, Bahaa EA Saleh, Alexander V Sergienko, and Malvin C Teich. “Quantum-optical coherence tomography with dispersion cancellation”. In: *Physical Review A* 65.5 (2002), p. 053817.
- [12] Bryce P. Hickam, Manni He, Nathan Harper, Szilard Szoke, and Scott K. Cushing. “Single-Photon Scattering Can Account for the Discrepancies among Entangled Two-Photon Measurement Techniques”. In: *The Journal of Physical Chemistry Letters* 13.22 (2022). PMID: 35635002, pp. 4934–4940. DOI: 10.1021/acs.jpcllett.2c00865. eprint: <https://doi.org/10.1021/acs.jpcllett.2c00865>. URL: <https://doi.org/10.1021/acs.jpcllett.2c00865>.
- [13] Rebecca Whittaker, Chris Erven, Alex Neville, Monica Berry, JL O’Brien, Hugo Cable, and JCF Matthews. “Absorption spectroscopy at the ultimate quantum limit from single-photon states”. In: *New Journal of Physics* 19.2 (2017), p. 023013.
- [14] Han-Sen Zhong, Hui Wang, Yu-Hao Deng, Ming-Cheng Chen, Li-Chao Peng, Yi-Han Luo, Jian Qin, Dian Wu, Xing Ding, Yi Hu, et al. “Quantum computational advantage using photons”. In: *Science* 370.6523 (2020), pp. 1460–1463.
- [15] EJ Lim, MM Fejer, and RL Byer. “Second-harmonic generation of green light in periodically poled planar lithium niobate waveguide”. In: *Electronics Letters* 25.3 (1989), pp. 174–174.
- [16] Taewon Park, Hubert S Stokowski, Vahid Ansari, Timothy P McKenna, Alexander Y Hwang, MM Fejer, and Amir H Safavi-Naeini. “High-efficiency second harmonic generation of blue light on thin-film lithium niobate”. In: *Optics Letters* 47.11 (2022), pp. 2706–2709.
- [17] Luis Ledezma, Ryoto Sekine, Qiushi Guo, Rajveer Nehra, Saman Jahani, and Alireza Marandi. “Intense optical parametric amplification in dispersion-engineered nanophotonic lithium niobate waveguides”. In: *Optica* 9.3 (2022), pp. 303–308.

- [18] Di Zhu, Linbo Shao, Mengjie Yu, Rebecca Cheng, Boris Desiatov, CJ Xin, Yaowen Hu, Jeffrey Holzgrafe, Soumya Ghosh, Amirhassan Shams-Ansari, et al. “Integrated photonics on thin-film lithium niobate”. In: *Advances in Optics and Photonics* 13.2 (2021), pp. 242–352.
- [19] Andrew J Mercante, Shouyuan Shi, Peng Yao, Linli Xie, Robert M Weikle, and Dennis W Prather. “Thin film lithium niobate electro-optic modulator with terahertz operating bandwidth”. In: *Optics express* 26.11 (2018), pp. 14810–14816.
- [20] Ran-Ran Xie, Gui-Qin Li, Feng Chen, and Gui-Lu Long. “Microresonators in lithium niobate thin films”. In: *Advanced Optical Materials* 9.19 (2021), p. 2100539.
- [21] Zheng Gong, Xianwen Liu, Yuntao Xu, and Hong X Tang. “Near-octave lithium niobate soliton microcomb”. In: *Optica* 7.10 (2020), pp. 1275–1278.
- [22] Qiushi Guo, Benjamin K Gutierrez, Ryoto Sekine, Robert M Gray, **James Williams**, Luis Ledezma, Luis Costa, Arkadev Roy, Selina Zhou, Mingchen Liu, et al. “Ultrafast mode-locked laser in nanophotonic lithium niobate”. In: *Science* 382.6671 (2023), pp. 708–713.
- [23] Mengjie Yu, David Barton III, Rebecca Cheng, Christian Reimer, Prashanta Kharel, Lingyan He, Linbo Shao, Di Zhu, Yaowen Hu, Hannah R Grant, et al. “Integrated femtosecond pulse generator on thin-film lithium niobate”. In: *Nature* 612.7939 (2022), pp. 252–258.
- [24] Xian Zhang, Xiaoyue Liu, Lin Liu, Ya Han, Heyun Tan, Liu Liu, Zhongjin Lin, Siyuan Yu, Ruijun Wang, and Xinlun Cai. “Heterogeneous integration of III–V semiconductor lasers on thin-film lithium niobate platform by wafer bonding”. In: *Applied Physics Letters* 122.8 (2023).
- [25] Shahriar Aghaeimeibodi, Boris Desiatov, Je-Hyung Kim, Chang-Min Lee, Mustafa Atabey Buyukkaya, Aziz Karasahin, Christopher JK Richardson, Richard P Leavitt, Marko Lončar, and Edo Waks. “Integration of quantum dots with lithium niobate photonics”. In: *Applied Physics Letters* 113.22 (2018).
- [26] Christian Leefmans, Avik Dutt, **James Williams**, Luqi Yuan, Midya Parto, Franco Nori, Shanhui Fan, and Alireza Marandi. “Topological dissipation in a time-multiplexed photonic resonator network”. In: *Nature Physics* 18.4 (2022), pp. 442–449.
- [27] Christian R Leefmans, Midya Parto, **James Williams**, Gordon HY Li, Avik Dutt, Franco Nori, and Alireza Marandi. “Topological temporally mode-locked laser”. In: *Nature Physics* (2024), pp. 1–7.
- [28] Gordon HY Li, Christian R Leefmans, **James Williams**, and Alireza Marandi. “Photonic elementary cellular automata for simulation of complex phenomena”. In: *Light: Science & Applications* 12.1 (2023), p. 132.

- [29] Rajveer Nehra, Ryoto Sekine, Luis Ledezma, Qiushi Guo, Robert M. Gray, Arkadev Roy, and Alireza Marandi. “Few-cycle vacuum squeezing in nanophotonics”. In: *Science* 377.6612 (Sept. 16, 2022), pp. 1333–1337. ISSN: 0036-8075, 1095-9203. DOI: [10.1126/science.abo6213](https://doi.org/10.1126/science.abo6213). URL: <https://www.science.org/doi/10.1126/science.abo6213> (visited on 06/27/2023).

Chapter 2

A VERY BRIEF INTRODUCTION TO QUANTUM OPTICS

2.1 A Quantum Description of the Electromagnetic Field

In this chapter, we review the physical and mathematical concepts necessary to understand and contextualize the nonlinear and quantum optics discussed later on. First, we review the second quantization of the electromagnetic field. Then we extend this quantization to arbitrary pulses and introduce the $\chi^{(2)}$ nonlinearity. Finally, we introduce the Hamiltonian of the system and discuss multimode descriptions of quantum states.

The hallmark of a quantized field is that we can only exchange energy with it in units of its quanta. For the electromagnetic field, this quanta is the photon. To describe a state with n photons, we can write down a state ψ as:

$$|\psi\rangle = |n\rangle \tag{2.1}$$

where ψ is a "wavefunction" describing the state of the field and $|n\rangle$ is a so-called "Fock state" describing a field with exactly n photons. To manipulate this field, we can introduce the operators a and a^\dagger , also known as the annihilation and creation operators respectively. Allowing these operators to act on a Fock state produces the following results:

$$a |n\rangle = \sqrt{n} |n-1\rangle \tag{2.2}$$

$$a^\dagger |n\rangle = \sqrt{n+1} |n+1\rangle \tag{2.3}$$

While a and a^\dagger deserve hats as they are operators, I have omitted the hats in this section to keep the math readable. The operators themselves are related through the commutator:

$$[a, a^\dagger] = aa^\dagger - a^\dagger a = 1 \tag{2.4}$$

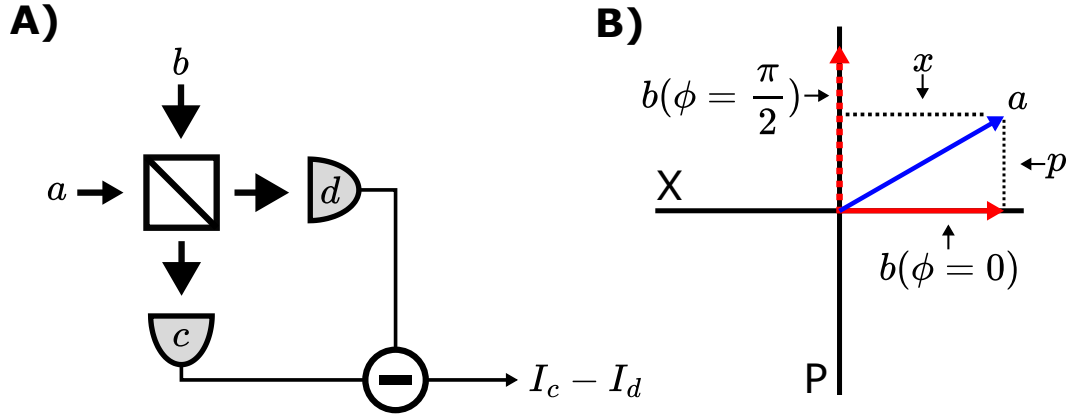


Figure 2.1: A) A schematic of homodyne detection with a as the measured field and b as the local oscillator. B) A phasor diagram plotting a with respect to the quadratures of b .

To connect this abstraction to what we can physically measure in the lab, we need to introduce the concept of observables. An observable A is a Hermitian operator which extracts a physically measurable quantity from the state. While a and a^\dagger are not observables as $(a)^\dagger = a^\dagger \neq a$, we can use them to construct:

$$\hat{N} = a^\dagger a \quad (2.5)$$

and

$$\hat{N}^\dagger = (a^\dagger a)^\dagger = (a)^\dagger (a^\dagger)^\dagger = a^\dagger a = \hat{N} \quad (2.6)$$

\hat{N} is the photon number operator. Allowing it to act on a Fock state $|n\rangle$ gives us:

$$\hat{N} |n\rangle = a^\dagger a |n\rangle = a^\dagger \sqrt{n} |n-1\rangle = n |n\rangle \quad (2.7)$$

We will use \hat{N} in later sections to analyze photon number measurements and discern information about an unknown $|\psi\rangle$.

2.2 Quadratures and Continuous Variable Quantum Optics

Homodyne detection is an optical signal measurement method often used in telecommunications. Figure 2.1A shows the experimental schematic. An unknown field $A(t)$ is interfered with a known local oscillator $B(t)$ at a balanced beamsplitter. The output ports C and D of the beamsplitter are measured via photodetection, and

the current from each photodetector is subtracted. We can write down the field operators at C and D as:

$$c = \frac{1}{\sqrt{2}}(a + ib) \quad d = \frac{1}{\sqrt{2}}(b + ia) \quad (2.8)$$

The photodetectors convert optical power to current (i.e $I_{det} = |E(t)|^2$), and so:

$$\begin{aligned} I_C &\propto c^\dagger c = \frac{1}{2}(a^2 + iab - iab^\dagger + b^2) \\ I_D &\propto d^\dagger d = \frac{1}{2}(b^2 + iab - ia^\dagger b + a^2) \end{aligned} \quad (2.9)$$

Subtracting their currents gives us:

$$I_C - I_D \propto i(a^\dagger b - b^\dagger a) \quad (2.10)$$

If we assume that b is a classical field such that $b(\phi) \propto |B|e^{i\phi}$, then Eq.2.10 becomes:

$$I_C - I_D \propto i|B|(a^\dagger e^{i\phi} - a e^{-i\phi}) \quad (2.11)$$

Now we introduce two new operators defined using the symmetric and anti-symmetric combination of the creation and annihilation operators:

$$x = \frac{1}{\sqrt{2}}(a + a^\dagger) \quad p = \frac{1}{i\sqrt{2}}(a - a^\dagger) \quad (2.12)$$

We can show that x and p can be used to represent the results of the homodyne measurement:

$$p \cos(\phi) - x \sin(\phi) = \frac{i}{\sqrt{2}}(a^\dagger e^{i\phi} - a e^{-i\phi}) \quad (2.13)$$

where we have constructed the right-hand side of Eq.2.12 up to a scalar. x and p , the quadratures of the field acted on by a and a^\dagger , represent the "in-phase" and "out-of-phase" components of the field. Figure 2.1B shows the phasor-diagram depicting the relationship between the local oscillator b (used as a reference for the field) and a , the field to be measured. x and p can be thought of as the projections

of a onto $b(\phi = 0)$ and its phase-shifted clone $b(\phi = \frac{\pi}{2})$. x and p will become useful concepts later on when we show how parametric process can amplify and de-amplify these quadratures. We note that

$$x^2 + p^2 = aa^\dagger + a^\dagger a = 2a^\dagger a + 1 = 2\hat{N} + 1 \quad (2.14)$$

The $+1$ at the end of Eq.2.14 is a result of the presence of vacuum energy in the field.

2.3 Defining Quantum Ultrafast Pulses

Until now, we've limited our description of these fields and their evolution to expressions involving a and a^\dagger , but these operators tell us nothing about the time-dependent distribution of the electric field. To describe a pulse, we can treat the pulse shape itself as a mode and use ladder operators to denote its occupancy such that:

$$A_m = \int E_m(t)a(t)dt \quad (2.15)$$

where A_m is the broadband photon annihilation operator acting on photons in the electric field distribution $E_m(t)$. To describe the total field $a(t)$ across all modes, we can construct it as a superposition of m modes:

$$a(t) = \sum_m E_m(t)A_m \quad (2.16)$$

While these m modes are ultimately up to us to define, we will see in future sections that the property:

$$\int E_m(t)E_n(t)dt = \delta_{m,n} \quad (2.17)$$

ensures these m modes remain uncorrelated and therefore unentangled with each other. This will help us partition multimode systems into distinct parts which we can analyze independently.

2.4 The $\chi^{(2)}$ Nonlinearity and Hamiltonian

The $\chi^{(2)}$ nonlinear interaction describes a 3-photon process in which either one photon (the pump photon) is annihilated and two are created (the signal and idler

photons) or vice versa. The former case is termed "optical parametric amplification" (OPA) or, when the amplification is performed on the vacuum field, "optical parametric generation" (OPG), while the latter case is termed "sum frequency generation" (SFG). To model these process mathematically, we define b and b^\dagger to represent the pump field at 2ω and a and a^\dagger to be the signal/idler field where we have assumed degeneracy such that the signal and idler are indistinguishable and hence belong to the same field. To represent OPA, we use the constructed operator $a^{\dagger 2}b$ to create a pair of signal/idler photons and annihilate a pump photon while SFG can be represented with a^2b^\dagger to annihilate a signal/idler pair and create a pump photon. Putting it all together, we express the Hamiltonian as:

$$\hat{H} = \omega_a a^\dagger a + \omega_b b^\dagger b + g(a^{\dagger 2}b + a^2b^\dagger) \quad (2.18)$$

where terms such as $\omega_a a^\dagger a$ denote energy resulting from the photon occupancy of the field and g represents a nonlinear coupling parameter calculated from the spatial and temporal overlap of the signal/idler and pump fields. We will return to this Hamiltonian later on and use it to derive quantum states at the output of an OPA.

2.5 Multimode Quantum Optics

Generally, modes are anything that can be written as a $|\rangle$. The occupancy states of a field are modes (i.e $|0\rangle, |1\rangle$ etc), and, in later chapters, we will discuss how continuous-variable states can be described with superpositions of these modes. In the context of OPAs, we can use their spectrotemporal modes to analyze their behavior as sources and measurement devices. The OPA produces a signal and idler field at its output which are correlated as a result of energy and momentum conservation. To study their correlation, we can plot the joint-probability amplitude of detecting a single signal photon at a frequency of f_{signal} while simultaneously detecting an idler photon at f_{idler} . We refer to this joint-probability function as the joint-spectral intensity or the JSI.

Figure 2.2 shows the JSI of our biphoton source presented in **Chapter 4**. At low gains, the JSI can be approximated as the product of the energy conservation of the pump (Fig. 2.2A) and the phase-matching condition (Fig. 2.2B). The phase-matching condition is calculated from the dispersive properties of the waveguide as well as the poling period. At higher gains, the JSI must be calculated from the Heisenberg propagators as defined in [2]. As our JSI is inseparable ($JSI(\omega_s, \omega_i) \neq \phi(\omega_s)\phi(\omega_i)$), we can decompose it into multiple independent modes

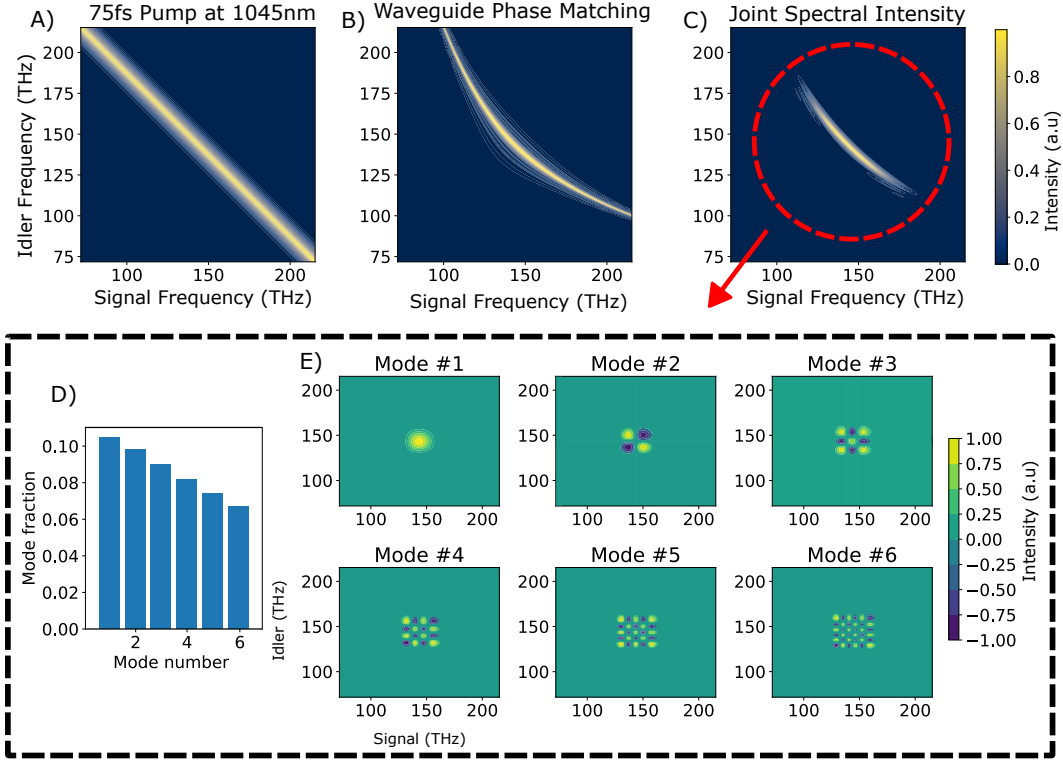


Figure 2.2: A) The energy conservation of the pump laser plotted as a function of the signal and idler frequencies. This is for a 75-fs transform-limited mode locked laser centered at 1045nm. B) The phase matching condition of a thin-film periodically poled lithium niobate waveguide in the type-0 configuration. The waveguide design can be found in [1]. Yellow areas are where parametric down-conversion from a pump photon to a signal and idler photon are supported. C) The joint spectral intensity function computed as the product of the pump and phase matching. D) A plot of the mode occupancy vs mode number of the JSI in panel C. E) Plots of the first 6 modes composing the JSI.

$\Phi(\omega_s, \omega_i)$ which can be expressed as $\Phi(\omega_s, \omega_i) = \phi(\omega_s)\phi(\omega_i)$. This multimode behavior fundamentally stems from the inability to satisfy the group-velocity criteria established in [3].

A multimode OPA can be modeled as a collection of single-mode OPAs acting on each mode. The output of an OPA after amplifying vacuum can be described as:

$$\rho = \bigotimes_{n=1}^N S_n^\dagger \rho_{vac} S_n \quad (2.19)$$

where S_n^\dagger is the squeezing operator of the Nth mode of the OPA. ρ is a multimode output state, making it challenging to isolate and measure the effects of squeezing

on a single mode. We experimentally analyze the impact of multiple modes during measurement and discuss how to mitigate multimode effects later on in **Chapter 6**.

References

- [1] James Williams, Rajveer Nehra, Elina Sendonaris, Luis Ledezma, Robert M Gray, Ryoto Sekine, and Alireza Marandi. “Ultra-Short Pulse Biphoton Source in Lithium Niobate Nanophotonics at 2\textmu m”. In: *arXiv preprint arXiv:2402.05163* (2024).
- [2] Martin Houde and Nicolás Quesada. “Waveguided sources of consistent, single-temporal-mode squeezed light: The good, the bad, and the ugly”. In: *AVS Quantum Science* 5.1 (2023).
- [3] Alfred B U’Ren, Christine Silberhorn, Reinhard Erdmann, Konrad Banaszek, Warren P Grice, Ian A Walmsley, and Michael G Raymer. “Generation of pure-state single-photon wavepackets by conditional preparation based on spontaneous parametric downconversion”. In: *arXiv preprint quant-ph/0611019* (2006).

SPECTROTEMPORAL MODES

3.1 Mode Structure

As discussed in chapter **Chapter 2**, the time-dependent electric field of a quantum state can be described using a basis of temporal modes [1], and these modes are computed via the Bloch-Messiah decomposition, representing entanglement in energy and time [2]. The distribution of these modes within a quantum state becomes relevant when multiple independent sources of quantum light are interfered as part of a computation. Observing strong interference is only possible when measurements performed on the system are sensitive only to a single mode. In a solid-state system such as the quantum dot, this problem is typically addressed through filtering output single photons to enforce a single spectral mode as interactions with the crystal lattice and defects can cause source broadening. For sources of quantum light based on nonlinear optics, such as spontaneous parametric down-conversion, single-mode emission is not guaranteed. If multiple temporal modes experience non-negligible phase matching for a given nonlinear process, then the output state will be created in a superposition of temporal modes. For temporally-multiplexed systems, this poses a problem as multimode states made from different laser pulses will have degraded interference by a factor of approximately $\frac{1}{N}$, where N is the number of modes [3]. This can be understood intuitively as the interference of two states being an effective measurement of their relative temporal modes. If both states share the same temporal mode they interfere strongly, whereas states in different modes will not experience interference as they are mutually orthogonal.

3.2 Continuous Variable Cluster States from Parametric Oscillators

For experiments using multiple independent squeezed states of light, multimode interference can be avoided by using mode-selective detection. Homodyne detection is often employed for this task as the measured mode is determined by shaping the local oscillator[4]. This technique is used in [5, 6, 7, 8, 9] to measure independent squeezed vacuum states for continuous variable quantum information processing using cluster states. Larsen et al [5, 6] utilize two separate bowtie-cavity type-0 OPOs made with periodically poled potassium titanyl phosphate (PPKTP) as their gain medium. Each oscillator, when pumped below threshold, produces pulses of

multimode squeezed vacuum, which are then combined at a beam splitter with a $\frac{\pi}{2}$ phase shift on one input to create 2-mode entangled states. These states are then sent through a series of delays and additional beam splitters to create an N-mode cluster state. This highly multimode state is measured at two separate homodyne detectors which confirm the non-classical entanglement for a single mode through a series of nullifier measurements. Cluster states made from squeezed light can also be used for general purpose quantum computing via MBQC. Asavant et al [7] perform a similar experiment to [5, 6], but instead use four separate type-0 OPOs to generate a large-scale cluster state. Konno et al [8, 9] uses two separate type-0 OPOs made with a PPKTP gain medium placed in a Fabry–Pérot cavity. The single mode squeezed vacuum states emitted from these oscillators are first passed through a beam splitter with 5% reflection. The reflected port of the beam splitter is directed to a superconducting nanowire single photon detector (SNSPD) so that idler photons from the squeezed vacuum state can be detected. When an idler photon is detected, this indicates that a single photon has been subtracted from the squeezed state, causing it to become a so-called kitten state, or an approximation of a Schrodinger’s cat state. Cat states are of great interest in quantum information processing as they can be used to implement quantum error correction with only logarithmic overhead [10]. Many optical photon-subtracted kittens and cats have been demonstrated [11, 12, 13, 14]. The novelty of [8, 9] is to create two independent cat states and then combine them at a 50:50 beam splitter to generate a Gottesman-Kitaev-Preskill (GKP) state. GKP states are also of interest as they provide additional phase-space symmetries which can be used to construct error correction methods capable of correcting single and multi-qubit errors [15, 16, 17, 18]. OPOs can also take advantage of the resonant enhancement of the pump field to lower the levels of nonlinear gain required as well as limit the degradation of the observable squeezing induced by amplitude and phase noise from the pump [19]. However, using OPOs as sources is not always desirable. For pulsed operation, the pulse repetition rate must match the cavity round-trip time. This ultimately constrains the physical dimensions of the OPO to the round-trip distance of the implementation medium (be it free-space, integrated photonics, etc). The cavity itself also requires stabilization through a complex external locking mechanism, and the observable squeezing is ultimately limited by the escape efficiency of the cavity [20].

3.3 Parametric Amplifiers as Sources of Quantum Light

From a practicality standpoint, using an OPA to generate squeezed vacuum is advantageous as OPAs do not require locking, and can, in principle, support operation with any pulse repetition rate, so long as the pulses do not begin to overlap because of the dispersion in the nonlinear medium. When combined with dispersion engineering, chip-scale OPAs can be made to support the propagation of ultrafast pulses, leading to record-breaking gain and gain bandwidth [21]. To understand the structure of the entanglement produced by these OPAs, we can compute their joint-spectral intensity function or JSI. The JSI is the joint probability distribution of the photon pairs emitted during parametric down conversion. A full computation of the JSI involves calculating the evolution of the creation and annihilation operators for the signal and idler modes. In the low gain limit, the JSI can be approximated as the product of the energy conservation of the pump and the phase matching as a function of the signal and idler frequencies [2]. Fig. 2.2A-C shows these functions for an OPA fabricated on thin-film lithium niobate [22]. The shape of the JSI contains information about the time-energy entanglement of the signal and idler. When the JSI cannot be written as the product of two independent functions of the signal and idler (i.e. $JSI(\omega_i, \omega_s) \neq |S_s(\omega_s)||S_i(\omega_i)|$ where $S_{s,i}(\omega_{s,i})$ are the spectral distributions for the signal/idler photons), the signal and idler are correlated. If the pair are in a true superposition, as opposed to a mixed state, then the JSI will exhibit non-classical correlations which experimentally violate Bell's inequality[23, 24]. Maclean et al [23] use a BiBO crystal in a type-I configuration to generate time-energy entangled photon pairs, and measure their correlations via dispersive frequency measurements and femtosecond-timescale temporal measurements implemented using photon up-conversion. Combining information from the frequency-frequency, time-time, time-frequency, and frequency-time correlations provides the data needed for a total recovery of the amplitude and phase information, allowing them to compute the joint-spectral amplitude (JSA) which contains phase information not present in the JSI. Chen et al [24] develop a simplified method for measuring the JSA through a method they coin as "conjugate-franson interferometry". This method modifies a standard Franson interferometer by adding acousto-optic modulators in one arm of the signal/idler Mach-Zender paths and performing dispersive frequency readout at the single photon detectors to infer phase and amplitude information. Fig. 2.2E shows the decomposition of the JSI in Fig. 2.2C. The modes that comprise the basis can all be expressed as $JSI(\omega_i, \omega_s) = |S_s(\omega_s)||S_i(\omega_i)|$. Franson interferometry combined with pair generation has recently been demonstrated in an integrated

platform [25]. One method to suppress these higher-order modes is bandpass filtering. Filtering limits measurements to a small region of the JSI. If this region is approximately constant in amplitude and phase, the measured photon pairs will appear to be a single mode. Filtering comes at the cost of reduced pair generation rate as well as the introduction of distinguishable thermal parts of the overall state. This is a result of vacuum fluctuations entering from frequency-dependent losses at the filter [2].

While the multimodeness may create challenges in some scenarios, others have suggested and demonstrated the use of these modes as a basis for storing and manipulating quantum information. Eckstein et al [26] propose the concept of a quantum pulse gate (QPG). A QPG operates by selectively addressing and performing frequency up-conversion on one of the modes of an incoming photon. This mode selectivity is engineered by both shaping the pump and the phase matching function of an OPA such that only one mode experiences a strong parametric interaction. Brecht et al [1] describe how these temporal modes can be exploited to perform standard QIP tasks such as state manipulation, measurement, and practical applications such as quantum key distribution. Ansari et al [27] experimentally demonstrate a technique to perform detector tomography and determine the measurement operators implemented by a QPG. By carefully preparing a pump and signal pulse with specific spectral and temporal structures, the measurement operators of the QPG can be inferred via the measurement outcomes that result from the injected signal and pump pulses. Serino et al [28] take the QPG technique a step further by experimentally demonstrating the demultiplexing of five independent temporal modes of an incoming single photon.

For type-0 phase matching, the signal and idler frequencies share the same spatial mode and therefore the same dispersive properties. This makes it difficult to achieve single-mode operation as the group velocity criteria in [29] cannot be satisfied. Intuitively, this can be thought of as a result of symmetries present in the JSI. Because the JSI must be symmetric about the line $\omega_s = \omega_i$, any phase matching near degeneracy must have a negative slope and therefore run parallel to the energy conservation condition of the pump. Theoretical device proposals for near single-mode operation in type-0 have recently been presented. Houde et al along with Mundhra et al both propose an ultrashort pulse pumped waveguide design with a high GVM at the signal/idler wavelength to suppress higher-order modes [30, 31]. Type-2 sources, in which the signal and idler are emitted into different polarization

modes, can satisfy the necessary group velocity criteria. When combined with engineered poling domains designed to remove fringes from the phase matching function, these sources can produce single-mode light [32, 33, 34, 35], and are used in experiments where multiple biphoton sources are interfered [36, 37, 38, 39, 40]. However, this light may initially be generated in a mixed state, and additional optics are often needed to create a coherent superposition depending on the desired measurement basis [41]. Mosley et al [34] achieve single-mode operation through a combination of dispersion engineering and an ultra-fast pump to satisfy [29]. By using a wavelength at which pump photons experience the same group velocity as either the signal or idler photons, a circular JSI free of spectral correlations can be generated when the phase matching is excited by a broadband pump. Dixon et al [33] achieve single mode operation through the engineering of the periodic reversal of the crystal domain directions in their nonlinear gain medium. This periodic reversal, known as periodic poling, is used to meet momentum conservation requirements for efficient photon pair generation by changing the sign of the $\chi^{(2)}$ nonlinearity along the length of the waveguide. Varying the duty-cycle of each poling domain while keeping the poling period constant allows for the suppression of side lobes in the JSI, enhancing the state purity to as high as 97%. In general, modification of the poling function to achieve a desired JSI shape is known as "domain engineering". Graffitti et al [35] use a more complex approach to domain engineering by employing an annealing algorithm to form a Gaussian JSI, achieving a purity of 95.5%. Zhong et al [40] use a combination of domain engineering and filtering to operate in a single mode. After passing emitted photons through a 12-nm bandpass filter, [40] measures a spectral purity of 99%, allowing them to use 25 independent sources of photon pairs in parallel to conduct large scale boson-sampling experiments and demonstrate a quantum advantage in optics for the first time. Xin et al [32] extend the techniques of domain and dispersion engineering to thin-film lithium niobate, achieving an unfiltered purity greater than 94%. [32] first tunes the waveguide geometry such that the group velocity of the pump lies between that of the signal and idler. After a geometry is chosen, the poling domains are apodized and selectively deleted to generate a Gaussian phase matching function.

References

- [1] B. Brecht, Dileep V. Reddy, C. Silberhorn, and M. G. Raymer. "Photon Temporal Modes: A Complete Framework for Quantum Information Science". In: *Phys. Rev. X* 5.4 (Oct. 30, 2015), p. 041017. ISSN: 2160-3308. DOI:

- 10.1103/PhysRevX.5.041017. URL: <https://link.aps.org/doi/10.1103/PhysRevX.5.041017> (visited on 07/06/2023).
- [2] Martin Houde and Nicolás Quesada. “Waveguided sources of consistent, single-temporal-mode squeezed light: The good, the bad, and the ugly”. In: *AVS Quantum Science* 5.1 (Mar. 1, 2023), p. 011404. ISSN: 2639-0213. DOI: 10.1116/5.0133009. URL: <https://pubs.aip.org/aqs/article/5/1/011404/2879061/Waveguided-sources-of-consistent-single-temporal> (visited on 01/24/2024).
- [3] Christopher L Morrison, Francesco Graffitti, Peter Barrow, Alexander Pickston, Joseph Ho, and Alessandro Fedrizzi. “Frequency-bin entanglement from domain-engineered down-conversion”. In: *APL Photonics* 7.6 (2022).
- [4] Jonathan Roslund, Renné Medeiros De Araujo, Shifeng Jiang, Claude Fabre, and Nicolas Treps. “Wavelength-multiplexed quantum networks with ultrafast frequency combs”. In: *Nature Photonics* 8.2 (2014), pp. 109–112.
- [5] Mikkel V. Larsen, Xueshi Guo, Casper R. Breum, Jonas S. Neergaard-Nielsen, and Ulrik L. Andersen. “Deterministic generation of a two-dimensional cluster state”. In: *Science* 366.6463 (Oct. 18, 2019), pp. 369–372. ISSN: 0036-8075, 1095-9203. DOI: 10.1126/science.aay4354. URL: <https://www.science.org/doi/10.1126/science.aay4354> (visited on 01/24/2024).
- [6] Mikkel V. Larsen, Xueshi Guo, Casper R. Breum, Jonas S. Neergaard-Nielsen, and Ulrik L. Andersen. “Deterministic multi-mode gates on a scalable photonic quantum computing platform”. In: *Nat. Phys.* 17.9 (Sept. 2021). Number: 9 Publisher: Nature Publishing Group, pp. 1018–1023. ISSN: 1745-2481. DOI: 10.1038/s41567-021-01296-y. URL: <https://www.nature.com/articles/s41567-021-01296-y> (visited on 07/06/2023).
- [7] Warit Asavanant, Yu Shiozawa, Shota Yokoyama, Baramée Charoensombutamon, Hiroki Emura, Rafael N. Alexander, Shuntaro Takeda, Jun-ichi Yoshikawa, Nicolas C. Menicucci, Hidehiro Yonezawa, and Akira Furusawa. “Generation of time-domain-multiplexed two-dimensional cluster state”. In: *Science* 366.6463 (Oct. 18, 2019). Publisher: American Association for the Advancement of Science, pp. 373–376. DOI: 10.1126/science.aay2645. URL: <https://www.science.org/doi/10.1126/science.aay2645> (visited on 07/06/2023).
- [8] Shunya Konno, Warit Asavanant, Fumiya Hanamura, Hironari Nagayoshi, Kosuke Fukui, Atsushi Sakaguchi, Ryuhoh Ide, Fumihiro China, Masahiro Yabuno, Shigehito Miki, et al. “Logical states for fault-tolerant quantum computation with propagating light”. In: *Science* 383.6680 (2024), pp. 289–293.
- [9] Shunya Konno, Warit Asavanant, Fumiya Hanamura, Hironari Nagayoshi, Kosuke Fukui, Atsushi Sakaguchi, Ryuhoh Ide, Fumihiro China, Masahiro

- Yabuno, Shigehito Miki, et al. “Propagating Gottesman-Kitaev-Preskill states encoded in an optical oscillator”. In: *arXiv preprint arXiv:2309.02306* (2023).
- [10] David S Schlegel, Fabrizio Minganti, and Vincenzo Savona. “Quantum error correction using squeezed Schrödinger cat states”. In: *Physical Review A* 106.2 (2022), p. 022431.
- [11] Kentaro Wakui, Hiroki Takahashi, Akira Furusawa, and Masahide Sasaki. “Photon subtracted squeezed states generated with periodically poled KTiOPO₄”. In: *Optics Express* 15.6 (2007), p. 3568. ISSN: 1094-4087. DOI: 10.1364/OE.15.003568. URL: <https://opg.optica.org/oe/abstract.cfm?uri=oe-15-6-3568> (visited on 02/28/2024).
- [12] Valentina Parigi, Alessandro Zavatta, Myungshik Kim, and Marco Bellini. “Probing Quantum Commutation Rules by Addition and Subtraction of Single Photons to/from a Light Field”. In: *Science* 317.5846 (Sept. 28, 2007), pp. 1890–1893. ISSN: 0036-8075, 1095-9203. DOI: 10.1126/science.1146204. URL: <https://www.science.org/doi/10.1126/science.1146204> (visited on 02/28/2024).
- [13] Alexei Ourjoumtsev, Rosa Tualle-Brouri, Julien Laurat, and Philippe Grangier. “Generating Optical Schrödinger Kittens for Quantum Information Processing”. In: *Science* 312.5770 (Apr. 7, 2006), pp. 83–86. ISSN: 0036-8075, 1095-9203. DOI: 10.1126/science.1122858. URL: <https://www.science.org/doi/10.1126/science.1122858> (visited on 02/28/2024).
- [14] Alexei Ourjoumtsev, Hyunseok Jeong, Rosa Tualle-Brouri, and Philippe Grangier. “Generation of optical ‘Schrödinger cats’ from photon number states”. In: *Nature* 448.7155 (Aug. 16, 2007), pp. 784–786. ISSN: 0028-0836, 1476-4687. DOI: 10.1038/nature06054. URL: <https://www.nature.com/articles/nature06054> (visited on 02/28/2024).
- [15] Kan Takase, Kosuke Fukui, Akito Kawasaki, Warit Asavanant, Mamoru Endo, Jun-ichi Yoshikawa, Peter Van Loock, and Akira Furusawa. “Gottesman-Kitaev-Preskill qubit synthesizer for propagating light”. In: *npj Quantum Information* 9.1 (Oct. 10, 2023), p. 98. ISSN: 2056-6387. DOI: 10.1038/s41534-023-00772-y. URL: <https://www.nature.com/articles/s41534-023-00772-y> (visited on 02/28/2024).
- [16] Kyungjoo Noh and Christopher Chamberland. “Fault-tolerant bosonic quantum error correction with the surface-Gottesman-Kitaev-Preskill code”. In: *Physical Review A* 101.1 (Jan. 13, 2020), p. 012316. ISSN: 2469-9926, 2469-9934. DOI: 10.1103/PhysRevA.101.012316. URL: <https://link.aps.org/doi/10.1103/PhysRevA.101.012316> (visited on 02/28/2024).
- [17] P. Campagne-Ibarcq, A. Eickbusch, S. Touzard, E. Zalys-Geller, N. E. Frattini, V. V. Sivak, P. Reinhold, S. Puri, S. Shankar, R. J. Schoelkopf, L. Frunzio, M. Mirrahimi, and M. H. Devoret. “Quantum error correction of a qubit encoded in grid states of an oscillator”. In: *Nature* 584.7821 (Aug. 20, 2020), pp. 368–

372. ISSN: 0028-0836, 1476-4687. DOI: 10.1038/s41586-020-2603-3. URL: <https://www.nature.com/articles/s41586-020-2603-3> (visited on 02/28/2024).
- [18] Kosuke Fukui, Akihisa Tomita, Atsushi Okamoto, and Keisuke Fujii. “High-Threshold Fault-Tolerant Quantum Computation with Analog Quantum Error Correction”. In: *Physical Review X* 8.2 (May 25, 2018), p. 021054. ISSN: 2160-3308. DOI: 10.1103/PhysRevX.8.021054. URL: <https://link.aps.org/doi/10.1103/PhysRevX.8.021054> (visited on 02/28/2024).
- [19] J Teja and Ngai C Wong. “Twin-beam generation in a triply resonant dual-cavity optical parametric oscillator”. In: *Optics Express* 2.3 (1998), pp. 65–71.
- [20] S Chaturvedi, K Dechoum, and PD Drummond. “Limits to squeezing in the degenerate optical parametric oscillator”. In: *Physical Review A* 65.3 (2002), p. 033805.
- [21] Luis Ledezma, Ryoto Sekine, Qiushi Guo, Rajveer Nehra, Saman Jahani, and Alireza Marandi. “Intense optical parametric amplification in dispersion-engineered nanophotonic lithium niobate waveguides”. In: *Optica* 9.3 (2022), pp. 303–308.
- [22] James Williams, Rajveer Nehra, Elina Sendonaris, Luis Ledezma, Robert M Gray, Ryoto Sekine, and Alireza Marandi. “Ultra-Short Pulse Biphoton Source in Lithium Niobate Nanophotonics at 2\textmu m”. In: *arXiv preprint arXiv:2402.05163* (2024).
- [23] Jean-Philippe W MacLean, John M Donohue, and Kevin J Resch. “Ultrafast quantum interferometry with energy-time entangled photons”. In: *Physical Review A* 97.6 (2018), p. 063826.
- [24] Changchen Chen, Jeffrey H Shapiro, and Franco NC Wong. “Experimental demonstration of conjugate-Franson interferometry”. In: *Physical Review Letters* 127.9 (2021), p. 093603.
- [25] Giovanni Finco, Filippo Miserochi, Andreas Maeder, Jost Kellner, Alessandra Sabatti, Robert J Chapman, and Rachel Grange. “Time-bin entangled Bell state generation and tomography on thin-film lithium niobate”. In: *npj Quantum Information* 10.1 (2024), p. 135.
- [26] Andreas Eckstein, Benjamin Brecht, and Christine Silberhorn. “A quantum pulse gate based on spectrally engineered sum frequency generation”. In: *Optics express* 19.15 (2011), pp. 13770–13778.
- [27] Vahid Ansari, Georg Harder, Markus Allgaier, Benjamin Brecht, and Christine Silberhorn. “Temporal-mode measurement tomography of a quantum pulse gate”. In: *Physical Review A* 96.6 (2017), p. 063817.

- [28] Laura Serino, Jano Gil-Lopez, Michael Stefszky, Raimund Ricken, Christof Eigner, Benjamin Brecht, and Christine Silberhorn. “Realization of a multi-output quantum pulse gate for decoding high-dimensional temporal modes of single-photon states”. In: *PRX quantum* 4.2 (2023), p. 020306.
- [29] Warren P Grice, Alfred B U’Ren, and Ian A Walmsley. “Eliminating frequency and space-time correlations in multiphoton states”. In: *Physical Review A* 64.6 (2001), p. 063815.
- [30] Martin Houde, Liam Beaudoin, Kazuki Hirota, Rajveer Nehra, and Nicolás Quesada. “Ultrashort-pulse-pumped, single-mode type-0 squeezers in lithium niobate nanophotonics”. In: *arXiv preprint arXiv:2412.17708* (2024).
- [31] Shivam Mundhra, Elina Sendonaris, Robert M Gray, **James Williams**, and Alireza Marandi. “Optimizing for a Near Single-Mode Type-0 Optical Parametric Amplifier in Nanophotonics”. In: *arXiv preprint arXiv:2412.07004* (2024).
- [32] CJ Xin, Jatadhari Mishra, Changchen Chen, Di Zhu, Amirhassan Shams-Ansari, Carsten Langrock, Neil Sinclair, Franco NC Wong, MM Fejer, and Marko Lončar. “Spectrally separable photon-pair generation in dispersion engineered thin-film lithium niobate”. In: *Optics Letters* 47.11 (2022), pp. 2830–2833.
- [33] P Ben Dixon, Jeffrey H Shapiro, and Franco NC Wong. “Spectral engineering by Gaussian phase-matching for quantum photonics”. In: *Optics express* 21.5 (2013), pp. 5879–5890.
- [34] Peter J Mosley, Jeff S Lundeen, Brian J Smith, Piotr Wasylczyk, Alfred B U’Ren, Christine Silberhorn, and Ian A Walmsley. “Heralded generation of ultrafast single photons in pure quantum states”. In: *Physical Review Letters* 100.13 (2008), p. 133601.
- [35] Francesco Graffitti, Peter Barrow, Massimiliano Proietti, Dmytro Kundys, and Alessandro Fedrizzi. “Independent high-purity photons created in domain-engineered crystals”. In: *Optica* 5.5 (2018), pp. 514–517.
- [36] Pieter Kok, William J Munro, Kae Nemoto, Timothy C Ralph, Jonathan P Dowling, and Gerard J Milburn. “Linear optical quantum computing with photonic qubits”. In: *Reviews of modern physics* 79.1 (2007), p. 135.
- [37] Peter C Humphreys, Benjamin J Metcalf, Justin B Spring, Merritt Moore, Xian-Min Jin, Marco Barbieri, W Steven Kolthammer, and Ian A Walmsley. “Linear optical quantum computing in a single spatial mode”. In: *Physical review letters* 111.15 (2013), p. 150501.
- [38] H-J Briegel, Wolfgang Dür, Juan I Cirac, and Peter Zoller. “Quantum repeaters: the role of imperfect local operations in quantum communication”. In: *Physical Review Letters* 81.26 (1998), p. 5932.

- [39] Justin B Spring, Benjamin J Metcalf, Peter C Humphreys, W Steven Kolthammer, Xian-Min Jin, Marco Barbieri, Animesh Datta, Nicholas Thomas-Peter, Nathan K Langford, Dmytro Kundys, et al. “Boson sampling on a photonic chip”. In: *Science* 339.6121 (2013), pp. 798–801.
- [40] Han-Sen Zhong, Hui Wang, Yu-Hao Deng, Ming-Cheng Chen, Li-Chao Peng, Yi-Han Luo, Jian Qin, Dian Wu, Xing Ding, Yi Hu, et al. “Quantum computational advantage using photons”. In: *Science* 370.6523 (2020), pp. 1460–1463.
- [41] Heonoh Kim, Sang Min Lee, Osung Kwon, and Han Seb Moon. “Two-photon interference of polarization-entangled photons in a Franson interferometer”. In: *Scientific reports* 7.1 (2017), p. 5772.

*Chapter 4***ULTRASHORT PULSE BIPHOTON SOURCE IN LITHIUM
NIOBATE NANOPHOTONICS AT 2 MICRON**

James Williams, Rajveer Nehra, Elina Sendonaris, Luis Ledezma, Robert M. Gray, Ryoto Sekine, and Alireza Marandi. "Ultrashort pulse biphoton source in lithium niobate nanophotonics at 2 μm ." *Nanophotonics* 0 (2024).

ABSTRACT

Photonics offers unique capabilities for quantum information processing (QIP) such as room-temperature operation, the scalability of nanophotonics, and access to ultrabroad bandwidths and consequently ultrafast operation. Ultrashort-pulse sources of quantum states in nanophotonics are an important building block for achieving scalable ultrafast QIP, however, their demonstrations so far have been sparse. Here, we demonstrate a femtosecond biphoton source in dispersion-engineered periodically poled lithium niobate nanophotonics. We measure 17 THz of bandwidth for the source centered at 2.09 μm , corresponding to a few optical cycles, with a brightness of 8.8 GHz/mW. Our results open new paths towards realization of ultrafast nanophotonic QIP.

4.1 Introduction

Entangled photon pairs (often referred to as biphotons) share non-classical correlations which can be leveraged to provide a quantum advantage in a variety of applications. The most mature and commercially available of these is quantum cryptography, namely in the form of quantum key distribution (QKD). First proposed with the BB84 protocol in 1984 [1], the correlations of polarization-entangled photons can be used to detect the presence of an eavesdropper attempting to intercept secure communications. When photons are allowed to pass from Alice (the sender) and Bob (the receiver) undisturbed, the entanglement between the pairs is preserved and their measurements will violate Bell's inequality. If an eavesdropper begins to interact with photons in transit, then the non-classical correlations will be destroyed, causing the successive measurements to follow Bell's inequality and alerting Alice and Bob that their communications have been compromised. Since BB84, improvements in photon sources and detection have led to the development of more sophisticated protocols capable of leveraging other forms of entanglement. Time-bin entangled photons have been used to prove secure communications through Franson interferometry [2, 3]. QKD has also been extended to so-called "continuous variable states" using measurements which directly probe the Heisenberg uncertainty relations [4]. Following in the footsteps of classical telecommunications, QKD schemes designed to take advantage of wavelength multiplexing have also been demonstrated [5].

As a result of the non-classical properties of entanglement, biphotons can also be used to obtain an advantage in sensing and measurement. In optical coherence tomography, biphotons have been used to enhance resolution by canceling the effects of dispersion in the medium under measurement [6]. Biphotons have also been used to overcome the diffraction limit in lithographic applications [7] and enhance performance in atomic state control applications [8]. Recently, a quantum advantage in computing has been demonstrated in which multiple biphoton sources are used to perform Gaussian boson sampling [9].

In recent years, TFLN has emerged as a leading candidate for biphoton sources for several reasons. The relatively large $\chi^{(2)}$ and mode overlap leads to high pair-generation efficiency as well as signal-to-noise. Ultrafast operation can be realized through tuning the waveguide geometry to achieve low GVM and GVD propagation. While our implementation currently relies on a table-top mode-locked laser, significant progress has been made in integrating short pulse sources on chip, especially in LN nanophotonics, with a 4.8-ps 10-GHz chip-scale mode-locked

laser demonstrated in [10] and a chip-scale electro-optic comb source with a 520-fs duration and a 30-GHz repetition rate demonstrated in [11].

There have been many successful demonstrations of broadband biphoton sources in TFLN [12, 13, 14]. However, these devices are still limited to the telecom wavelength range. Moreover, they have been demonstrated in the continuous-wave (CW) regime and have been unsuitable for ultrafast operation given their dispersive properties. Unlike the previous nanophotonic biphoton sources [15, 16, 17, 12, 18, 19, 20, 21, 22, 23], we utilize a near-zero dispersion regime for the realization of ultrashort-pulse photon pairs in nanophotonics. Operating in the 2- μm band in lithium niobate is particularly advantageous as it yields better fabrication tolerances compared with similar geometries for the 1550-nm band [24], and low GVD for both pump and signal simultaneously as well as the ability to match their group velocities and create strong temporal confinement for generated photon pairs [25].

Operation beyond the standard telecommunications band has several advantages for quantum applications. For instance, recent work on free-space QKD at 1550 nm has made a compelling case for moving to longer wavelengths to avoid limitations caused by solar irradiance [26]. Integrated photonics platforms can also benefit from operation at longer wavelengths because of lower scattering losses [27] and more efficient high-speed modulators [28, 29]. Classical and quantum networks are becoming practical in the 2- μm window given the progress on sources [30, 31], as well as low-dispersion and low-nonlinearity photonic crystal fibers [32, 33], and high-speed detectors [34]. Along with thulium/holmium amplifiers offering 40 THz of gain bandwidth [35], these technologies can facilitate the construction of wide area classical and quantum networks in the mid-IR. Quantum effects and secure communications have also been successfully demonstrated in the 2- μm band with Hong-Ou-Mandel visibility of 88.1% measured in bulk PPLN by [19] and polarization-based quantum key distribution implemented by [36] with a key rate of 0.254 bits/pair.

In this work, we present the first ultrafast biphoton source in nanophotonic PPLN capable of supporting ultra-short pulse propagation at both the pump and signal/idler wavelengths (Fig.4.1). Our source covers 17 THz of 3-dB bandwidth centered at 2.09 μm , and produces a 165-fs biphoton wavepacket at the output. Through 2 and 3-fold coincidence counting experiments, we demonstrate a coincidence-to-accidentals ratio (CAR) of 945, a pair generation rate of 8.8 GHz/mW or 440 kHz/mW/GHz, and a heralded $g_H^{(2)}(0)$ of 0.027, all of which are state-of-the-art for this wavelength

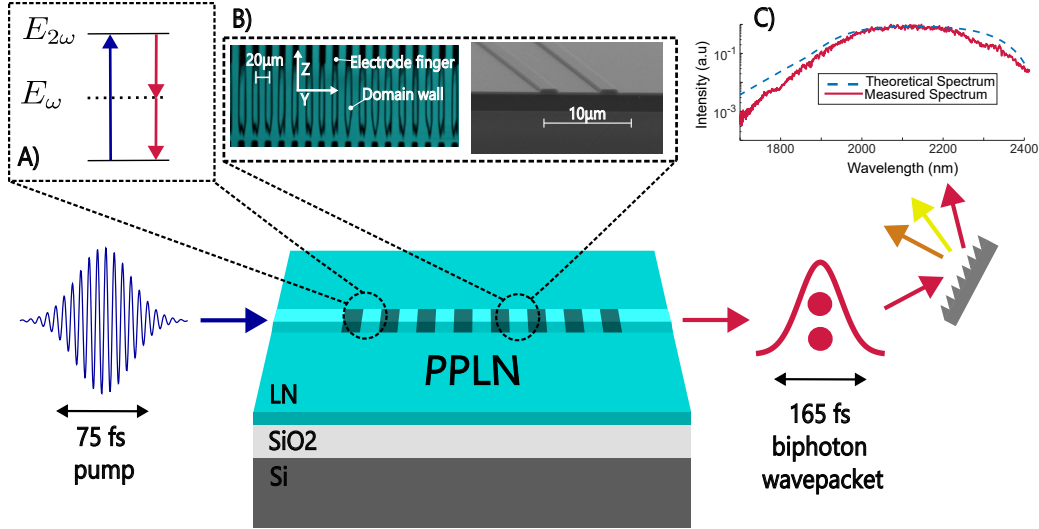


Figure 4.1: A diagram of the source operation. Femtosecond pump pulses are injected into a dispersion-engineered periodically poled lithium niobate (PPLN) waveguide to produce an ultrafast photon pair via type-0 spontaneous parametric down-conversion (SPDC). A) An illustration of the SPDC process used to generate photon pairs. B) 2-photon microscopy image of the poled region and an SEM of a representative device. C) The theoretical and measured SPDC spectra.

range in nanophotonics. Combined with the recent advances in ultrafast lithium niobate nanophotonics [37, 38, 39, 11], and the wide variety of high-performance components [40], our source demonstrates a practical path towards ultrafast on-chip QIP.

Biphoton Generation from OPAs

To generate biphotons, the OPA amplifies the vacuum field to produce pairs of entangled photons from single pump photon. Using the Hamiltonian introduced in chapter 2, we can time-evolve the vacuum field using the time-evolution operator:

$$U = e^{\frac{i}{\hbar}\hat{H}t} \quad (4.1)$$

We can approximate the low-gain regime in which the biphoton source operates by evaluating U at some small time step δt and then expanding U as follows:

$$\hat{U} \approx 1 + \sum_{n=0}^{\infty} \frac{i\delta t^n}{\hbar n!} \hat{H} \quad (4.2)$$

Since our biphoton source operates in the undepleted pump regime, we can reduce the pump operators in the Hamiltonian to their classical analog as follows:

$$\hat{H} \approx g(a^{\dagger 2} B + a^2 B^*) \quad (4.3)$$

where we have ignored the self-energy terms as they do not act on vacuum. In the poled region of the waveguide, the vacuum field evolves as follows:

$$\hat{U} |0\rangle = \frac{1}{\alpha} \left(|0\rangle + \frac{i\delta t g \sqrt{2}}{\hbar} |2\rangle + \frac{i\delta t^2 g \sqrt{3}}{\hbar} |4\rangle + \dots \right) \quad (4.4)$$

where α ensures normalization such that $\langle 0 | \hat{U}^\dagger \hat{U} | 0 \rangle = 1$. We note that the state is still mostly vacuum in superposition with even-numbered photon occupancy terms which exponentially decrease in amplitude. The term we are most interested in is the $\frac{i\delta t g \sqrt{2}}{\hbar} |2\rangle$ which represents the biphoton pair we wish to generate. It is important to note that while this state may not appear to have any inherent entanglement as we have written (i.e with just a single $| \rangle$ and not in a superposition), these photons still experience other forms of entanglement such as time-bin entanglement and spectrotemporal entanglement. We briefly mention time-bin entanglement in the context of Franson interferometry in chapter 2.

To obtain useful results from biphotons, we need to detect them pair-wise. All of the aforementioned experiments which employ biphotons to gain a quantum advantage use some flavor of coincidence detection such that only events where both photons were present are considered. While our photon source was experimentally operated at 250 MHz, the highest photon pair rates we measured at the detector were on the order of 100s of kHz. Two factors contribute to this. First, because the generated biphoton state is mostly vacuum, most laser pulses produce no photon pairs and hence these events are ignored. Second, when pairs are successfully produced, they are susceptible to both losses and detector inefficiency. Because we need both photons to click at the detector, our measured pair rate is proportional to the square of these losses. Both of these possibilities are ruled out with coincidence detection.

Another relevant consideration regarding this state is the presence of higher-order photon number terms such as $|4\rangle$, $|6\rangle$, etc. These terms represent the creation of so-called "multiphoton" events. Experimentally, these events lead to false coincidence counts which result in a reduced signal-to-noise ratio. These events can be avoided by lowering the pump power at the cost of a lower pair generation rate. We investigate

the impact of these multimode events later on in this chapter when we discuss the data analysis for coincidence-to-accidentals ratio measurements.

Device Design and Fabrication

Our source is designed for type-0 degenerate spontaneous parametric down-conversion (SPDC) while also optimizing the dispersion parameters for short-pulse propagation. Our waveguide design also minimizes the group-velocity mismatch between the pump and signal/idler wavelengths to minimize the temporal interaction window of the pump and generated photon pairs [41], allowing for the creation of an ultrashort signal/idler wavepacket. We target our waveguide design for conversion from a pump centered at $1.045 \mu\text{m}$ to a degenerate signal/idler pair at $2.09 \mu\text{m}$. The dispersion curves for our design are presented in Fig.4.2. We achieve a GVD of $135 \text{ fs}^2/\text{mm}$ and $60 \text{ fs}^2/\text{mm}$ for the pump and signal/idler respectively, and a GVM of $33 \text{ fs}/\text{mm}$. For comparison, bulk lithium niobate has a GVD of $246 \text{ fs}^2/\text{mm}$ for pump light, a GVD of $-56 \text{ fs}^2/\text{mm}$ for signal/idler photons, and a GVM of $115 \text{ fs}/\text{mm}$.

This near-zero GVM and GVD regime of operation leads to a broad spectrum of signal/idler pairs as shown in Fig.4.1 with a 3-dB bandwidth of 17 THz. For a 5-mm long device, we achieve a maximum temporal length for the signal/idler wavepacket of 165 fs. The duration of this wavepacket can be estimated from the temporal overlap of the pump pulse with the vacuum modes into which the waveguide phase-matching and dispersion permit SPDC. As the pump propagates down the waveguide and walks off in time from the $2 \mu\text{m}$ vacuum field, an large number of time-delayed vacuum modes within the walk-off window can experience the creation of a photon pair. The total wavepacket duration is approximated from the pump pulse duration and the total walk-off time resulting from the GVM using Eq.27(a) from [42]. Shorter gain windows, the gain being responsible for pair generation, for similar devices have been demonstrated in [43]. The temporal length of the photon pair can be directly measured using techniques developed in [44] and [45]. Substantial GVD at either the pump or signal/idler frequencies will also temporally broaden generated photon pairs either by increasing the effective temporal gain window or by dispersing photon pairs after their creation [46]. For 700-nm thick lithium-niobate on insulator (LNOI), achieving a large enough GVD necessary for the GVD to be the primary contribution to the temporal length of the photon pairs is generally difficult without resorting to extremely narrow waveguide geometries or deep etch depths. Therefore, our focus is on minimizing the GVM as this is the dominant contribution from the

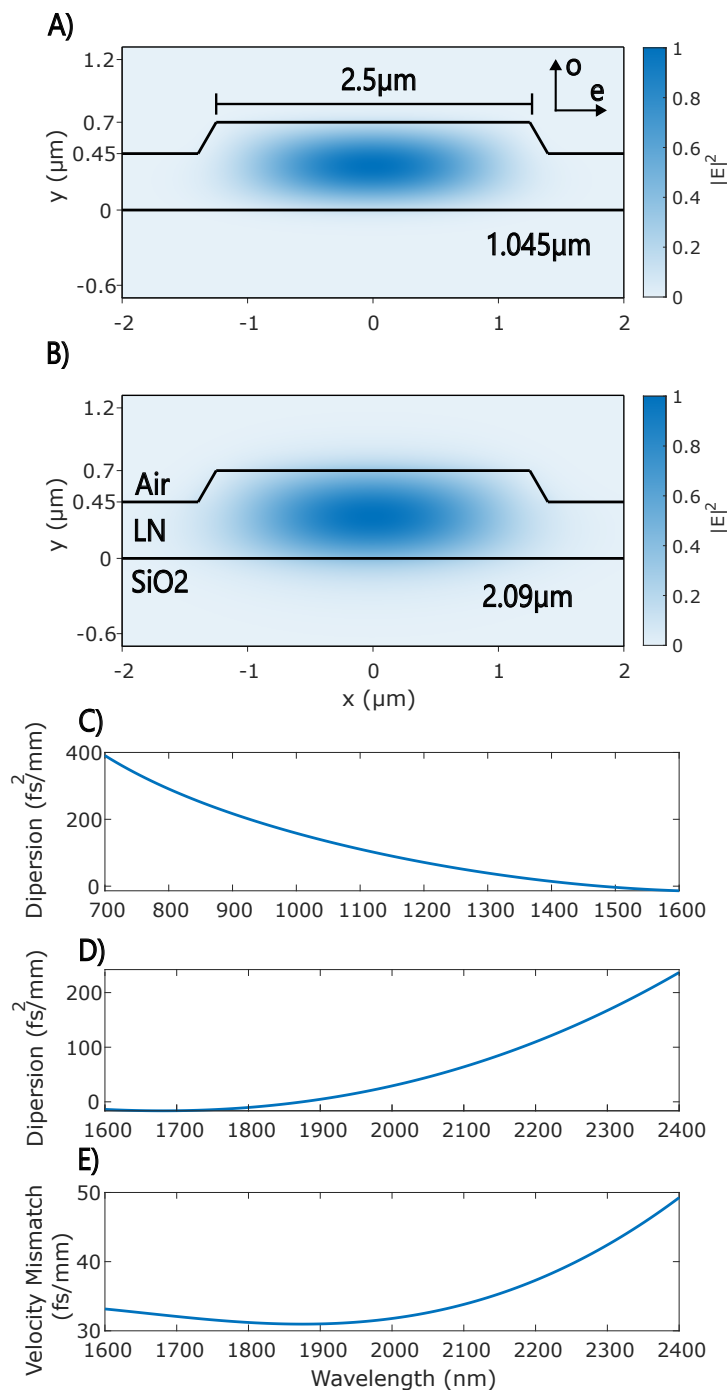


Figure 4.2: A) The quasi-TE waveguide mode for pump light at $1.045\ \mu\text{m}$. Arrows at the top right denote the ordinary and extraordinary material axes. B) The quasi-TE waveguide mode for signal light at $2.09\ \mu\text{m}$. C) Dispersion profile for the pump wavelength. D) Dispersion profile for the signal wavelength. E) Group velocity mismatch at different signal wavelengths relative to $1.045\ \mu\text{m}$.

waveguide geometry to our temporal length. There exist other geometries for LNOI that also experience low GVM and GVD thanks to the relaxed fabrication tolerances and flatter dispersion curves around 1 and 2 μm [25, 37].

We calculate the waveguide dispersion by first measuring the width and etch depth via atomic force microscopy, and then simulating the exact geometry with a mode-solver to find the effective refractive index, group velocity, and second-order dispersion. In addition to temporal confinement, the waveguide geometry spatially confines both the pump and signal/idler modes to the fundamental quasi-TE mode, providing a large mode overlap to increase the pair generation rate. The mode profiles are plotted in Fig.4.2A-B.

We fabricate our devices using commercially available thin-film lithium niobate on silica wafers from NANOLN, with a 700-nm thick X-cut thin-film on 4.7- μm thick SiO₂. We start by using electron beam lithography to pattern poling electrodes deposited via metal evaporation. After poling, we lithographically define and etch waveguides with dry Ar⁺ plasma. The inset of Fig.4.1B shows a 2-photon microscopy image of the poled region before etching as well as an SEM image of the waveguide facet at the edge of the chip.

4.2 Spectrotemporal Modes

While not the focus of this work, many recent works on photon-pair sources focus on using dispersion or poling domain engineering to minimize the number of temporal field-orthogonal modes [47] present in the output pairs [48, 49, 9, 50, 51]. The structure and occupancy of these modes can be found by performing a Bloch-Messiah decomposition on the joint-spectral intensity (JSI) of the signal and idler photons [52]. The JSI itself is estimated by the product of the energy conservation of the pump and the phase matching of the waveguide as a function of the signal and idler frequencies. A more detailed discussion of this process is presented in the supplementary. In the context of SPDC, minimization of the mode number is equivalent to removing the spectral correlations from the photon pairs. This creates indistinguishable photons, which are especially important for applications where multiple independent biphoton sources are combined [53, 54, 55, 56] as this indistinguishably leads to a stronger interference of single photons from different sources. Interference acts as a measurement of the relative mode of the two incoming photons. If both photons share the same mode, then they interfere strongly, whereas photons in different modes experience no interference. The visibility of the

interference between two independent but identical sources of biphotons is limited to approximately $\frac{1}{N}$ where N is the number of modes present [57].

Single-mode operation for the degenerate type-0 case without the use of filtering has remained elusive due to constraints stemming from the shape of the phase matching function as well as an inherent inability to satisfy the group velocity criteria used in [58, 48]. We estimate a Schmidt number of 16 from the decomposition of the JSI. For an ideal experiment with perfectly achromatic optics and detectors, this mode number will not limit the performance in CAR, generation rate, or heralded $g_H^{(2)}(0)$ of our source. In practice, the SNSPDs used for single photon detection experience a sharp fall-off in efficiency for increasing wavelength as does the transmissivity of the SMF-28 fibers leading up to them. We therefore perform all SNSPD measurements through a 48-nm bandpass filter centered at 2.09 μm to limit the impact of achromatic detection on our measurements. This reduces our mode number to 3. Using this filter during measurement prevents us from directly observing the total brightness of the source. Therefore, using a technique similar to [15], we calculate the total brightness by computing the ratio of the measured SPDC spectrum and the filter pass band. Multiplying the measured brightness by this ratio gives the total brightness.

The Schmidt number can be reduced by engineering the dispersion of the waveguide to meet certain group velocity mismatch requirements [58, 59], or by engineering the poling domains to remove fringes caused by the sinc^2 shape of the phase matching function provided by periodic poling [49, 48]. For degenerate SPDC in the type-0 configuration, reducing the mode number is challenging as the phase matching function runs parallel to the energy conservation of the pump near degeneracy, thereby causing the JSI to take on a narrow and inseparable elliptical shape. Filtering can also be employed to reduce the mode number as this limits measurements to a local region of the JSI. If the JSI is relatively constant in this region, then the source will appear to be single mode. This does however come at the cost of a reduced rate, as well as the introduction of a distinguishable thermal component into the state as a result of the presence of vacuum at one of the input ports of the filter [52].

4.3 Determining Losses via Parametric Generation

In order to accurately calculate the pair generation rate, we must know the pump power on-chip. We can measure the pump power off-chip before the reflective objective, and then infer the on-chip pump power by multiplying by the input loss. While the input loss cannot be directly measured, we can calculate it by measur-

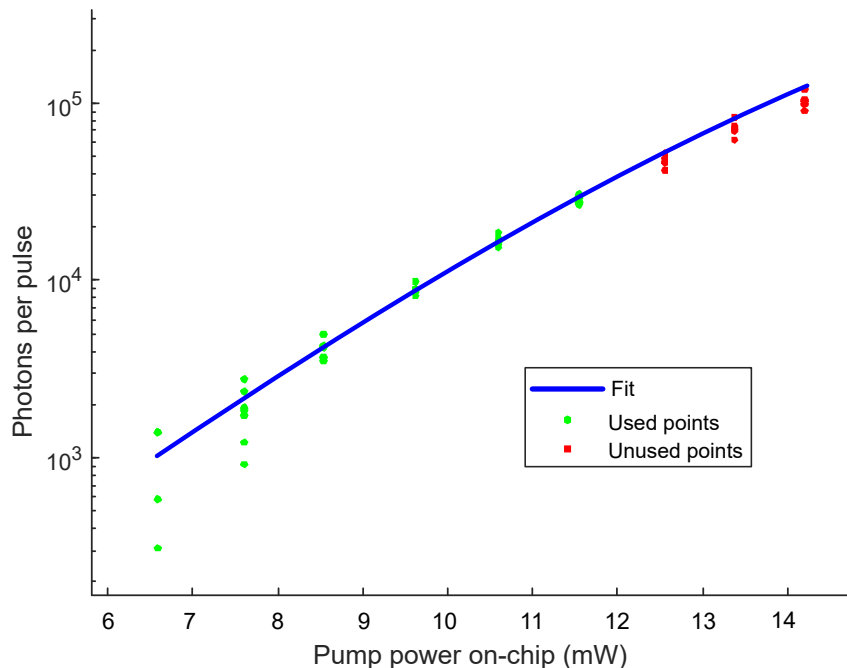


Figure 4.3: A plot of the average number of photons per pulse vs input pump power.

ing the throughput loss and subtracting the output loss to find the input loss. The throughput loss is measured by sending in $1 \mu\text{W}$ of pump power to avoid depletion effects, and then measuring the received power at the output. The output loss is calculated using the same methods presented in [37]. The output average photon number is first measured versus the input pump power. This curve is then fitted with the function $N_{avg} = \eta \sinh(\sqrt{\beta P})^2$ where η is the output loss and β is the nonlinear gain. Knowing the exact input loss is not necessary to compute η as changing the input loss (i.e changing the scale of the x-axis) will only affect the calculated value of β . After calculating the input loss, the curve can be fitted again with the correct x-axis to determine β .

Fig.4.3 shows the fitted photon number data. We extract a loss of 9 dB by fitting the raw data from 5 separate measurements. While this measurement gives the losses at $2 \mu\text{m}$, we know from fiber-in fiber-out chip coupling measurements that the loss at $1 \mu\text{m}$ is approximately 1 dB more than that for $2 \mu\text{m}$. Hence we conclude that the fiber coupling loss at $1 \mu\text{m}$ is 10 dB. Subtracting this from our throughput loss of 20 dB gives us 10 dB of input loss. Near the end of the curve, we have marked points in red which were not used in the fit. In the limit of large pump power, the assumptions underlying $N_{avg} = \eta \sinh(\sqrt{\beta P})^2$ are violated, and the depletion of the

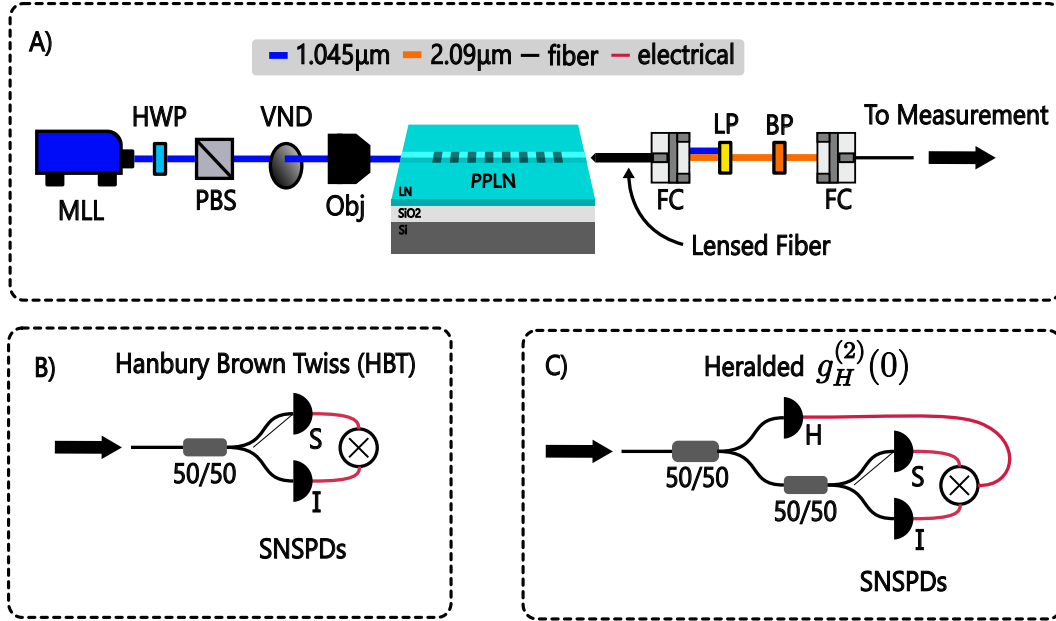


Figure 4.4: A) The experimental setup used to characterize the source. MLL is a 250-MHz 75-fs mode-locked laser centered at $1.045 \mu\text{m}$. HWP is a half-wave plate. PBS is a polarizing beam splitter. VND is a variable neutral density filter. Obj is a reflective objective. FC is a freespace to fiber coupler. LP is a low-pass filter. BP is a band-pass filter. SNSPDs are superconducting nanowire single photon detectors. 50/50 are balanced fiber beamsplitters. H, S, and I denote the heralding, signal, and idler channels respectively. B) Measurement setup for performing the Hanbury Brown-Twiss (HBT) experiment. C) Measurement setup for determining $g_H^{(2)}(0)$. The SEM image inset is of a representative device [37].

pump pulse causes the experimental data to deviate from the model.

4.4 Experimental Setup

The experimental setup used to characterize our biphoton source is shown in Fig. 4.4. A 75-fs 250-MHz mode-locked laser centered at $1.045 \mu\text{m}$ is directed through a motorized half-wave plate (HWP) and polarizing beam splitter (PBS) combination used to digitally control the input power to the experiment. Laser light is then collected and focused onto the input facet of the waveguide via a reflective objective to minimize dispersion. Inside the waveguide, photons from the pump are split into signal/idler pairs via degenerate type-0 SPDC. Light from the output facet is collected with a lensed PM-2000 fiber from OZ Optics. This fiber is directed into freespace with a reflective coupler and passed through one 1330-nm long pass filter, three 1500-nm long pass filters, and a 48-nm bandpass filter centered at $2.09 \mu\text{m}$ to provide 150 dB of pump rejection. The photon pairs are then coupled back into

fiber and passed through a series of fiber-coupled 50/50 splitters to perform Hanbury Brown-Twiss (HBT) and heralded $g_H^{(2)}(0)$ experiments for measuring the CAR, pair generation rate, and single photon behavior.

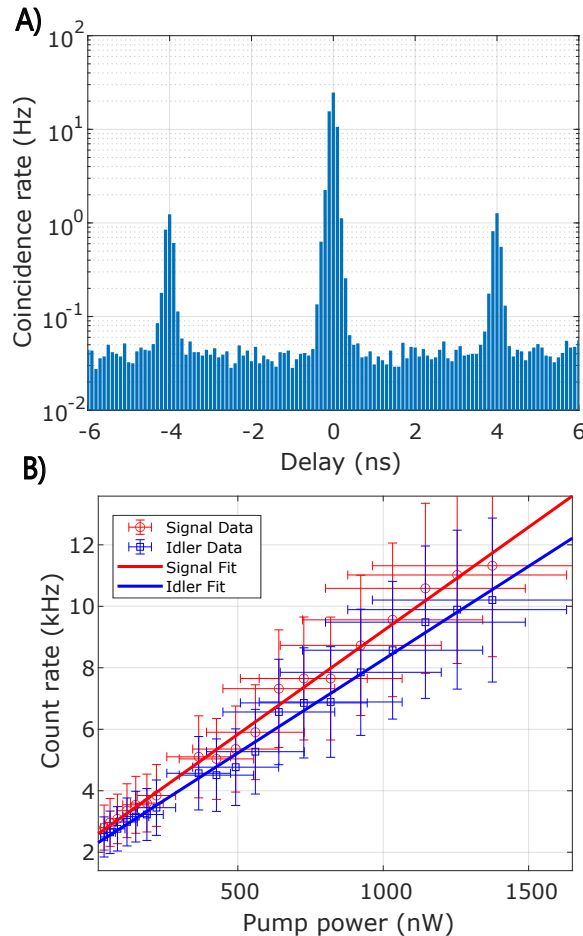


Figure 4.5: A) Example histogram from an HBT experiment taken at $11 \mu\text{W}$ of on-chip pump power. The main coincidence peak, caused by the detection of a signal/idler pair from the same generation event, is centered at 0-ns delay while accidentals peaks, caused by signal and idler photons created from consecutive and hence uncorrelated generation events, are present to the left and right at ± 4 ns. B) Count rates for the signal and idler channels compared with the fitted linear model.

4.5 Measurement and Data Processing

To assess the CAR and on-chip pair generation rate, an HBT experiment (Fig.4.4B) is performed by passing photon pairs from the chip into a 50/50 beamsplitter and looking for coincidences at the output ports using a pair of superconducting nanowire single photon detectors (SNSPDs) from IDQuantique. True coincidences are created by entangled pairs of photons hitting the detectors at the same time, whereas

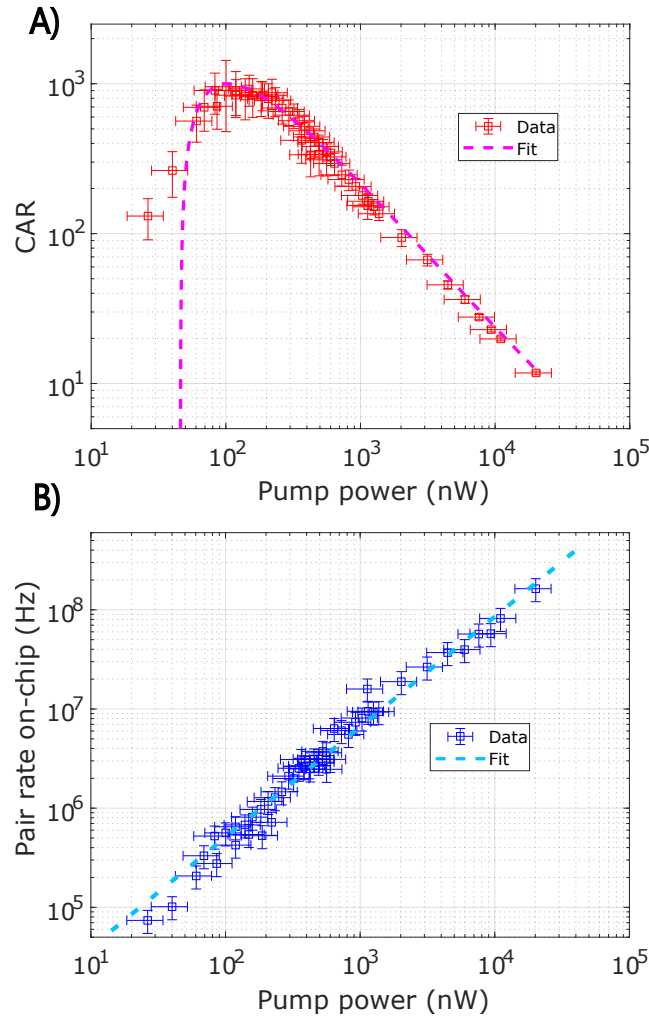


Figure 4.6: A) Coincidence-to-accidentals ratio (CAR) as a function of on-chip pump power. The fitted model is taken from [19]. B) On-chip pair generation rate as a function of on-chip pump power. This is the rate of pair generation at the output of the poled region of the waveguide. Pump input coupling losses are calculated based on a parametric gain measurement detailed in the supplementary.

accidentals are created by two photons from unrelated SNSPD processes causing coincidences. This is a measurement of the signal-to-noise ratio (SNR) of the detection system as the ratio of true to accidental coincidences is determined by the losses in the signal path, the dark count rates for the SNSPDs, and multi-photon generation events. Fig.4.5A shows a coincidence histogram collected by the time-to-digital converter recording events from the SNSPDs. The central peak at 0 ns is a result of both true and accidental coincidences, while side peaks are caused by accidentals. For a continuous-wave pump, accidental counts are spread evenly across the delay histogram. For the pulsed case, accidentals counts are localized to multiples of the

pump repetition time (4 ns in our case for our 250-MHz repetition rate). The CAR is defined as:

$$CAR = \frac{R_{si} - R_{acc}}{R_{acc}} \quad (4.5)$$

where R_{si} is the total coincidence peak count rate and R_{acc} is the accidental peak count rate. Error bars are calculated via the standard deviation of CAR calculated from different accidentals peaks. The timing jitter in the SNSPD measurement is limited by the jitter of the electronics (100 ps), resulting in coincidence and accidentals peaks which are much wider than the temporal width of the biphotons themselves. Fig.4.5B shows the count rates at the signal and idler detectors as a function of the on-chip pump power. By combining individual detector count rates with the coincidence count rates, the pair generation rate on-chip and detection efficiency for the signal and idler paths can be calculated from fitting the simplified linear model:

$$R_s = \epsilon P \eta_s + R_{d_s} \quad (4.6)$$

$$R_i = \epsilon P \eta_i + R_{d_i} \quad (4.7)$$

$$R_{si} = \frac{1}{2} \epsilon P \eta_s \eta_i \quad (4.8)$$

where $R_{s,i,si}$ are the signal, idler, and coincidence count rates respectively. P is the pump power in mW, ϵ is the generation rate in pairs per mW, $\eta_{s,i}$ are the losses for the signal and idler paths including detector efficiency, and $R_{d_{s,i}}$ is the dark count for the signal and idler detectors. The factor of $\frac{1}{2}$ in Eq.4 is the result of a lack of deterministic signal/idler separation in our experiment as they are degenerate in wavelength and polarization. This model is valid for small values of P where the pair generation rate is directly proportional to the input power for SPDC. To compute on-chip power for rate normalization, we measure the input loss by subtracting measurements of the output lensed fiber and throughput losses. The output loss for the lensed fiber is calculated by fitting the parametric generation output power vs pump power as detailed in the supplementary. Using this method, we calculate an output coupling loss of 9 dB from the chip to lensed fiber. The losses for additional components are measured with a 2 μ m diode laser. We measure 5 dB from the freespace filter, 3 dB from the transition from SM-2000 to SMF-28 fiber, and 6 dB from the SNSPD's detection efficiency for a total of 23 dB. This agrees well with

the measured total system efficiency of 25 ± 2 dB from fitting experimental data to equations 2, 3, and 4.

Fig.4.6A displays the measured CAR values vs the on-chip pump power which has been fitted with a model provided by [19]. At high pump powers, the CAR is limited by noise induced from multiphoton events generated by a strong pump pulse. As the pump power is lowered, the CAR increases until the maximum SNR is achieved. The CAR then decreases at lower pump powers due to a loss of signal altogether from the reduced pair generation rate. We measure a maximum CAR of 945 ± 475 at a pump power of 100 nW. The large variance is a result of the lack of prominent accidental peaks at low pump powers. The theoretical model used to fit the CAR vs power curve depends only on the pair generation rate, detector dark count rates, and system losses. A perfectly achromatic detection system would measure a higher CAR in the absence of the filter due to the higher observed pair generation rate. This is not the case for our system as our SNSPDs and fibers suffer higher losses at longer wavelengths, and therefore a bandpass filter in the measurement path increases our measured CAR by limiting the spectral dependence of the measurement efficiency to help satisfy the assumptions of the model. Fig.4.6B displays the measured on-chip pair generation rate as a function of the on-chip power. This is the rate at which generated photon pairs exit the poled region of the waveguide before incurring detection losses. We measure a slope of 8.8 ± 2.3 GHz/mW over the entire SPDC spectrum. Using our filter bandwidth, this normalizes to a pair-generation rate of 440 ± 115 kHz/mW/GHz.

In many applications requiring single photons, biphoton sources are used as a heralded source of single photons where the idler is detected to infer the presence of a single photon on the signal channel. To assess the performance of our biphoton source as a heralded single photon source, we measure $g_H^{(2)}(0)$ (Fig.4.4C). The heralded $g_H^{(2)}(0)$ is defined as:

$$g_H^{(2)}(0) = \frac{R_{HSI}R_H}{R_{HS}R_{HI}} = \frac{P_{HSI}}{P_{HS}P_{HI}} \quad (4.9)$$

where $R_{H,S,I}$ are the 2 and 3-fold coincidence rates of the heralding, signal, and idler detectors respectively. $P_{H,S,I}$ represent the probability for any given laser pulse to produce a click at the subscripted detectors [60]. Fig.4.7 shows the measured $g_H^{(2)}(0)$ as a function of the on-chip pump power. As the pump power decreases, $g_H^{(2)}(0)$ initially drops as fewer and fewer multiphoton events are observed. At

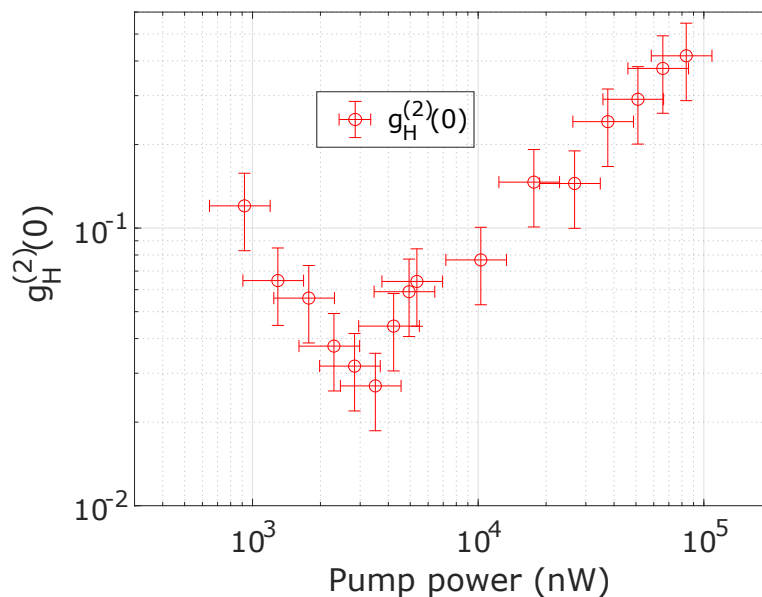


Figure 4.7: Heralded $g_H^{(2)}(0)$ of our source as a function of on-chip pump power.

very low pump powers, SNR is lost due to low count rates, causing $g_H^{(2)}(0)$ to rise again. We report a minimum $g_H^{(2)}(0)$ of 0.027 ± 0.0084 at a pump power of $3.5 \mu\text{W}$ on chip, showing that we can reliably herald single photons from our device using the measurement setup. This performance is competitive with state-of-the-art mid and near-IR sources (see table 1 in the supplementary). The CAR and $g_H^{(2)}(0)$ performance are maximized at two different pump powers because the $g_H^{(2)}(0)$ measurement uses 3 detectors (as opposed to 2 for CAR) and is therefore more susceptible to system losses, necessitating a higher power to maximize the system SNR. Increasing overall system losses would also shift the maximum CAR to a higher power as these losses translate to a lower overall signal.

4.6 Comparison and Discussion

Fig.4.8 compares a variety of different IR pair sources with our work. We include 1550-nm sources to demonstrate that not only does our device have state-of-the-art performance at $2 \mu\text{m}$, but it is also competitive with state-of-the-art devices for standard telecommunications bands. This allows for a more fair comparison of pair generation rate as most reported $2\text{-}\mu\text{m}$ sources utilize the $\chi^{(3)}$ instead of the $\chi^{(2)}$ nonlinearity, which has a normalized pair generation rate relative to mW^2 of pump power instead of mW . Table 1 in the supplementary goes into greater detail by normalizing the efficiency with the device length and bandwidth for an apples-to-apples

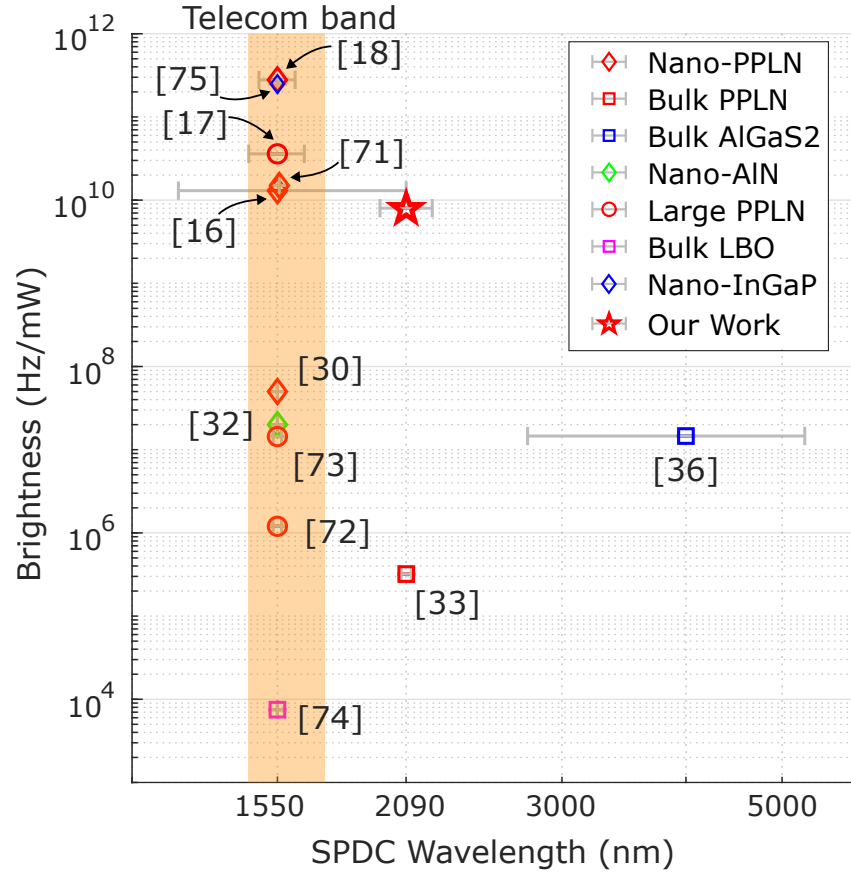


Figure 4.8: A comparison plot of relevant photon pair sources. Horizontal error bars represent the reported source bandwidth. Data for efficiency, wavelength, and bandwidth are taken from [12, 16, 14, 61] are PPLN ridge waveguides, similar to our device. [13, 62, 63] are larger ($>1\text{-}\mu\text{m}$ tall) PPLN waveguides. [19] is a bulk PPLN crystal. [22] is a bulk AlGaS2 crystal. [18] is a nanophotonic AIN ring resonator. [64] is a bulk LBO crystal. [65] is an InGaP ring resonator.

comparison. Looking at the last pair generation rate column ($\text{Hz}/\text{mW}/\text{cm}^2/\text{GHz}$), we see that our rate measurements agree well with other devices reported in literature except for one recent demonstration which exceeds the normalized pair generation of all other listed sources by an order of magnitude[14]. It should be noted that the pair generation rate will intrinsically be lower at $2\ \mu\text{m}$ compared to $1550\ \text{nm}$ as a result of the λ^{-4} dependence [25]. In the lower portion of the table which lists $2\text{-}\mu\text{m}$ sources, we see that our source exceeds the CAR, pair generation rate, and heralded $g_H^{(2)}(0)$ of the other recent $2\text{-}\mu\text{m}$ demonstrations in bulk crystals. We attribute this namely to the use of nanophotonic TFLN, which is responsible for the stronger nonlinear interactions given the device length, mode confinement, and dispersion engineering.

Detailed Comparison Table

Reference	Signal/Idler Wavelength	Platform	CAR	Pair Rate Hz/mW	Pair Rate $Hz/mW/GHz$	Pair Rate $Hz/mW/GHz/cm^2$	Heralded $g_H^{(2)}(0)$
[16]	1570nm/1570nm	5mm TFLN Waveguide	67000 ± 714	x	$460 \cdot 10^3$	$1.84 \cdot 10^6$	0.022 ± 0.004
[14]	1500nm/1500nm	6mm TFLN Waveguide	599	$279 \cdot 10^9$	$11.5 \cdot 10^6$	$31.9 \cdot 10^6$	x
[61]	1312nm/1557nm	40mm TFLN Waveguide	270000	$15 \cdot 10^9$	$3.1 \cdot 10^6$	$19 \cdot 10^3$	0.001
[17]	1530nm/1570nm	300 μ m TFLN Waveguide	6900 ± 200	x	$28.6 \pm 0.54 \cdot 10^3$	$3.18 \pm 0.06 \cdot 10^6$	x
[12]	1531nm/1571nm	5mm TFLN Waveguide	152710 ± 32772	$13 \cdot 10^9$	$324 \pm 25 \cdot 10^3$	$1.37 \pm 0.01 \cdot 10^6$	x
[13]	1578nm/1578nm	Large PPLN Waveguide	8000	$36 \cdot 10^9$	$1.43 \cdot 10^6$	$229 \cdot 10^3$	x
[62]	1550nm/1550nm	Large PPLN Waveguide	x	$1.2 \cdot 10^6$	160	17	x
[63]	1550nm/1550nm	Large PPLN Waveguide	x	$14.4 \cdot 10^6$	$1.9 \cdot 10^3$	213	x
[18]	1550nm/1550nm	AlN Ring Resonator	560	$20 \cdot 10^6$	$5.3 \cdot 10^6$	x	0.088 ± 0.004
[64]	1550nm/1550nm	Bulk LBO	x	$7.5 \cdot 10^3$	x	x	x
[65]	1550nm/1550nm	InGaP Ring Resonator	$1.4 \cdot 10^4$	$27.9 \cdot 10^9$	x	x	x
[15]	1572nm/1542nm	AlGaAs Ring Resonator	2697 ± 260	$20 \cdot 10^9$ *	$200 \cdot 10^9$ *	x	0.004 ± 0.01
[19]	2100nm/2100nm	1mm Bulk PPLN	180 ± 50	$320 \cdot 10^3$	x	x	x
[20]	1259nm/2015nm	Silicon-On-Insulator Waveguide	40.9 ± 9	$5.9 \cdot 10^6$ *	x	x	0.23 ± 0.08
[21]	1289nm/2000nm	Silicon-on-Insulator Waveguide	114 ± 4	$5.7 \cdot 10^3$ †*	x	x	x
[22]	700nm/6300nm	Bulk AgGaS ₂	706	$14.6 \cdot 10^6$	x	x	x
[23]	2000nm/2150nm	Silicon-on-Insulator Waveguide	25.7 ± 1.1	x	x	x	x
[36]	2080nm/2080nm	1mm Bulk PPLN	607 ± 185	$98.33 \cdot 10^3$	x	x	x
Our Work	2090nm/2090nm	5mm TFLN Waveguide	945 ± 475	$8.8 \pm 2.3 \cdot 10^9$	$440 \pm 115 \cdot 10^3$	$1.76 \pm 0.46 \cdot 10^6$	0.027 ± 0.003

Table 4.1: x = did not report. † = estimated based on reported data. * = units of per mW^2 .

Here we provide a more detailed comparison table which we reference in the main text. This table also includes $\chi^{(3)}$ sources which, while they constitute the majority of available mid-IR sources, are absent from the comparison plot as their rate scales as the square of the pump power instead of linearly as with $\chi^{(2)}$ sources.

4.7 Conclusion

We have demonstrated a dispersion engineered broadband biphoton source with a record breaking CAR, pair generation rate, and heralded $g_H^{(2)}(0)$ in the 2- μm window. The near-zero GVM and GVD operation of our source allows for use of ultrashort pulses, a crucial resource for realizing large-scale quantum information processing systems as the temporal confinement of these pulses can be used to both enhance the strength of nonlinear interactions as well as create well-defined time bins for temporal multiplexing of quantum gates beyond 1-THz clock speeds. Reduced solar irradiance near 2- μm combined with technological advancements in transmission and detection in the mid-IR make our source an ideal candidate for both freespace and fiber based quantum key distribution. Future work will revolve around characterizing the quantum interference, temporal width, and entanglement properties of the source through Hong-Ou-Mandel (HOM) and Franson interferometry. We plan to improve outcoupling losses via both on-chip adiabatic couplers for pump rejection and the use of an inverse tapered waveguide for better mode matching with a lensed fiber. Using in-house adiabatic coupler designs and state-of-the-art inverse tapers [66], we can lower the output coupling losses to 0.32 dB and filter losses to 3 dB for a total detection loss of 9.32 dB.

4.8 Acknowledgments and Disclosures

Device nanofabrication was performed at the Kavli Nanoscience Institute (KNI) at Caltech. The authors gratefully acknowledge support from ARO grant no. W911NF-23-1-0048, NSF grant no. 1846273 and 1918549, AFOSR award FA9550-20-1-0040, the center for sensing to intelligence at Caltech, and NASA/JPL. The authors wish to thank NTT Research for their financial support. All authors have accepted responsibility for the entire content of this manuscript and approved its submission. L.L. and A.M. are involved in developing photonic integrated nonlinear circuits at PINC Technologies Inc. L.L. and A.M. have an equity interest in PINC Technologies Inc. The other authors declare that they have no competing interests. Informed consent was obtained from all individuals included in this study. The conducted research is not related to either human or animals use. Data sets used in this thesis

are available from the author upon request.

References

- [1] Charles H Bennett and Gilles Brassard. “Quantum cryptography: Public key distribution and coin tossing”. In: *Theoretical computer science* 560 (2014), pp. 7–11.
- [2] Tian Zhong, Hongchao Zhou, Robert D Horansky, Catherine Lee, Varun B Verma, Adriana E Lita, Alessandro Restelli, Joshua C Bienfang, Richard P Mirin, Thomas Gerrits, et al. “Photon-efficient quantum key distribution using time–energy entanglement with high-dimensional encoding”. In: *New Journal of Physics* 17.2 (2015), p. 022002.
- [3] Irfan Ali-Khan, Curtis J Broadbent, and John C Howell. “Large-alphabet quantum key distribution using energy-time entangled bipartite states”. In: *Physical review letters* 98.6 (2007), p. 060503.
- [4] Pu Wang, Xuyang Wang, and Yongmin Li. “Security analysis of unidimensional continuous-variable quantum key distribution using uncertainty relations”. In: *Entropy* 20.3 (2018), p. 157.
- [5] Ken-ichiro Yoshino, Mikio Fujiwara, Akihiro Tanaka, Seigo Takahashi, Yoshihiro Nambu, Akihisa Tomita, Shigehito Miki, Taro Yamashita, Zhen Wang, Masahide Sasaki, et al. “High-speed wavelength-division multiplexing quantum key distribution system”. In: *Optics letters* 37.2 (2012), pp. 223–225.
- [6] Ayman F Abouraddy, Magued B Nasr, Bahaa EA Saleh, Alexander V Sergienko, and Malvin C Teich. “Quantum-optical coherence tomography with dispersion cancellation”. In: *Physical Review A* 65.5 (2002), p. 053817.
- [7] E Pavel, SI Jinga, BS Vasile, A Dinescu, V Marinescu, R Trusca, and N Tosa. “Quantum optical lithography from 1 nm resolution to pattern transfer on silicon wafer”. In: *Optics & Laser Technology* 60 (2014), pp. 80–84.
- [8] Barak Dayan, Avi Pe’Er, Asher A Friesem, and Yaron Silberberg. “Two photon absorption and coherent control with broadband down-converted light”. In: *Physical review letters* 93.2 (2004), p. 023005.
- [9] Han-Sen Zhong, Hui Wang, Yu-Hao Deng, Ming-Cheng Chen, Li-Chao Peng, Yi-Han Luo, Jian Qin, Dian Wu, Xing Ding, Yi Hu, et al. “Quantum computational advantage using photons”. In: *Science* 370.6523 (2020), pp. 1460–1463.
- [10] Qiushi Guo, Benjamin K Gutierrez, Ryoto Sekine, Robert M Gray, **James Williams** A, Luis Ledezma, Luis Costa, Arkadev Roy, Selina Zhou, Mingchen Liu, et al. “Ultrafast mode-locked laser in nanophotonic lithium niobate”. In: *Science* 382.6671 (2023), pp. 708–713.

- [11] Mengjie Yu, David Barton III, Rebecca Cheng, Christian Reimer, Prashanta Kharel, Lingyan He, Linbo Shao, Di Zhu, Yaowen Hu, Hannah R Grant, et al. “Integrated femtosecond pulse generator on thin-film lithium niobate”. In: *Nature* 612.7939 (2022), pp. 252–258.
- [12] Usman A Javid, Jingwei Ling, Jeremy Staffa, Mingxiao Li, Yang He, and Qiang Lin. “Ultrabroadband entangled photons on a nanophotonic chip”. In: *Physical Review Letters* 127.18 (2021), p. 183601.
- [13] Yuting Zhang, Hao Li, Tingting Ding, Yiwen Huang, Longyue Liang, Xuerui Sun, Yongzhi Tang, Jiayu Wang, Shijie Liu, Yuanlin Zheng, et al. “Scalable, fiber-compatible lithium-niobate-on-insulator micro-waveguides for efficient nonlinear photonics”. In: *Optica* 10.6 (2023), pp. 688–693.
- [14] Guang-Tai Xue, Yun-Fei Niu, Xiaoyue Liu, Jia-Chen Duan, Wenjun Chen, Ying Pan, Kunpeng Jia, Xiaohan Wang, Hua-Ying Liu, Yong Zhang, et al. “Ultrabright multiplexed energy-time-entangled photon generation from lithium niobate on insulator chip”. In: *Physical Review Applied* 15.6 (2021), p. 064059.
- [15] Trevor J Steiner, Joshua E Castro, Lin Chang, Quynh Dang, Weiqiang Xie, Justin Norman, John E Bowers, and Galan Moody. “Ultrabright entangled-photon-pair generation from an Al Ga As-On-insulator microring resonator”. In: *PRX Quantum* 2.1 (2021), p. 010337.
- [16] Jie Zhao, Chaoxuan Ma, Michael Rüsing, and Shayan Mookherjea. “High quality entangled photon pair generation in periodically poled thin-film lithium niobate waveguides”. In: *Physical review letters* 124.16 (2020), p. 163603.
- [17] Bradley S Elkus, Kamal Abdelsalam, Ashutosh Rao, Vesselin Velez, Sasan Fathpour, Prem Kumar, and Gregory S Kanter. “Generation of broadband correlated photon-pairs in short thin-film lithium-niobate waveguides”. In: *Optics express* 27.26 (2019), pp. 38521–38531.
- [18] Xiang Guo, Chang-ling Zou, Carsten Schuck, Hojoong Jung, Risheng Cheng, and Hong X Tang. “Parametric down-conversion photon-pair source on a nanophotonic chip”. In: *Light: Science & Applications* 6.5 (2017), e16249–e16249.
- [19] Shashi Prabhakar, Taylor Shields, Adetunmise C Dada, Mehdi Ebrahim, Gregor G Taylor, Dmitry Morozov, Kleanthis Erotokritou, Shigehito Miki, Masahiro Yabuno, Hirotaka Terai, et al. “Two-photon quantum interference and entanglement at 2.1 μm ”. In: *Science advances* 6.13 (2020), eaay5195.
- [20] S Signorini, M Sanna, S Piccione, M Ghulinyan, P Tidemand-Lichtenberg, C Pedersen, and L Pavesi. “A silicon source of heralded single photons at 2 μm ”. In: *APL Photonics* 6.12 (2021), p. 126103.

- [21] M Sanna, D Rizzotti, S Signorini, and L Pavesi. “An integrated entangled photons source for mid-infrared ghost spectroscopy”. In: *Quantum Sensing and Nano Electronics and Photonics XVIII*. Vol. 12009. SPIE. 2022, pp. 143–151.
- [22] Mohit Kumar, Pawan Kumar, Andres Vega, Maximilian A Weissflog, Thomas Pertsch, and Frank Setzpfandt. “Mid-infrared photon pair generation in Ag-GaS₂”. In: *Applied Physics Letters* 119.24 (2021), p. 244001.
- [23] Lawrence M Rosenfeld, Dominic A Sulway, Gary F Sinclair, Vikas Anant, Mark G Thompson, John G Rarity, and Joshua W Silverstone. “Mid-infrared quantum optics in silicon”. In: *Optics Express* 28.25 (2020), pp. 37092–37102.
- [24] Paulina S Kuo. “Towards noncritical phasematching in thin-film lithium niobate waveguides”. In: *Nonlinear Frequency Generation and Conversion: Materials and Devices XXI*. Vol. 11985. SPIE. 2022, pp. 60–67.
- [25] Marc Jankowski, Jatadhari Mishra, and MM Fejer. “Dispersion-engineered nanophotonics: a flexible tool for nonclassical light”. In: *Journal of Physics: Photonics* 3.4 (2021), p. 042005.
- [26] Sheng-Kai Liao, Hai-Lin Yong, Chang Liu, Guo-Liang Shentu, Dong-Dong Li, Jin Lin, Hui Dai, Shuang-Qiang Zhao, Bo Li, Jian-Yu Guan, et al. “Long-distance free-space quantum key distribution in daylight towards inter-satellite communication”. In: *Nature Photonics* 11.8 (2017), pp. 509–513.
- [27] David E Hagan and Andrew P Knights. “Mechanisms for optical loss in SOI waveguides for mid-infrared wavelengths around 2 μm ”. In: *Journal of Optics* 19.2 (2016), p. 025801.
- [28] Wei Cao, David Hagan, David J Thomson, Milos Nedeljkovic, Callum G Littlejohns, Andy Knights, Shaif-Ul Alam, Junjia Wang, Frederic Gardes, Weiwei Zhang, et al. “High-speed silicon modulators for the 2 μm wavelength band”. In: *Optica* 5.9 (2018), pp. 1055–1062.
- [29] Muhammad Usman Sadiq, Hongyu Zhang, James O’Callaghan, Brendan Roycroft, Niamh Kavanagh, Kevin Thomas, Agnieszka Gocalinska, Yong Chen, Tom Bradley, John R Hayes, et al. “40 Gb/s WDM transmission over 1.15-km HC-PBGF using an InP-based Mach-Zehnder modulator at 2 μm ”. In: *Journal of Lightwave Technology* 34.8 (2016), pp. 1706–1711.
- [30] Richard Phelan, Michael Gleeson, Diarmuid Byrne, John O’Carroll, Marta Nawrocka, Kevin Carney, Rob Lennox, Lina Maigyte, Phil Long, Chris Herbert, et al. “High power narrow linewidth discrete mode laser diode integrated with a curved semiconductor optical amplifier emitting at 2051 nm”. In: *Applied Optics* 57.22 (2018), E1–E5.

- [31] Cheng-Ao Yang, Sheng-Wen Xie, Yi Zhang, Jin-Ming Shang, Shu-Shan Huang, Ye Yuan, Fu-Hui Shao, Yu Zhang, Ying-Qiang Xu, and Zhi-Chuan Niu. “High-power, high-spectral-purity GaSb-based laterally coupled distributed feedback lasers with metal gratings emitting at $2\ \mu\text{m}$ ”. In: *Applied Physics Letters* 114.2 (2019).
- [32] Erik Agrell, Magnus Karlsson, AR Chraplyvy, David J Richardson, Peter M Krummrich, Peter Winzer, Kim Roberts, Johannes Karl Fischer, Seb J Savory, Benjamin J Eggleton, et al. “Roadmap of optical communications”. In: *Journal of Optics* 18.6 (2016), p. 063002.
- [33] DJ Richardson. “New optical fibres for high-capacity optical communications”. In: *Philosophical Transactions of the Royal Society A: Mathematical, Physical and Engineering Sciences* 374.2062 (2016), p. 20140441.
- [34] Nan Ye, Hua Yang, Michael Gleeson, Nicola Pavarelli, Hongyu Zhang, James O’Callaghan, Wei Han, Noreen Nudds, Sean Collins, Agnieszka Gocalinska, et al. “InGaAs Surface Normal Photodiode for $2\ \mu\text{m}$ Optical Communication Systems”. In: *IEEE Photonics Technology Letters* 27.14 (2015), pp. 1469–1472.
- [35] Zhihong Li, AM Heidt, JMO Daniel, Yongmin Jung, Shaif-Ul Alam, and David J Richardson. “Thulium-doped fiber amplifier for optical communications at $2\ \mu\text{m}$ ”. In: *Optics Express* 21.8 (2013), pp. 9289–9297.
- [36] Adetunmise C Dada, Jędrzej Kaniewski, Corin Gawith, Martin Lavery, Robert H Hadfield, Daniele Faccio, and Matteo Clerici. “Near-Maximal Two-Photon Entanglement for Optical Quantum Communication at $2.1\ \mu\text{m}$ ”. In: *Physical Review Applied* 16.5 (2021), p. L051005.
- [37] Luis Ledezma, Ryoto Sekine, Qiushi Guo, Rajveer Nehra, Saman Jahani, and Alireza Marandi. “Intense optical parametric amplification in dispersion-engineered nanophotonic lithium niobate waveguides”. In: *Optica* 9.3 (2022), pp. 303–308.
- [38] Rajveer Nehra, Ryoto Sekine, Luis Ledezma, Qiushi Guo, Robert M Gray, Arkadev Roy, and Alireza Marandi. “Few-cycle vacuum squeezing in nanophotonics”. In: *Science* 377.6612 (2022), pp. 1333–1337.
- [39] Qiushi Guo, Ryoto Sekine, Luis Ledezma, Rajveer Nehra, Devin J Dean, Arkadev Roy, Robert M Gray, Saman Jahani, and Alireza Marandi. “Femtojoule femtosecond all-optical switching in lithium niobate nanophotonics”. In: *Nature Photonics* 16.9 (2022), pp. 625–631.
- [40] Di Zhu, Linbo Shao, Mengjie Yu, Rebecca Cheng, Boris Desiatov, CJ Xin, Yaowen Hu, Jeffrey Holzgrafe, Soumya Ghosh, Amirhassan Shams-Ansari, et al. “Integrated photonics on thin-film lithium niobate”. In: *Advances in Optics and Photonics* 13.2 (2021), pp. 242–352.

- [41] Aron Vanselow, Paul Kaufmann, Helen M Chrzanowski, and Sven Ramelow. “Ultra-broadband SPDC for spectrally far separated photon pairs”. In: *Optics letters* 44.19 (2019), pp. 4638–4641.
- [42] Wojciech Wasilewski, Alexander I Lvovsky, Konrad Banaszek, and Czesław Radzewicz. “Pulsed squeezed light: Simultaneous squeezing of multiple modes”. In: *Physical Review A* 73.6 (2006), p. 063819.
- [43] Gordon HY Li, Ryoto Sekine, Rajveer Nehra, Robert M Gray, Luis Ledezma, Qiushi Guo, and Alireza Marandi. “All-optical ultrafast ReLU function for energy-efficient nanophotonic deep learning”. In: *Nanophotonics* 12.5 (2022), pp. 847–855.
- [44] S Sensarn, GY Yin, and SE Harris. “Generation and compression of chirped biphotons”. In: *Physical review letters* 104.25 (2010), p. 253602.
- [45] Maria V Chekhova, Semen Germanskiy, Dmitri B Horoshko, Galiya Kh Kitaeva, Mikhail I Kolobov, Gerd Leuchs, Chris R Phillips, and Pavel A Prudkovskii. “Broadband bright twin beams and their upconversion”. In: *Optics letters* 43.3 (2018), pp. 375–378.
- [46] F Roeder, R Pollmann, M Stefszky, M Santandrea, K-H Luo, V Quiring, R Ricken, C Eigner, B Brecht, and C Silberhorn. “Measurement of ultrashort bi-photon correlation times with an integrated two-colour broadband SU (1, 1)-interferometer”. In: *arXiv preprint arXiv:2310.04293* (2023).
- [47] Benjamin Brecht, Dileep V Reddy, Christine Silberhorn, and Michael G Raymer. “Photon temporal modes: a complete framework for quantum information science”. In: *Physical Review X* 5.4 (2015), p. 041017.
- [48] CJ Xin, Jatadhari Mishra, Changchen Chen, Di Zhu, Amirhassan Shams-Ansari, Carsten Langrock, Neil Sinclair, Franco NC Wong, MM Fejer, and Marko Lončar. “Spectrally separable photon-pair generation in dispersion engineered thin-film lithium niobate”. In: *Optics Letters* 47.11 (2022), pp. 2830–2833.
- [49] P Ben Dixon, Jeffrey H Shapiro, and Franco NC Wong. “Spectral engineering by Gaussian phase-matching for quantum photonics”. In: *Optics express* 21.5 (2013), pp. 5879–5890.
- [50] Peter J Mosley, Jeff S Lundeen, Brian J Smith, Piotr Wasylczyk, Alfred B U’Ren, Christine Silberhorn, and Ian A Walmsley. “Heralded generation of ultrafast single photons in pure quantum states”. In: *Physical Review Letters* 100.13 (2008), p. 133601.
- [51] Francesco Graffitti, Peter Barrow, Massimiliano Proietti, Dmytro Kundys, and Alessandro Fedrizzi. “Independent high-purity photons created in domain-engineered crystals”. In: *Optica* 5.5 (2018), pp. 514–517.

- [52] Martin Houde and Nicolás Quesada. “Waveguided sources of consistent, single-temporal-mode squeezed light: The good, the bad, and the ugly”. In: *AVS Quantum Science* 5.1 (2023).
- [53] Pieter Kok, William J Munro, Kae Nemoto, Timothy C Ralph, Jonathan P Dowling, and Gerard J Milburn. “Linear optical quantum computing with photonic qubits”. In: *Reviews of modern physics* 79.1 (2007), p. 135.
- [54] Peter C Humphreys, Benjamin J Metcalf, Justin B Spring, Merritt Moore, Xian-Min Jin, Marco Barbieri, W Steven Kolthammer, and Ian A Walmsley. “Linear optical quantum computing in a single spatial mode”. In: *Physical review letters* 111.15 (2013), p. 150501.
- [55] H-J Briegel, Wolfgang Dür, Juan I Cirac, and Peter Zoller. “Quantum repeaters: the role of imperfect local operations in quantum communication”. In: *Physical Review Letters* 81.26 (1998), p. 5932.
- [56] Justin B Spring, Benjamin J Metcalf, Peter C Humphreys, W Steven Kolthammer, Xian-Min Jin, Marco Barbieri, Animesh Datta, Nicholas Thomas-Peter, Nathan K Langford, Dmytro Kundys, et al. “Boson sampling on a photonic chip”. In: *Science* 339.6121 (2013), pp. 798–801.
- [57] Christopher L Morrison, Francesco Graffitti, Peter Barrow, Alexander Pickston, Joseph Ho, and Alessandro Fedrizzi. “Frequency-bin entanglement from domain-engineered down-conversion”. In: *APL Photonics* 7.6 (2022).
- [58] Warren P Grice, Alfred B U’Ren, and Ian A Walmsley. “Eliminating frequency and space-time correlations in multiphoton states”. In: *Physical Review A* 64.6 (2001), p. 063815.
- [59] Alfred B U’Ren, Christine Silberhorn, Reinhard Erdmann, Konrad Banaszek, Warren P Grice, Ian A Walmsley, and Michael G Raymer. “Generation of pure-state single-photon wavepackets by conditional preparation based on spontaneous parametric downconversion”. In: *arXiv preprint quant-ph/0611019* (2006).
- [60] S Signorini and L Pavesi. “On-chip heralded single photon sources”. In: *AVS Quantum Science* 2.4 (2020).
- [61] Matthias Bock, Andreas Lenhard, Christopher Chunnillall, and Christoph Becher. “Highly efficient heralded single-photon source for telecom wavelengths based on a PPLN waveguide”. In: *Optics express* 24.21 (2016), pp. 23992–24001.
- [62] A Yoshizawa, R Kaji, and H Tsuchida. “Generation of polarisation-entangled photon pairs at 1550 nm using two PPLN waveguides”. In: *Electronics Letters* 39.7 (2003), p. 1.

- [63] Shigehiko Mori, Jonas Söderholm, Naoto Namekata, and Shuichiro Inoue. “On the distribution of 1550-nm photon pairs efficiently generated using a periodically poled lithium niobate waveguide”. In: *Optics communications* 264.1 (2006), pp. 156–162.
- [64] Tae-Gon Noh, Heonoh Kim, Chun Ju Youn, Seok-Beom Cho, Jongcheol Hong, Taehyoung Zyung, and Jaewan Kim. “Noncollinear correlated photon pair source in the 1550 nm telecommunication band”. In: *Optics express* 14.7 (2006), pp. 2805–2810.
- [65] Mengdi Zhao and Kejie Fang. “InGaP quantum nanophotonic integrated circuits with 1.5% nonlinearity-to-loss ratio”. In: *Optica* 9.2 (2022), pp. 258–263.
- [66] Ni Yao, Junxia Zhou, Renhong Gao, Jintian Lin, Min Wang, Ya Cheng, Wei Fang, and Limin Tong. “Efficient light coupling between an ultra-low loss lithium niobate waveguide and an adiabatically tapered single mode optical fiber”. In: *Optics express* 28.8 (2020), pp. 12416–12423.

*Chapter 5***ULTRAFAST SINGLE-PHOTON DETECTION USING
NANOPHOTONIC PARAMETRIC AMPLIFIERS**

Elina Sendonaris, **James Williams**, Rajveer Nehra, Robert M Gray, Ryoto Sekine, Luis Ledezma, and Alireza Marandi (2024) Ultrafast single-photon detection using nanophotonic parametric amplifiers. arXiv preprint arXiv:2410.18397.

ABSTRACT

Integrated photonic quantum information processing (QIP) has advanced rapidly due to progress in various nanophotonic platforms. Single photon detectors have been the subject of intense study due to their ubiquity in QIP systems, yet many state-of-the-art detectors operate at cryogenic temperatures under vacuum and suffer from long dead times. We propose and demonstrate a single photon detection scheme based on optical parametric amplification in nanophotonic lithium niobate (LN) combined with a macroscopic photodetector. We use quantum detector tomography to experimentally demonstrate an efficiency of 26.5% with a 2.2% dark count rate. We show that by improving the nonlinearity-to-loss ratio in nanophotonics and using homodyne detection on a squeezed pump, the detector can achieve 69% efficiency with 0.9% dark count rate. The detector operates at room temperature, has a dead time limited only by its dispersion and pump pulse length, and is readily integrated in LN nanophotonics, in which many other components of photonic QIP are available. Our results represent a step towards all-optical ultrafast single photon detection for scalable nanophotonic QIP.

5.1 Main

Photonic QIP has been the subject of intense research as the relative absence of thermal noise at optical frequencies translates to a relatively long coherence time for optical photons. Particularly, QIP systems such as measurement-based quantum computing [1, 2, 3], quantum computing with linear optics [4, 5, 6], and quantum simulations [7] are all based on quantum information stored in photons. These systems contain three crucial elements: state generation, state manipulation, and detection. Single photon detectors (SPDs) are the most widely used detectors in photonic QIP, for both determining the outcome of a computation in discrete-variable (DV) QIP [4, 8] and for generating non-Gaussian states, necessary for universal continuous-variable (CV) QIP [9, 10], such as Schrödinger cat and kitten states [11] and GKP states [12, 13]. However, high-performance single photon detection remains challenging to implement because of the need to achieve extreme sensitivity and fast operation while avoiding false detection events [14].

Some of the most widely used single photon detectors include superconducting nanowire single photon detectors (SNSPDs) [15], transition-edge sensors (TESs) [16], and single photon avalanche detectors (SPADs) [17]. SNSPDs benefit from their high efficiency [18, 19], large electronic bandwidths [20, 21], low dark count rates [22], and low timing jitter [23]. However, they suffer from long dead times and operate at cryogenic temperatures and under vacuum. TESs also operate in cryogenic vacuum conditions and can distinguish between different numbers of photons while having high efficiencies but lack short reset times compared to SNSPDs [16, 24]. SPADs operate at room temperature and pressure but tend to have higher dark count rates and lower efficiencies than SNSPDs [17]. For all of these detectors, the wavelength range at which they operate is limited by the materials used, and their performance drops off at wavelengths longer than near-infrared (NIR).

Moving QIP systems to integrated photonics is of growing interest due to the stability and compactness of the components as well as the scalability in manufacturing [25, 26, 27]. Quantum photonics can benefit from the low loss and strong light-matter interaction offered by integrated platforms [28, 29]. Currently, single photons on photonic chips are detected either by outcoupling them to SPDs off-chip [30] or integrating the detector onto the photonic chip itself and placing it in a cryostat [31]. However, outcoupling photons from a chip leads to a lower total detection efficiency due to the outcoupling loss, and integrating an SNSPD on chip creates fabrication and performance challenges, especially when scaling device size given the spatial

constraints of typical cryostats.

In this work, we utilize ultrahigh gain nanophotonic OPAs to experimentally realize a room-temperature single photon OPA detector (OPAD), and analyze its prospects for QIP. Spatial confinement in nanophotonics combined with dispersion engineering enables us to use ultrashort pulses with high peak intensity, leading to stronger nonlinear interaction with an inherent dark time limited only by the $\chi^{(2)}$ response (typically less than 1 fs), dispersion of the device, and pump pulse length. Recently, nanophotonic optical parametric amplifiers (OPAs) with gains of up to 100 dB/cm have been demonstrated [32], opening up new avenues for quantum state engineering and measurement [33, 34, 35, 36]. Optical parametric amplification has been used to both generate and measure squeezing over large bandwidths [37, 33, 35]. Here, we extend the use of OPAs into single-photon detection and analyze the OPAD's performance using the positive operator-valued measure (POVM) framework and quantum detector tomography [38]. We experimentally implement such a detector using a periodically poled thin-film lithium niobate (TFLN) waveguide OPA and a fast InGaAs photodetector. We also present an advanced variant of the OPAD and show through simulations that Schrödinger's kitten states can be created using such an OPAD for photon subtraction from squeezed vacuum.

Figure 5.1(a) shows the concept of the OPAD: an OPA followed by a macroscopic detector (which we term a classical detector). We consider two macroscopic detection methods: a photodetector and a homodyne detector on the pump after the OPA [39]. In both detection schemes, we define a thresholding criteria for a click, as shown in Fig. 5.1(b,c). For a single classical photodetector, this criteria is a threshold in the photocurrent (Fig. 5.1(c)) and for the homodyne measurement, the criteria is a range of outputs in the pump homodyne. In Fig. 5.1(d,e), we show numerically how the single-photon detection efficiency and dark count rate are affected by the thresholding criteria for these two schemes.

The performance of the photodetector OPAD is limited by how well the system can distinguish between vacuum and a single photon, which is not perfect due to the Gaussian noise erasing the parity information of these states. However, a squeezed single photon has more probability distributed at high photon numbers, and hence photocurrent, than squeezed vacuum does. Therefore, setting the threshold involves a trade-off between two sought-after qualities in a single photon detector: low dark counts, which occur when measuring the amplified vacuum results in a photocurrent above the threshold and causes a click; and high photon detection efficiency, which

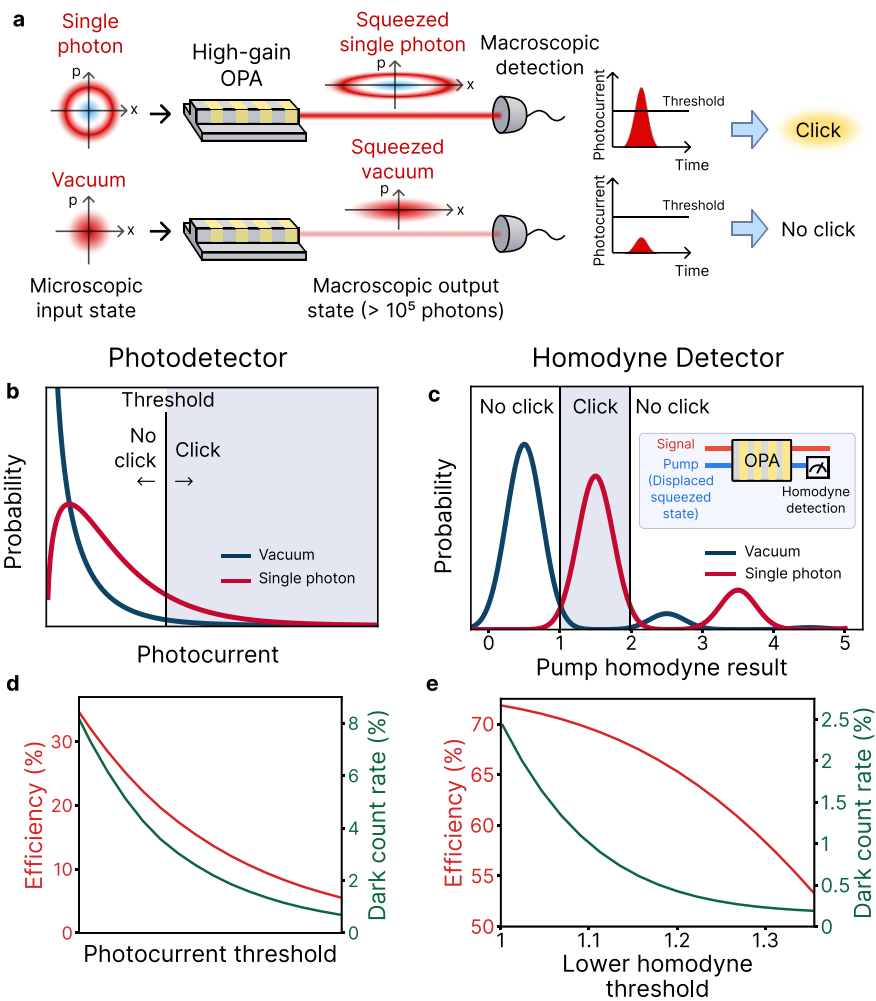


Figure 5.1: Detecting single photons with an OPA and a macroscopic detector. (a) The concept of the single photon OPAD. A microscopic quantum state is amplified in a waveguide OPA to levels detectable by a macroscopic detector. A threshold is applied to the detected pulse to categorize the signal as single photon or vacuum. (b) Photocurrent distribution from a photodetector when the input to the OPA is vacuum (dark blue) or a single photon (red). An example click threshold is shown. (c) Pump homodyne result distribution of vacuum (dark blue) and a single photon (red) as a function of the homodyne measurement result of the pump's squeezed quadrature. Inset: schematic of the homodyne detection scheme. (d) Efficiency and dark count rate as a function of photocurrent threshold. The specific threshold is dependent on the OPA gain and photodetector, and thus is left unlabeled. (e) Efficiency and dark count rate as a function of lower homodyne result threshold, with an upper threshold of 2.

is the probability that measuring a squeezed single photon results in a click. This trade-off can be seen in Fig. 5.1(d), with both the efficiency and dark count rate falling as the threshold increases.

Using a homodyne detector on the pump after the OPA, akin to the quantum non-demolition (QND) scheme from [39] (shown in the inset of Fig. 5.1(c)), can substantially enhance the OPAD's performance. With larger g/κ (the ratio of the coupling between the fundamental and second harmonic to the single-photon loss) and fewer modes [36] than exist in current OPAs, one could operate an OPAD in the pump-depletion regime in which the pump and signal become entangled, and non-Gaussian and Wigner negative features begin to emerge. In this regime, it is possible to project the signal state onto a squeezed Fock state through homodyne conditioning on the depleted pump, which is initially a displaced squeezed state. We simulated this OPAD scheme with the parameters from [39] (normalized interaction time $gt = 1$, pump squeezing of 3 dB, and single-mode OPA squeezing of 3.88 dB), finding a 69.2% efficiency and 0.9% dark count rate for certain click categorization limits on the homodyne measurement, corresponding to the shaded region between vertical lines in Fig. 5.1(c). The purity of the state resulting from a click is 0.89. Such an OPAD implements a non-Gaussian detection and could be used to create universal CV QIP resource states. The g/κ needed to realize this detection is proportional to the pump squeezing, which in this case corresponds to a requirement of $g/\kappa \gtrsim 1/4$ (see section 5.7 for more details).

Using quantum detector tomography [38, 40, 41], we characterized an OPAD made up of an integrated TFLN waveguide OPA (2.4-mm long) and an InGaAs photodetector, as shown in Fig. 5.2(a). The waveguide is dispersion-engineered for minimal group velocity mismatch between the signal and the pump, and for minimal group velocity dispersion at the signal's and pump's frequencies [32], enabling the distortion-free propagation of ultrafast pulses. To perform detector tomography, we send coherent states at $2.09 \mu\text{m}$ of different amplitudes and phases into the OPA. The coherent states are generated by a free-space optical parametric oscillator (OPO).

Histograms of the amplified and de-amplified coherent state photocurrents can be seen in Figure 5.2(c). Amplified pulses are measured at a pump phase of $\theta = 0$ while de-amplified pulses are measured at a pump phase of $\theta = \frac{\pi}{2}$. The amplified pulses have a higher average photocurrent and variance than amplified vacuum, and the de-amplified pulses have a similar distribution to amplified vacuum, as expected. The cause of the double-bumped distribution of $|\alpha| = 2.13$ in Figure 5.2(c) is likely

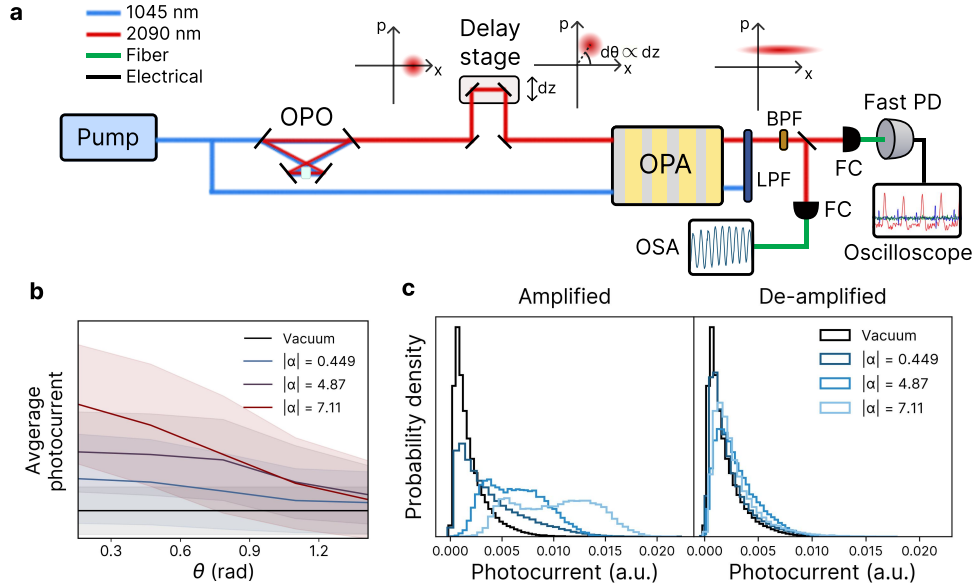


Figure 5.2: Experimental quantum tomography of an OPA-based detector. (a) Experimental setup for quantum tomography, including Wigner functions of the generated coherent and coherent squeezed states (not to scale). BPF: band-pass filter; LPF: low-pass filter; PD: photodetector; FC: fiber coupler; OSA: optical spectrum analyzer. (b) Average photocurrent of pulses as a function of coherent state angle. Shaded regions indicate the standard deviation of the pulses' photocurrent distribution. (c) Histogram of the pulse photocurrents for amplified and de-amplified coherent states and vacuum.

pump depletion, which leads to gain saturation and a bunching of the tail of higher photon number outcomes. The average photocurrent as a function of the coherent state angle θ , with the data binned into 5 angle bins between 0 and $\pi/2$, is plotted in Figure 5.2(b). The shaded regions indicate the standard deviation of the data. As θ approaches $\pi/2$, the average and standard deviation approaches that of a squeezed vacuum state, corresponding to the de-amplification of the coherent states.

To obtain the POVM of our OPAD, we used a convex optimization algorithm, similar to the one described in [38]. The experimentally retrieved and theoretical POVMs are shown in Figure 5.3 (a). The experimentally reconstructed POVM has a dark count probability of 2.2% and an efficiency of 26.2%, while the theoretical POVM has a dark count probability of 4.4% and an efficiency of 22.7%. The Wigner functions of the experimentally reconstructed POVM elements are shown in Fig. 5.3(b), with the click having negativity in the center.

The theoretical POVM was calculated for an OPA with a scaled-down gain (10 dB)

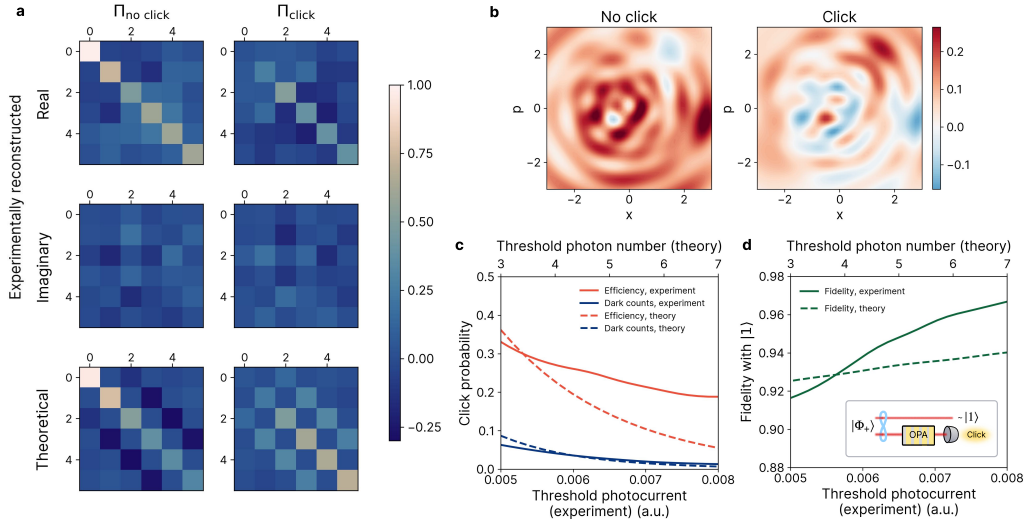


Figure 5.3: Detector tomography results and analysis. (a) The POVM elements of the OPAD, reconstructed through detector tomography (first and second rows) and theoretically calculated using QuTiP (third row). The theoretical POVM elements are real. (b) Experimentally reconstructed Wigner functions of the no click and click POVM elements. (c) The efficiency and dark count rate of the detector for both experimentally reconstructed and theoretically calculated POVMs as a function of the threshold photocurrent or photon number. (d) The fidelity with a single photon state after one mode of the Bell state $(|00\rangle + |11\rangle)/\sqrt{2}$ is measured with an OPAD vs. the threshold photocurrent or photon number, for both experimental and theoretical POVMs. Inset: diagram of the measurement scheme.

to be computationally viable, and with proportional noise. Since more squeezing does not change the POVM qualitatively, it is possible to recover the same POVMs from different amounts of gain by choosing appropriate thresholds (we elaborate on this procedure in later sections). We calculated the fidelity between the theoretical and experimental POVMs $F_n = \text{Tr}((\Pi_{n,\text{theo}}^{1/2} \Pi_{n,\text{exp}} \Pi_{n,\text{theo}}^{1/2})^{1/2})^2$ [38], with the trace of each of the POVM elements normalized to 1, for every combination of N_{th} in the theoretical POVM and photocurrent threshold in the experimental reconstruction. The average fidelity of both elements, $(F_{\text{click}} + F_{\text{no click}})/2$, was over 0.72 for thresholds chosen to optimize this metric.

To quantify the trade-off between efficiency and dark counts, we sweep the cutoff photocurrent in our convex optimization algorithm as well as N_{th} in the theoretical POVM calculation. The efficiencies and dark counts vs. the threshold photon number (for theory) and threshold photocurrent (for experiment) both for the experimental and theoretical POVMs are plotted in Figure 5.3(c), with the threshold

photocurrent adjusted to match the threshold photon number proportionally to the gains of the OPAs. The experimental POVM outperforming the theoretical POVM at higher thresholds is an indication that the pump depletion, which causes the later bump in the amplified photocurrent distribution, is improving the performance. This is because as the threshold photocurrent increases, especially above 0.006, the detection probability does not decrease as quickly as for a squeezed coherent state with no pump depletion.

We considered an example of DV detection in which one mode of a Bell state $|\Phi_+\rangle = (|00\rangle + |11\rangle)/\sqrt{2}$ is sent to the OPAD. We calculated the fidelity of the other mode with a single photon ($|1\rangle$) as a function of the detection efficiency using the theoretical and experimentally reconstructed POVMS. The results are plotted in Figure 5.3(d). As expected, the theoretical curve indicates a decrease in fidelity as the detection efficiency increases. This is due to the higher dark count probability at lower thresholds. The experimental POVM has a higher fidelity than the theoretical fidelity, which can be explained by the pump depletion.

The main benefits of the OPAD are its speed, room-temperature operation, integrability, and flexibility in wavelength. The speed of detection is limited only by the laser repetition rate, the photodetection system's electronic bandwidth, and the width of the pulses. We detected pulses with an 18 GHz detector, which is competitive with the timing resolutions of state-of-the-art SNSPDs and SPADs [42, 20]. Typically, the efficiency of SNSPDs and SPADs decreases as the wavelength increases due to bandgap-related limitations [43]. However, the OPAD can be designed to operate flexibly within the transparency window of LN spanning from the visible to the mid-IR. Furthermore, the simplicity of the design means that this detector can be readily integrated into the fast-evolving nonlinear nanophotonic circuits in LN. Additionally, our OPAD scheme is tolerant to losses after the OPA, as the loss affects all amplified states equally and can thus be accounted for by setting a lower threshold photocurrent.

The proposed OPAD can be used as an effective photon subtraction scheme for generation of non-Gaussian states with further improvements on the gain and material loss on nanophotonic platforms. We consider creating a Schrödinger kitten state through photon subtraction [11] a pump homodyne OPAD similar to the QND scheme and parameters in [39], as shown in Fig. 5.4(a) (see Methods for details). In this scheme, when the pump homodyne measurement is in a specific range, a click is triggered, projecting the initial squeezed vacuum onto a kitten state. The ensem-

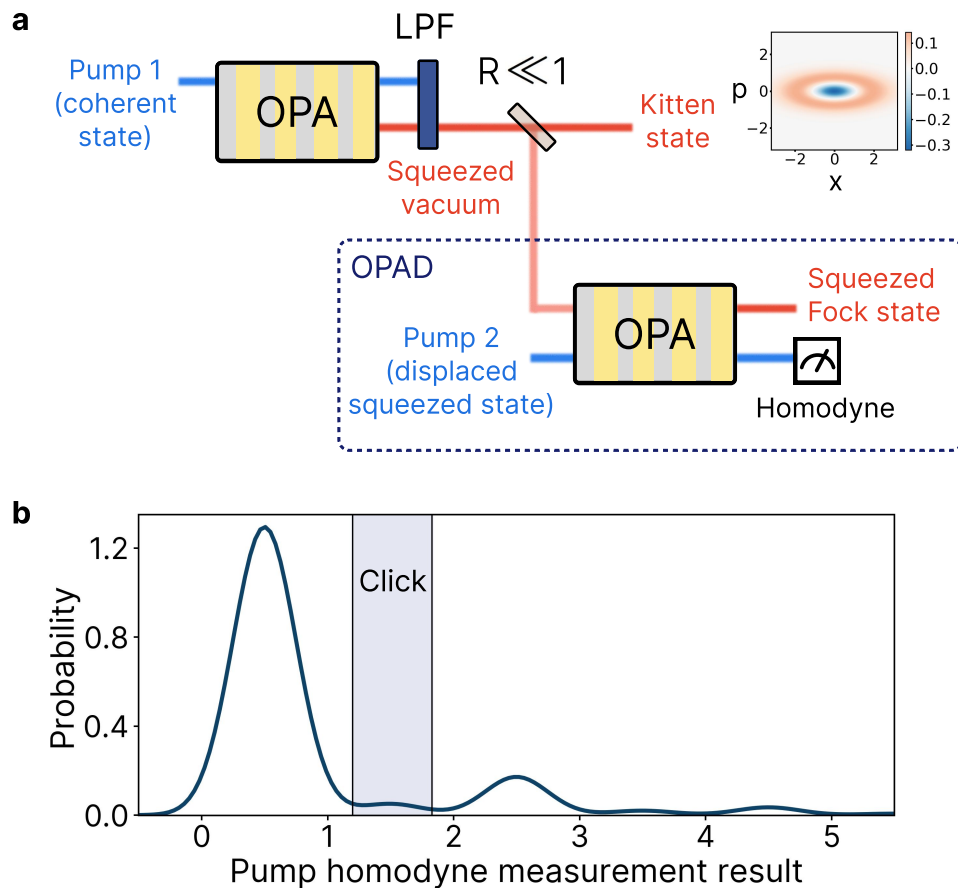


Figure 5.4: Using a pump homodyne OPAD to create a kitten state. (a) Diagram of the scheme. The first OPA creates squeezed vacuum and the second OPA is followed by a homodyne measurement on the depleted pump, triggering a click. The Wigner function of the kitten state is shown on the upper right. (b) The detection probability as a function of the pump homodyne measurement result, with the detection window considered to create the kitten state shaded.

ble average output state purity is numerically estimated to be 0.98 (shown in Fig. 5.4(b)), and the fidelity between the squeezed photon subtracted 2-mode squeezed state and a photon subtracted squeezed state is 0.96, with a click probability of 2.4%. Experimental realization of such kitten states requires further advancement in the losses in nanophotonic waveguides and the multimode effects that occur with broadband pulsed operation and dispersion engineering [44]. The propagation loss limits the g/κ of current realizations of OPAs to much less than one. Significant non-Gaussianity can be observed only when g/κ is around the order of unity.

5.2 Conclusion

We have proposed and demonstrated an OPAD on a TFLN nanophotonic chip suitable for detecting single photons. Our detector works at room temperature and pressure, and as the optical parametric amplification happens instantaneously, the speed of the detector is limited by the dispersion and pump pulse length, which determine the minimum duration of the output pulse at the signal wavelength. For our device, the GVM mismatch is less than 10 fs/mm, and so our speed is primarily constrained by the duration of the pump pulse to approximately 77 fs or a maximum repetition rate of 13 THz [44]. Through tailoring of the material, periodic poling, and dispersion engineering, it is possible to detect photons from visible wavelengths into the MIR. As an example of the OPAD's utility for DV QIP, we simulated a measurement using our experimental POVM on one mode of a Bell state and showed that for a detection efficiency of 30%, the fidelity of the other mode with a single photon is over 92%, showing how this system is useful for ultrafast DV state manipulations. We also showed numerically that it is possible to create a Schrödinger kitten state with a fidelity of 0.96 with an OPAD that uses homodyne detection on the pump. Our results suggest that single photon all-optical detection using second-order optical nonlinearity is a promising direction for ultrafast integrated photonic quantum information processing.

5.3 Methods

Experimental setup

We send coherent states of known amplitude and phase created by an OPO into the OPAD to gather data for POVM reconstruction. We pump both the OPO and the OPAD with 75-fs pulses at 1.045 μm at a 250 MHz repetition rate from a mode-locked laser. The coherent state amplitudes are set with a neutral density filter, and the phase is swept using a piezoelectric adjustable delay line. To reduce the

multi-mode effects in the amplified light and filter the pump out, we used a 48-nm bandwidth band-pass filter centered at 2.09 μm . In addition to this filter, we used one 1330-nm long-pass filter and two 1500 nm long-pass filters, which provided 150 dB of total pump rejection. Both the coherent states and the pump pulses were coupled onto the chip using a reflective objective and out-coupled with a tapered single-mode fiber.

Using a 90/10 beam-splitter, we record both the individual pulse photocurrent amplitudes and a slower time-averaged signal from an optical spectrum analyzer (OSA) containing the amplification and de-amplification envelope of the signal (amp/de-amp) as the phase is swept. The pulse data is recorded using an InGaAs photodetector with an 18 GHz bandwidth with an 80Gs/s 40GHz oscilloscope, enough to resolve individual optical pulses and hence measurement outcomes. The amp/de-amp envelope is used to determine the phase of the coherent state relative to the pump. We use data from roughly 4 million pulses as well as 140,000 pulses of optical parametric generation data in which the signal is the vacuum state to calibrate the shot noise.

In order to characterize the amplitude of the coherent states on-chip, we send the pulses into an SNSPD optimized for operation at 2 μm . Knowing the chip output loss from OPG measurements (see Supplemental Information) and the loss from the filters allowed us to calculate the amplitude from the fraction of pulses that caused a click on the SNSPD.

Quantum detector tomography

We calculate the theoretical click and no-click POVM matrices for a squeezer with 10 dB of squeezing. We used $\eta = \eta_{pd}\eta_f = 0.314$, for photodetector efficiency $\eta_{pd} = 0.629$ and filter loss $\eta_f = 0.5$. In order to determine the appropriate standard deviation σ for 10 dB of squeezing, we use the ratio of the standard deviation of the electronic noise to the average photocurrent for squeezed vacuum as a metric for the amount of noise. This metric was 0.172 for our setup and the average photon number for a 10 dB squeezed vacuum contains 2.02 photons, so for the theoretical POVM we used $\sigma = 2.02 \times 0.172 = 0.347$ photons. We sum over photon numbers up to 150 since at 10 dB the average photon number of squeezed vacuum is 2.02 and the probability amplitude at 150 photons is 10^{-7} .

To experimentally reconstruct the POVM of our OPAD, we use the convex optimization process described in [38] with the full POVM matrices rather than just the

diagonal entries as this is a phase-sensitive measurement. Because of this, we must solve a tensor equation rather than just a matrix one. We seek to invert the following equation:

$$P_{i,n} = F_{i,k,p} \Pi_{k,p,n} \quad (5.1)$$

where $P_{i,n} = \langle \alpha_i | \pi_n | \alpha_i \rangle$ is the experimentally determined probability of getting a click or not as a function of the coherent state amplitude α_i , and $F_{i,k,p} = e^{-|\alpha_i|^2} (\alpha_i^*)^k \alpha_i^p / \sqrt{k!p!}$ are the prefactors associated with the type of state being sent in (in our case, coherent states). $\Pi_{k,p,n} = \sum_{k,p} \theta^{(n)} |k\rangle \langle p|$ are the POVM matrices we are trying to find by performing a convex optimization which minimizes $\|P - F\Pi\|_2$. The indices k and p are the indices of the matrices, n refers to which measurement result ($n = 0$ for no click, $n = 1$ for a click), and i indexes the coherent state amplitude.

The optimization also involves a regularization constraint which smooths the diagonal entries of the POVM, which takes the form of:

$$R = \sum_{k,n} (\theta_{k+1,k+1}^{(n)} - \theta_{k,k}^{(n)})^2 \quad (5.2)$$

We can then perform the minimization over:

$$\min(\|P - F\Pi\|_2 + \gamma R) \quad (5.3)$$

for some regularization constant γ . Here we use $\gamma = 10^{-4}$, a relatively low value, in order to prevent over-smoothing of the POVM, as we expect some sharp characteristics from $|0\rangle \langle 0|$ to $|1\rangle \langle 1|$ indicating the click-like character of the detector (for more details see the Supplemental Information).

We use data from coherent states with amplitudes $|\alpha| = 0.449, 4.87, \text{ and } 7.11$ and binned the phases into five bins between 0 and $\pi/2$, as shown in Fig. 5.2(c), in order to discretize the data for the convex optimization. We found that varying the bin sizes did not create large variations in the output. We used CVXPY, a Python library for solving convex optimization problems, to invert Eqn. 5.1 [45].

Homodyne OPAD

We consider an OPAD with the homodyne measurement on the pump outlined in [39], which projects the signal onto a mixture of squeezed Fock states based on a homodyne measurement of a depleted pump. The parameters used in our simulations are the same as those considered in that paper. For an OPA Hamiltonian

in a displaced frame of $\hat{H} = g(\hat{a}^{\dagger 2}\hat{b} + \hat{a}^2\hat{b}^{\dagger}) + \delta\hat{a}^{\dagger}\hat{a} + \frac{r}{2}(\hat{a}^{\dagger 2} + \hat{a}^2)$, as for Figure 1 of that paper, we use $\sqrt{1 - r^2/\delta^2} = 150$ and $\tilde{g}/g = \sinh(\tanh^{-1}(r/\delta)) = 1$, which leads to the Fock states post-measurement having 3.88 dB of squeezing. We also set the total interaction time $gt = 1$. For the purity calculations, we consider a pump with 3 dB squeezing.

When we consider creating a Schrödinger kitten state using squeezed photon subtraction from squeezed vacuum using this scheme, we simulate a 5 dB squeezed vacuum going through a beam-splitter with reflectivity 0.2, with the OPAD on the reflected port. For our parameters, the measurement is effectively a squeezed Fock state subtraction, with the number of photons dependent on the pump homodyne detection result. We set the limits of the detected range of pump homodyne measurements which trigger a click such that the ensemble average output state purity is 0.98 and the average fidelity between this squeezed-photon-subtracted two-mode squeezed state and a photon-subtracted squeezed state is over 0.96. The probability of getting a detection result in the desired range is 2.4%.

5.4 Data availability

The data used to generate the plots and results in this thesis are available from the author upon reasonable request.

5.5 Code availability

The code used to analyze the data and generate the plots for this thesis chapter is available from the author upon reasonable request.

5.6 OPAD POVM

The POVM of an OPA followed by a photodetector with imperfect efficiency and Gaussian electronic noise, given by [46], is:

$$\Pi_n = \sum_{m \geq 0} P(n|m) \hat{S}^{\dagger}(\xi) |m\rangle \langle m| \hat{S}(\xi) \quad (5.4)$$

where $P(n|m)$ is the probability that the photodetector will register n photons when m photons arrive at the detector. We assume that the OPA is operating at degeneracy in the low pump-depletion, linear gain regime, so that it implements the single-mode squeezing operator $\hat{S}(\xi)$, for squeezing parameter ξ . Because the squeezing operator is phase-sensitive, this is a phase-sensitive detector. $P(n|m)$

depends on the photodetector's efficiency η and sources of Gaussian noise as

$$P(n|m) = \sum_{q \geq 0} P_{\sigma}(n|q)P_{\eta}(q|m) \quad (5.5)$$

where

$$P_{\sigma}(n|q) = \exp\left(\frac{-(n-q)^2}{2\sigma^2}\right) \quad (5.6)$$

is the probability of detecting n photons given q photons arrived at the detector. There is Gaussian noise with standard deviation σ , representing the electronic noise.

The term

$$P_{\eta}(q|m) = \frac{m!}{q!(m-q)!} \eta^q (1-\eta)^{m-q} \quad (5.7)$$

is the probability that q photons are detected after m photons pass through a beam-splitter with transmission η , which models the finite efficiency $\eta \leq 1$ of the photodetector.

We can model a click detector by setting a threshold number of photons N_{th} above which the detector registers a click. Then, the click POVM is

$$\Pi_{\text{click}} = \sum_{n \geq N_{th}} \Pi_n \quad (5.8)$$

and $\Pi_{\text{no click}} = \mathbf{1} - \Pi_{\text{click}}$. The probability of getting result k is $p_k = \text{Tr}(\rho \Pi_k)$, so the single photon efficiency is the (1,1) matrix element of Π_{click} in the Fock basis, and the dark count rate is the (0,0) element of the same matrix. All the summations are all over all photon numbers, but for computational purposes it suffices to sum over photon numbers within the range where there is significant probability density based on the squeezing parameter and noise standard deviation.

5.7 Chip dimensions and characterization

We use a thin-film lithium niobate (TFLN) chip with a thickness of 700 nm, waveguide etch depth of 345 nm and width of 1.85 μm . The poling period is 5.22 μm . We estimate that the group velocity mismatch between the fundamental and second harmonic is 5.2 fs/mm, and the group velocity dispersion at the fundamental is 120.1 fs^2/mm and at the second harmonic it is 28.4 fs^2/mm .

We characterize the chip's gain and output coupling by measuring the optical parametric generation (OPG) power as a function of pump power. We do so by blocking the signal path from the OPO and adjusting the pump power using a half-wave plate

and polarizing beam-splitter. The data we collected is shown in Fig. 5.5. The equation we fit to is

$$P_{OPG,off} = \hbar\omega_s\eta_{OC}f_{rep} \sinh^2(L\sqrt{\eta_{NL}\eta_{IC}P_{pump,off}}) \quad (5.9)$$

$$\approx \frac{\hbar\omega_s\eta_{OC}f_{rep}}{4} e^{2L\sqrt{\eta_{NL}\eta_{IC}P_{pump,off}}} \quad (5.10)$$

where the last approximation is in the large-gain regime. $P_{OPG,off}$ is the OPG power off-chip, $P_{pump,off}$ is the pump power off-chip, η_{OC} is the output coupling efficiency of the chip, η_{IC} is the input coupling efficiency, ω_s is the signal frequency, f_{rep} is the laser repetition rate, L is the length of the OPA, and η_{NL} is the normalized second harmonic efficiency. We fit to a linearized version of the equation, $\ln(P_{OPG,off}) = \ln(\hbar\omega_s\eta_{OC}f_{rep}/4) + 2b\sqrt{P_{pump,off}}$. We find $\eta_{OC} = 0.102$ and $b = L\sqrt{\eta_{NL}\eta_{IC}} = 16.3$ with standard deviations of the fit $\sigma_{\eta_{OC}} = 0.027$ and $\sigma_b = 0.328$. Thus, the output coupling loss is 9.9 dB. The transmission loss through the chip is 25 dB, which leads to an input coupling loss of approximately 15.1 dB. This is likely due to the mode mismatch between the output of the reflective objective and the waveguide. We find $\eta_{NL} = (1.46 \pm 0.06) \times 10^5 \text{ W}^{-1}\text{cm}^{-2}$.

Extracting g/κ from OPG measurements

The interaction Hamiltonian for 3-wave mixing is

$$\frac{\hat{H}}{\hbar} = g(\hat{a}^{\dagger 2}\hat{b} + \hat{a}^2\hat{b}^{\dagger}) \quad (5.11)$$

for interaction strength g , signal annihilation operator \hat{a} , and pump annihilation operator \hat{b} . In the Heisenberg picture under the undepleted-pump assumption with pump strength $\hat{b} \rightarrow \beta$, for an initial state of vacuum, the signal number operator evolves as $\langle \hat{a}^{\dagger}\hat{a} \rangle(t) = \langle \hat{N}_a \rangle(t) = \sinh^2(2g|\beta|t)$. To compare this to the OPG equation (Eqn. 5.9), we consider how to convert these quantities into the power measurements. $\langle \hat{N}_a \rangle(t) = P_{OPG,on}/(\hbar\omega_s f_{rep})$ and $|\beta| = \sqrt{\langle \hat{N}_b \rangle} = \sqrt{P_{pump,on}/(\hbar\omega_p f_{rep})}$ where the "on" subscript refers to the on-chip power. Substituting, we have:

$$P_{OPG,off} \approx \frac{\hbar\omega_s f_{rep} \eta_{OC}}{4} e^{4gt\sqrt{\eta_{IC}P_{pump,off}/(\hbar\omega_p f_{rep})}} \quad (5.12)$$

Comparing to Eqn. 5.9, we can see:

$$4gt\sqrt{\eta_{IC}P_{pump,off}/(\hbar\omega_p f_{rep})} = 2L\sqrt{\eta_{NL}\eta_{IC}P_{pump,off}} \quad (5.13)$$

so we have:

$$g = L\sqrt{\eta_{NL}\hbar\omega_p f_{rep}}/(2t) \quad (5.14)$$

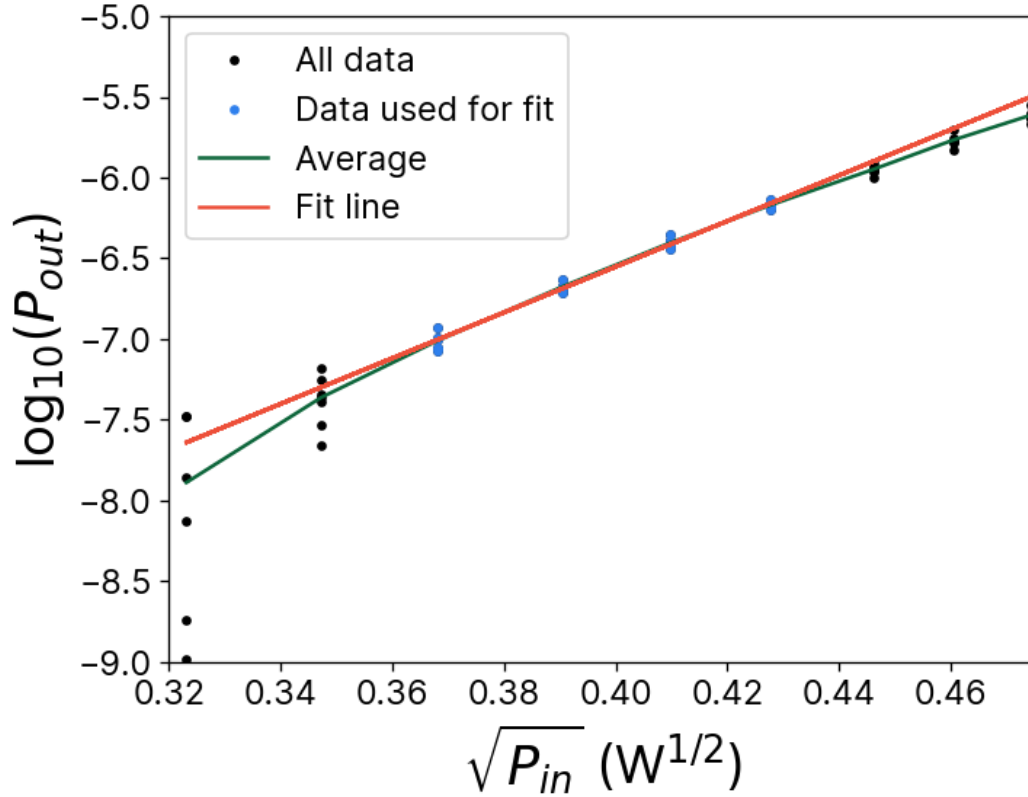


Figure 5.5: OPG power as a function of pump power. We use a subset of the data which is in the undepleted pump regime and also has a high enough power to clear the electronic noise floor of the detector, shown in blue. The average power is shown as the green line for illustration purposes. The fit equation with the parameters we found is shown in red.

and with $t = Ln/c$, finally:

$$g = \frac{c}{2n} \sqrt{\eta_{NL} \hbar \omega_p f_{rep}} \quad (5.15)$$

From the value of η_{NL} from the fit, we have $g = 29$ MHz.

However, we must account for multimode effects in our OPA. The simplest way of dealing with it is to assume that each mode receives an equal amount of the gain. We calculate the purity ρ from the normalized joint spectral intensity by performing a singular value decomposition and adding the squares of the eigenvalues, and obtain the effective mode number $m_{eff} = 1/\rho \approx 12.6$. We can then calculate $g_{eff} = g/m_{eff} = 2.3$ MHz.

We compare this number to the theoretical value using this equation from [47],

modified to include the naive multimode effects:

$$g_{eff} = \frac{4d_{eff}}{m_{eff}\lambda^3} \sqrt{\frac{2\pi^3\hbar c^3}{n^3\epsilon_0\tilde{V}_{sh}}} \quad (5.16)$$

where d_{eff} is the effective quadratic nonlinear coefficient, which is $d_{33}/(2\pi)$, with $d_{33} = 20$ pm/V and \tilde{V}_{sh} is the effective mode volume divided by $(\lambda/n)^3$, with perfect mode overlap resulting in it being exactly the normalized mode volume. We use the size of the waveguide 400 nm by 1780 nm times the pulse width of $\tau_p = 100$ fs equating to $\tau_p c/n = 1.62$ μ m for $n = 1.85$. Assuming perfect overlap and plugging in the parameters for our waveguide and pulse width to get the volume, we get an estimate of $g = 9.0$ MHz. This value is of the same order to the experimental extraction, and the discrepancy may be attributed to the imperfect mode overlap between the first harmonic and second harmonic.

We estimate the loss in the waveguide of 0.23 dB/cm and a group velocity of $v_g = 1.33 \times 10^8$ m/s, which leads to a $\kappa = \alpha v_g$ [47] of 702 MHz. Thus, $g_{eff}/\kappa \approx 0.0033$.

5.8 High-gain OPA simulations

The OPA in our theoretical POVM calculations has 10 dB of squeezing. This is clearly below the gain that our actual on-chip OPA has, which is in the tens of dBs. However, we do not have to simulate the actual gain of the OPA because the nature of the POVM does not qualitatively change with higher gain. Squeezing stretches out the photon number distributions but does not change their characteristics beyond 5 dB of squeezing.

To test whether the gain affected the efficiency-dark count trade-off, we simulate OPADs with gains between 7 and 12 dB, adjusted the Gaussian noise's standard deviation to be proportional to the average photon number of vacuum squeezed by that parameter, and swept the threshold photon number. The gain does not affect the efficiency-dark count rate curve, as can be seen in Fig. 5.6(a). The difference between the different gains is that for a the same threshold, the OPAD will be on different places on this curve. However, by adjusting the threshold it is possible to achieve the same performance as any other OPAD with different gain.

As another example, we calculate the click probability for input states of a single photon and a coherent state with $\langle N \rangle = |\alpha|^2 = 1$ for a threshold which yields a 2.5% dark count rate (a.k.a. vacuum click probability). As can be seen in Fig. 5.6(b), the rates stay constant over squeezing from 10 to 45 dB, indicating that an OPAD's performance is not based on the OPA's gain, and that as long as the classical

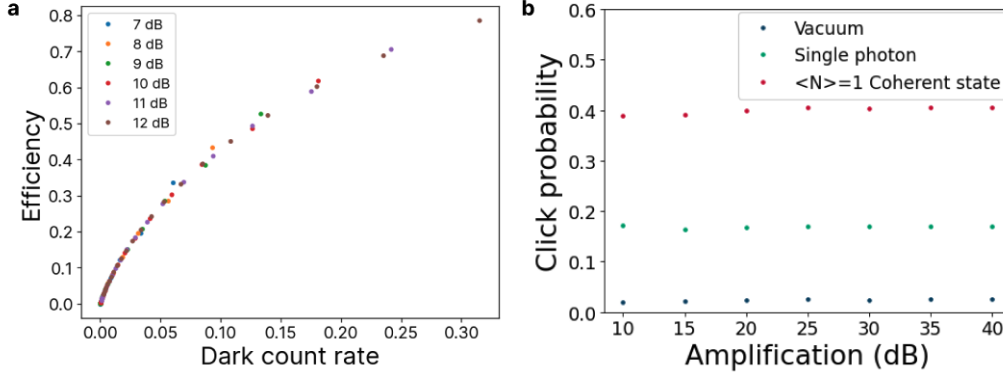


Figure 5.6: The performance of OPAs with different levels of gain. (a) The efficiency vs. dark count rate of OPADs with OPAs with various levels of gain with Gaussian noise proportional to the gain. The points were generated by sweeping the threshold photon number. (b) Click probability vs. OPA gain for vacuum, single photon, and an $\langle N \rangle = 1$ coherent state, for vacuum click probability (dark count rate) of 2.5%. Note the constant click probabilities over a wide amplification range.

detector is sensitive enough to detect the pulses, an appropriate threshold can be set to achieve any performance along the dark count rate-efficiency curve.

Thus, we conclude that it is possible to gain insight from a simulation of an OPAD with 10 dB of gain despite it being much less than the actual gain.

5.9 Detector tomography regularization constant

To invert the matrix equation to extract the POVM, we perform convex optimization to minimize this equation:

$$\min(\|P - F\Pi\|_2 + \gamma R) \quad (5.17)$$

with γR being the regularization to smooth the potentially spiky nature of the diagonal entries of the POVM, with $R = \sum_{k,n} (\theta_{k+1,k+1}^{(n)} - \theta_{k,k}^{(n)})^2$. To ensure we use a value of γ not too high such that it introduces artifacts, we swept γ and found the dark count rate and efficiency as a function of γ (Fig. 5.7). We find that 10^{-4} was within the region such that changing it did not change the result significantly, so we chose that value.

5.10 Acknowledgments

Device nanofabrication was performed at the Kavli Nanoscience Institute (KNI) at Caltech. The authors gratefully acknowledge support from ARO grant no. W911NF-

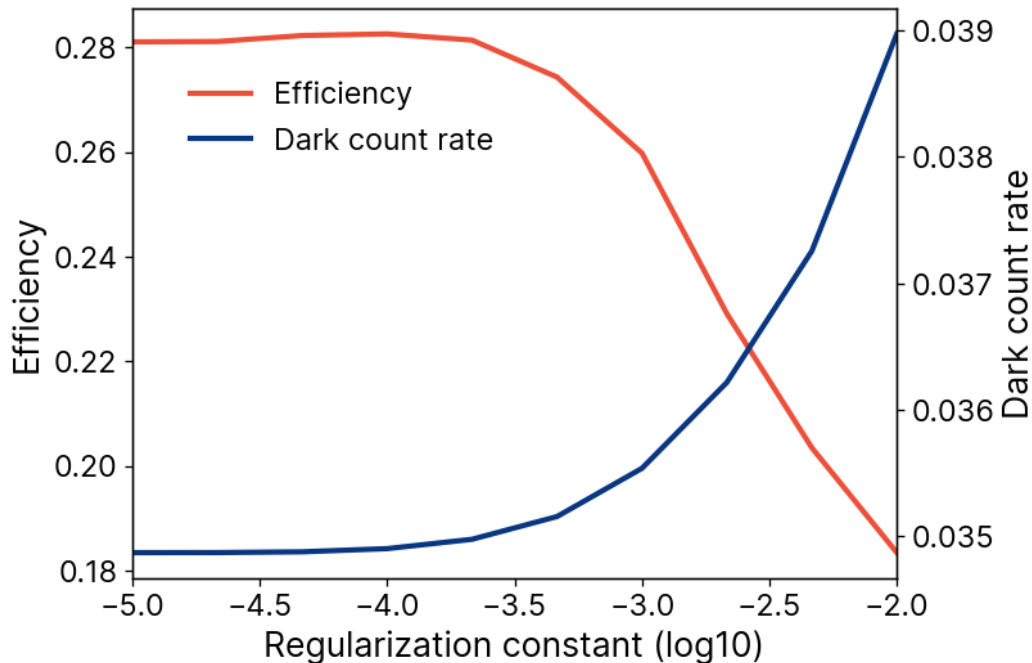


Figure 5.7: A plot of dark count rate and efficiency as a function of the regularization constant γ .

23-1-0048, NSF grant no. 1846273, 1918549, 2139433, AFOSR award FA9550-23-1-0755, DARPA award D23AP00158, the center for sensing to intelligence at Caltech, the Alfred P. Sloan Foundation, and NASA/JPL. The authors wish to thank NTT Research for their financial support. RN would like to thank Dr. Saman Jahani for fruitful discussions. ES would like to thank Edwin Ng and Ryotatsu Yanagimoto for advice on g/κ calculations.

5.11 Author information

These authors contributed equally: Elina Sendonaris and James Williams.

Contributions

E.S., J.W., R.N., and A.M. conceived the idea and designed the experiments. E.S. and J.W. carried out the experiments with help from R.G.. E.S. carried out the numerical simulations with help from L.L., J.W., and R.N. R.S. fabricated the device. E.S. wrote the manuscript with input from all authors. A.M. supervised the project.

5.12 Ethics declarations

Competing interests

A.M., R. N., L.L., and R.S. are inventors on the U.S. patent application (application number 18/155,444). R.S., L.L., and A.M. are involved in developing photonic integrated nonlinear circuits at PINC Technologies Inc. R.S., L.L., and A.M. have an equity interest in PINC Technologies Inc.

References

- [1] Robert Raussendorf and Hans J. Briegel. “A One-Way Quantum Computer”. In: *Phys. Rev. Lett.* 86.22 (May 28, 2001), pp. 5188–5191. ISSN: 0031-9007, 1079-7114. DOI: 10.1103/PhysRevLett.86.5188. URL: <https://link.aps.org/doi/10.1103/PhysRevLett.86.5188> (visited on 07/06/2023).
- [2] Mikkel V. Larsen, Xueshi Guo, Casper R. Breum, Jonas S. Neergaard-Nielsen, and Ulrik L. Andersen. “Deterministic multi-mode gates on a scalable photonic quantum computing platform”. In: *Nat. Phys.* 17.9 (Sept. 2021). Number: 9 Publisher: Nature Publishing Group, pp. 1018–1023. ISSN: 1745-2481. DOI: 10.1038/s41567-021-01296-y. URL: <https://www.nature.com/articles/s41567-021-01296-y> (visited on 07/06/2023).
- [3] Sara Bartolucci, Patrick Birchall, Hector Bombin, Hugo Cable, Chris Dawson, Mercedes Gimeno-Segovia, Eric Johnston, Konrad Kieling, Naomi Nickerson, Mihir Pant, Fernando Pastawski, Terry Rudolph, and Chris Sparrow. *Fusion-based quantum computation*. Jan. 22, 2021. arXiv: 2101.09310 [quant-ph]. URL: <http://arxiv.org/abs/2101.09310> (visited on 07/05/2023).
- [4] Emanuel Knill, Raymond Laflamme, and Gerard Milburn. “A scheme for efficient quantum computation with linear optics”. In: 409 (2001).
- [5] Nicolas C. Menicucci. “Temporal-mode continuous-variable cluster states using linear optics”. In: *Phys. Rev. A* 83.6 (June 13, 2011), p. 062314. ISSN: 1050-2947, 1094-1622. DOI: 10.1103/PhysRevA.83.062314. URL: <https://link.aps.org/doi/10.1103/PhysRevA.83.062314> (visited on 07/06/2023).
- [6] Nicolas C. Menicucci, Peter Van Loock, Mile Gu, Christian Weedbrook, Timothy C. Ralph, and Michael A. Nielsen. “Universal Quantum Computation with Continuous-Variable Cluster States”. In: *Phys. Rev. Lett.* 97.11 (Sept. 13, 2006), p. 110501. ISSN: 0031-9007, 1079-7114. DOI: 10.1103/PhysRevLett.97.110501. URL: <https://link.aps.org/doi/10.1103/PhysRevLett.97.110501> (visited on 07/06/2023).
- [7] Usman A. Javid, Raymond Lopez-Rios, Jingwei Ling, Austin Graf, Jeremy Staffa, and Qiang Lin. “Chip-scale simulations in a quantum-correlated synthetic space”. In: *Nat. Photon.* (June 22, 2023). Publisher: Nature Publishing Group, pp. 1–8. ISSN: 1749-4893. DOI: 10.1038/s41566-023-01236-7.

- URL: <https://www.nature.com/articles/s41566-023-01236-7> (visited on 08/01/2023).
- [8] Jeremy L O’Brien. “Optical quantum computing”. In: *Science* 318.5856 (2007), pp. 1567–1570.
- [9] Seth Lloyd and Samuel L Braunstein. “Quantum computation over continuous variables”. In: *Physical Review Letters* 82.8 (1999), p. 1784.
- [10] Ben Q. Baragiola, Giacomo Pantaleoni, Rafael N. Alexander, Angela Karanjai, and Nicolas C. Menicucci. “All-Gaussian Universality and Fault Tolerance with the Gottesman-Kitaev-Preskill Code”. In: *Phys. Rev. Lett.* 123.20 (Nov. 13, 2019), p. 200502. ISSN: 0031-9007, 1079-7114. DOI: 10.1103/PhysRevLett.123.200502. URL: <https://link.aps.org/doi/10.1103/PhysRevLett.123.200502> (visited on 07/07/2023).
- [11] Alexei Ourjoumtsev, Rosa Tualle-Brouri, Julien Laurat, and Philippe Grangier. “Generating optical Schrodinger kittens for quantum information processing”. In: *Science* 312.5770 (2006), pp. 83–86.
- [12] Daniel Gottesman, Alexei Kitaev, and John Preskill. “Encoding a qubit in an oscillator”. In: *Physical Review A* 64.1 (2001), p. 012310.
- [13] Shunya Konno, Warit Asavanant, Fumiya Hanamura, Hironari Nagayoshi, Kosuke Fukui, Atsushi Sakaguchi, Ryuhoh Ide, Fumihiro China, Masahiro Yabuno, Shigehito Miki, et al. “Logical states for fault-tolerant quantum computation with propagating light”. In: *Science* 383.6680 (2024), pp. 289–293.
- [14] Robert H. Hadfield. “Single-photon detectors for optical quantum information applications”. In: *Nature Photon* 3.12 (Dec. 2009), pp. 696–705. ISSN: 1749-4885, 1749-4893. DOI: 10.1038/nphoton.2009.230. URL: <https://www.nature.com/articles/nphoton.2009.230> (visited on 06/27/2023).
- [15] Iman Esmail Zadeh, J. Chang, Johannes W. N. Los, Samuel Gyger, Ali W. Elshaari, Stephan Steinhauer, Sander N. Dorenbos, and Val Zwiller. “Superconducting nanowire single-photon detectors: A perspective on evolution, state-of-the-art, future developments, and applications”. In: *Appl. Phys. Lett.* 118.19 (May 10, 2021), p. 190502. ISSN: 0003-6951, 1077-3118. DOI: 10.1063/5.0045990. URL: <https://pubs.aip.org/aip/apl/article/1062620> (visited on 06/27/2023).
- [16] Adriana E Lita, Aaron J Miller, and Sae Woo Nam. “Counting near-infrared single-photons with 95% efficiency”. In: *Optics express* 16.5 (2008), pp. 3032–3040.
- [17] Francesco Ceccarelli, Giulia Acconcia, Angelo Gulinatti, Massimo Ghioni, Ivan Rech, and Roberto Osellame. “Recent Advances and Future Perspectives of Single-Photon Avalanche Diodes for Quantum Photonics Applications”. In: *Advanced Quantum Technologies* 4.2 (2021). _eprint: <https://onlinelibrary.wiley.com/doi/pdf/10.1002>

- p. 2000102. ISSN: 2511-9044. DOI: 10.1002/qute.202000102. URL: <https://onlinelibrary.wiley.com/doi/abs/10.1002/qute.202000102> (visited on 06/27/2023).
- [18] Dileep V. Reddy, Robert R. Nerem, Sae Woo Nam, Richard P. Mirin, and Varun B. Verma. “Superconducting nanowire single-photon detectors with 98% system detection efficiency at 1550 nm”. In: *Optica* 7.12 (Dec. 20, 2020), p. 1649. ISSN: 2334-2536. DOI: 10.1364/OPTICA.400751. URL: <https://opg.optica.org/abstract.cfm?URI=optica-7-12-1649> (visited on 08/01/2023).
- [19] Francesco Marsili, Varun B Verma, Jeffrey A Stern, Susanmarie Harrington, Adriana E Lita, Thomas Gerrits, Igor Vayshenker, Burm Baek, Matthew D Shaw, Richard P Mirin, et al. “Detecting single infrared photons with 93% system efficiency”. In: *Nature Photonics* 7.3 (2013), pp. 210–214.
- [20] Giovanni V. Resta, Lorenzo Stasi, Matthieu Perrenoud, Sylvain El-Khoury, Tiff Brydges, Rob Thew, Hugo Zbinden, and Félix Bussi eres. “GHz detection rates and dynamic photon-number resolution with superconducting nanowire arrays”. In: *Nano Lett.* 23.13 (July 12, 2023), pp. 6018–6026. ISSN: 1530-6984, 1530-6992. DOI: 10.1021/acs.nanolett.3c01228. arXiv: 2303.17401[physics, physics:quant-ph]. URL: <http://arxiv.org/abs/2303.17401> (visited on 08/03/2023).
- [21] Fadri Gr unenfelder, Alberto Boaron, Giovanni V. Resta, Matthieu Perrenoud, Davide Rusca, Claudio Barreiro, Rapha el Houlmann, Rebecka Sax, Lorenzo Stasi, Sylvain El-Khoury, Esther H anggi, Nico Bosshard, F elix Bussi eres, and Hugo Zbinden. “Fast single-photon detectors and real-time key distillation enable high secret-key-rate quantum key distribution systems”. In: *Nat. Photon.* 17.5 (May 2023), pp. 422–426. ISSN: 1749-4885, 1749-4893. DOI: 10.1038/s41566-023-01168-2. URL: <https://www.nature.com/articles/s41566-023-01168-2> (visited on 07/05/2023).
- [22] Hiroyuki Shibata, Kaoru Shimizu, Hiroki Takesue, and Yasuhiro Tokura. “Ultimate low system dark-count rate for superconducting nanowire single-photon detector”. In: *Opt. Lett., OL* 40.14 (July 15, 2015). Publisher: Optica Publishing Group, pp. 3428–3431. ISSN: 1539-4794. DOI: 10.1364/OL.40.003428. URL: <https://opg.optica.org/ol/abstract.cfm?uri=ol-40-14-3428> (visited on 08/01/2023).
- [23] Boris Korzh, Qing-Yuan Zhao, Jason P. Allmaras, Simone Frasca, Travis M. Autry, Eric A. Bersin, Andrew D. Beyer, Ryan M. Briggs, Bruce Bumble, Marco Colangelo, Garrison M. Crouch, Andrew E. Dane, Thomas Gerrits, Adriana E. Lita, Francesco Marsili, Galan Moody, Cristi an Pe a, Edward Ramirez, Jake D. Rezac, Neil Sinclair, Martin J. Stevens, Angel E. Velasco, Varun B. Verma, Emma E. Wollman, Si Xie, Di Zhu, Paul D. Hale, Maria Spiropulu, Kevin L. Silverman, Richard P. Mirin, Sae Woo Nam, Alexander G. Kozorezov, Matthew D. Shaw, and Karl K. Berggren. “Demonstration of

- sub-3 ps temporal resolution with a superconducting nanowire single-photon detector”. In: *Nat. Photonics* 14.4 (Apr. 2020). Number: 4 Publisher: Nature Publishing Group, pp. 250–255. ISSN: 1749-4893. DOI: 10.1038/s41566-020-0589-x. URL: <https://www.nature.com/articles/s41566-020-0589-x> (visited on 08/01/2023).
- [24] Jascha A Lau, Varun B Verma, Dirk Schwarzer, and Alec M Wodtke. “Superconducting single-photon detectors in the mid-infrared for physical chemistry and spectroscopy”. In: *Chemical Society Reviews* 52.3 (2023), pp. 921–941.
- [25] Di Zhu, Linbo Shao, Mengjie Yu, Rebecca Cheng, Boris Desiatov, C. J. Xin, Yaowen Hu, Jeffrey Holzgrafe, Soumya Ghosh, Amirhassan Shams-Ansari, Eric Puma, Neil Sinclair, Christian Reimer, Mian Zhang, and Marko Lončar. “Integrated photonics on thin-film lithium niobate”. In: *Adv. Opt. Photon., AOP* 13.2 (June 30, 2021). Publisher: Optica Publishing Group, pp. 242–352. ISSN: 1943-8206. DOI: 10.1364/AOP.411024. URL: <https://opg.optica.org/aop/abstract.cfm?uri=aop-13-2-242> (visited on 08/01/2023).
- [26] S. Y. Siew, B. Li, F. Gao, H. Y. Zheng, W. Zhang, P. Guo, S. W. Xie, A. Song, B. Dong, L. W. Luo, C. Li, X. Luo, and G.-Q. Lo. “Review of Silicon Photonics Technology and Platform Development”. In: *Journal of Lightwave Technology* 39.13 (July 2021). Conference Name: Journal of Lightwave Technology, pp. 4374–4389. ISSN: 1558-2213. DOI: 10.1109/JLT.2021.3066203.
- [27] Jintian Lin, Fang Bo, Ya Cheng, and Jingjun Xu. “Advances in on-chip photonic devices based on lithium niobate on insulator”. In: *Photon. Res., PRJ* 8.12 (Dec. 1, 2020). Publisher: Optica Publishing Group, pp. 1910–1936. ISSN: 2327-9125. DOI: 10.1364/PRJ.395305. URL: <https://opg.optica.org/prj/abstract.cfm?uri=prj-8-12-1910> (visited on 08/04/2023).
- [28] Galan Moody, Volker J Sorger, Daniel J Blumenthal, Paul W Juodawlkis, William Loh, Cheryl Sorace-Agaskar, Alex E Jones, Krishna C Balram, Jonathan CF Matthews, Anthony Laing, et al. “2022 Roadmap on integrated quantum photonics”. In: *Journal of Physics: Photonics* 4.1 (2022), p. 012501.
- [29] Jianwei Wang, Fabio Sciarrino, Anthony Laing, and Mark G Thompson. “Integrated photonic quantum technologies”. In: *Nature Photonics* 14.5 (2020), pp. 273–284.
- [30] J. M. Arrazola, V. Bergholm, K. Brádler, T. R. Bromley, M. J. Collins, I. Dhand, A. Fumagalli, T. Gerrits, A. Goussev, L. G. Helt, J. Hundal, T. Isacsson, R. B. Israel, J. Izaac, S. Jahangiri, R. Janik, N. Killoran, S. P. Kumar, J. Lavoie, A. E. Lita, D. H. Mahler, M. Menotti, B. Morrison, S. W. Nam, L. Neuhaus, H. Y. Qi, N. Quesada, A. Repeatingon, K. K. Sabapathy, M. Schuld, D. Su, J. Swinerton, A. Száva, K. Tan, P. Tan, V. D. Vaidya, Z. Vernon, Z. Zabaneh, and Y. Zhang. “Quantum circuits with many photons on a programmable nanophotonic chip”. In: *Nature* 591.7848 (Mar. 2021).

- Number: 7848 Publisher: Nature Publishing Group, pp. 54–60. ISSN: 1476-4687. DOI: 10.1038/s41586-021-03202-1. URL: <https://www.nature.com/articles/s41586-021-03202-1> (visited on 07/06/2023).
- [31] Ayed Al Sayem, Risheng Cheng, Sihao Wang, and Hong X. Tang. “Lithium-niobate-on-insulator waveguide-integrated superconducting nanowire single-photon detectors”. In: *Applied Physics Letters* 116.15 (Apr. 13, 2020), p. 151102. ISSN: 0003-6951, 1077-3118. DOI: 10.1063/1.5142852. URL: <https://pubs.aip.org/apl/article/116/15/151102/38104/Lithium-niobate-on-insulator-waveguide-integrated> (visited on 07/06/2023).
- [32] Luis Ledezma, Ryoto Sekine, Qiushi Guo, Rajveer Nehra, Saman Jahani, and Alireza Marandi. “Intense optical parametric amplification in dispersion-engineered nanophotonic lithium niobate waveguides”. In: *Optica* 9.3 (Mar. 20, 2022), p. 303. ISSN: 2334-2536. DOI: 10.1364/OPTICA.442332. URL: <https://opg.optica.org/abstract.cfm?URI=optica-9-3-303> (visited on 06/27/2023).
- [33] Rajveer Nehra, Ryoto Sekine, Luis Ledezma, Qiushi Guo, Robert M. Gray, Arkadev Roy, and Alireza Marandi. “Few-cycle vacuum squeezing in nanophotonics”. In: *Science* 377.6612 (Sept. 16, 2022), pp. 1333–1337. ISSN: 0036-8075, 1095-9203. DOI: 10.1126/science.abo6213. URL: <https://www.science.org/doi/10.1126/science.abo6213> (visited on 06/27/2023).
- [34] **James Williams**, Rajveer Nehra, Elina Sendonaris, Luis Ledezma, Robert M Gray, Ryoto Sekine, and Alireza Marandi. “Ultrashort pulse biphoton source in lithium niobate nanophotonics at 2 μm ”. In: *Nanophotonics* 0 (2024).
- [35] Mahmoud Kalash and Maria V Chekhova. “Wigner function tomography via optical parametric amplification”. In: *Optica* 10.9 (2023), pp. 1142–1146.
- [36] Ryotatsu Yanagimoto, Edwin Ng, Marc Jankowski, Rajveer Nehra, Timothy P. McKenna, Tatsuhiro Onodera, Logan G. Wright, Ryan Hamerly, Alireza Marandi, M. M. Fejer, and Hideo Mabuchi. *Mesoscopic ultrafast nonlinear optics – The emergence of multimode quantum non-Gaussian physics*. Nov. 22, 2023. arXiv: 2311.13775[physics, physics:quant-ph]. URL: <http://arxiv.org/abs/2311.13775> (visited on 11/27/2023).
- [37] Yaakov Shaked, Yoad Michael, Rafi Z Vered, Leon Bello, Michael Rosenbluh, and Avi Pe’er. “Lifting the bandwidth limit of optical homodyne measurement with broadband parametric amplification”. In: *Nature communications* 9.1 (2018), p. 609.
- [38] A Feito, J S Lundeen, H Coldenstrodt-Ronge, J Eisert, M B Plenio, and I A Walmsley. “Measuring measurement: theory and practice”. In: *New J. Phys.* 11.9 (Sept. 28, 2009), p. 093038. ISSN: 1367-2630. DOI: 10.1088/1367-2630/11/9/093038. URL: <https://iopscience.iop.org/article/10.1088/1367-2630/11/9/093038> (visited on 06/27/2023).

- [39] Ryotatsu Yanagimoto, Rajveer Nehra, Ryan Hamerly, Edwin Ng, Alireza Marandi, and Hideo Mabuchi. “Quantum Nondemolition Measurements with Optical Parametric Amplifiers for Ultrafast Universal Quantum Information Processing”. In: *PRX Quantum* 4.1 (Mar. 29, 2023), p. 010333. ISSN: 2691-3399. DOI: [10.1103/PRXQuantum.4.010333](https://doi.org/10.1103/PRXQuantum.4.010333). URL: <https://link.aps.org/doi/10.1103/PRXQuantum.4.010333> (visited on 09/22/2024).
- [40] J. S. Lundeen, A. Feito, H. Coldenstrodt-Ronge, K. L. Pregnell, Ch. Silberhorn, T. C. Ralph, J. Eisert, M. B. Plenio, and I. A. Walmsley. “Tomography of quantum detectors”. In: *Nature Phys* 5.1 (Jan. 2009), pp. 27–30. ISSN: 1745-2473, 1745-2481. DOI: [10.1038/nphys1133](https://doi.org/10.1038/nphys1133). URL: <https://www.nature.com/articles/nphys1133> (visited on 06/27/2023).
- [41] Rajveer Nehra, Kevin Valson Jacob, Miller Eaton, and Olivier Pfister. “Characterizing Quantum Detectors by Wigner Functions”. In: *OSA Quantum 2.0 Conference (2020), paper QTu8A.6*. Quantum 2.0. Optica Publishing Group, Sept. 14, 2020, QTu8A.6. DOI: [10.1364/QUANTUM.2020.QTu8A.6](https://doi.org/10.1364/QUANTUM.2020.QTu8A.6). URL: <https://opg.optica.org/abstract.cfm?uri=QUANTUM-2020-QTu8A.6> (visited on 11/21/2023).
- [42] Dekang Chen, Stephen D. March, Andrew H. Jones, Yang Shen, Adam A. Dadey, Keye Sun, J. Andrew McArthur, Alec M. Skipper, Xingjun Xue, Bingtian Guo, Junwu Bai, Seth R. Bank, and Joe C. Campbell. “Photon-trapping-enhanced avalanche photodiodes for mid-infrared applications”. In: *Nat. Photon.* 17.7 (July 2023). Number: 7 Publisher: Nature Publishing Group, pp. 594–600. ISSN: 1749-4893. DOI: [10.1038/s41566-023-01208-x](https://doi.org/10.1038/s41566-023-01208-x). URL: <https://www.nature.com/articles/s41566-023-01208-x> (visited on 07/06/2023).
- [43] Stefano Dello Russo, Arianna Elefante, Daniele Dequal, Deborah Katia Pallotti, Luigi Santamaria Amato, Fabrizio Sgobba, and Mario Siciliani de Cumis. “Advances in Mid-Infrared Single-Photon Detection”. In: *Photonics* 9.7 (July 2022). Number: 7 Publisher: Multidisciplinary Digital Publishing Institute, p. 470. ISSN: 2304-6732. DOI: [10.3390/photonics9070470](https://doi.org/10.3390/photonics9070470). URL: <https://www.mdpi.com/2304-6732/9/7/470> (visited on 08/04/2023).
- [44] Wojciech Wasilewski, A. I. Lvovsky, Konrad Banaszek, and Czesław Radzewicz. “Pulsed squeezed light: Simultaneous squeezing of multiple modes”. In: *Phys. Rev. A* 73.6 (June 20, 2006), p. 063819. ISSN: 1050-2947, 1094-1622. DOI: [10.1103/PhysRevA.73.063819](https://doi.org/10.1103/PhysRevA.73.063819). URL: <https://link.aps.org/doi/10.1103/PhysRevA.73.063819> (visited on 03/09/2024).
- [45] Steven Diamond and Stephen Boyd. “CVXPY: A Python-Embedded Modeling Language for Convex Optimization”. In: *Journal of Machine Learning Research* (2016). To appear. URL: https://stanford.edu/~boyd/papers/pdf/cvxpy_paper.pdf.

- [46] Alex O C Davis, Mattia Walschaers, Valentina Parigi, and Nicolas Treps. “Conditional preparation of non-Gaussian quantum optical states by mesoscopic measurement”. In: *New J. Phys.* 23.6 (June 1, 2021), p. 063039. ISSN: 1367-2630. DOI: 10.1088/1367-2630/ac0204. URL: <https://iopscience.iop.org/article/10.1088/1367-2630/ac0204> (visited on 07/06/2023).
- [47] Ryotatsu Yanagimoto, Edwin Ng, Marc Jankowski, Hideo Mabuchi, and Ryan Hamerly. “Temporal trapping: a route to strong coupling and deterministic optical quantum computation”. In: *Optica* 9.11 (2022), pp. 1289–1296.

*Chapter 6***ULTRAFAST ALL-OPTICAL MEASUREMENT OF SQUEEZED
VACUUM IN A LITHIUM NIOBATE NANOPHOTONIC
CIRCUIT**

James Williams, Elina Sendonaris, Rajveer Nehra, Robert M Gray, Ryoto Sekine, Luis Ledezma, and Alireza Marandi (2024) Ultrafast All-Optical Measurement of Squeezed Vacuum in a Lithium Niobate Nanophotonic Circuit arXiv preprint arXiv:2502.00518.

ABSTRACT

Squeezed vacuum, a fundamental resource for continuous-variable quantum information processing, has been used to demonstrate quantum advantages in sensing, communication, and computation. While most experiments use homodyne detection to characterize squeezing and are therefore limited to electronic bandwidths, recent experiments have shown optical parametric amplification (OPA) to be a viable measurement strategy. Here, we realize OPA-based quantum state tomography in integrated photonics and demonstrate the generation and all-optical Wigner tomography of squeezed vacuum in a nanophotonic circuit. We employ dispersion-engineering to enable the distortion-free propagation of femtosecond pulses and achieve ultrabroad operation bandwidths, effectively lifting the speed restrictions imposed by traditional electronics on quantum measurements with a theoretical maximum clock speed of 6.5 THz. We implement our circuit on thin-film lithium niobate, a platform compatible with a wide variety of active and passive photonic components. Our results chart a course for realizing all-optical ultrafast quantum information processing in an integrated room-temperature platform.

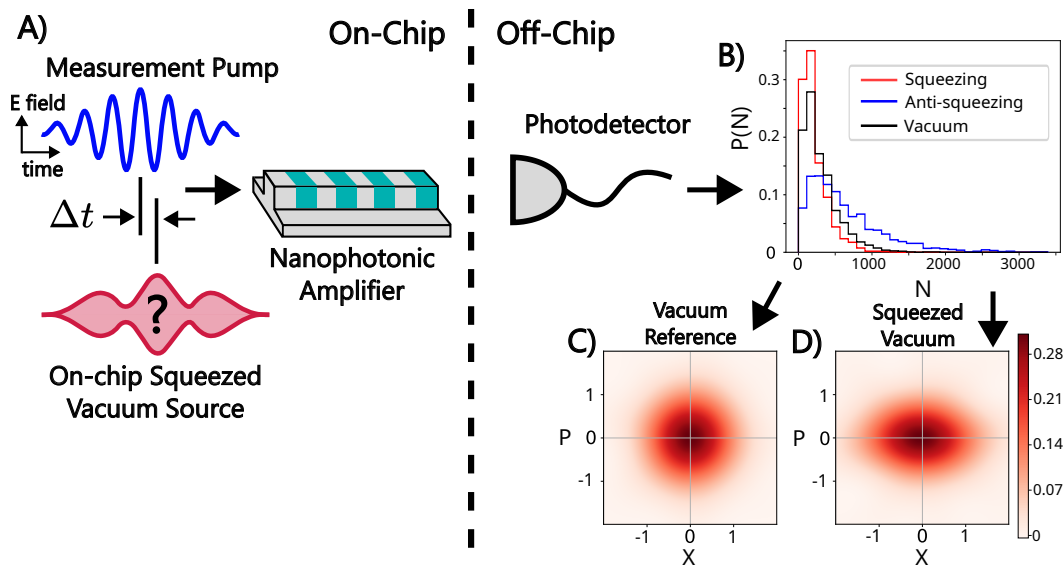


Figure 6.1: A) Layout of the measurement procedure. Δt represents the relative time-delay between the pump and squeezed vacuum generated on-chip where a 0.775 fs delay corresponds to a measurement phase of $\phi = \frac{\pi}{2}$. B) Measured photon number distributions for squeezing ($\phi = \frac{\pi}{2}$), anti-squeezing ($\phi = 0$) and vacuum. C) Wigner function recovered for vacuum. D) Wigner function recovered for squeezed vacuum.

6.1 Introduction

Many quantum systems have been used to gain an advantage over otherwise purely classical means in a variety of fields [1, 2, 3]. Photonics has emerged as a front-runner platform in quantum information processing (QIP) for several key reasons. Most photonic technologies are capable of operating at room temperature outside a carefully-controlled cryogenic environment. Advances in integrated photonics have allowed many devices and circuits to be combined into a single monolithic platform similar to CMOS technology and the advent of integrated circuits [4]. Photonics also offers an inherently broad bandwidth which, when combined with dispersion engineering, can allow for the manipulation and propagation of ultra-short pulses of light [5]. Time-multiplexing, a pulse-based encoding technique used in photonic systems, can leverage femtosecond pulses to scale information density and throughput, and can exceed clock speeds beyond what is currently possible with conventional electronics [6, 7, 8].

A crucial part of any QIP system is a measurement device capable of characterizing a component of interest. Homodyne detection is widely employed as its phase-sensitive nature can be used to reconstruct the Wigner function, a quasi-probability

distribution over two non-commuting variables which completely characterizes a quantum state [9]. Homodyne detectors can also isolate a single mode of a state of interest by shaping the spectral profile of the local oscillator appropriately [10]. This phase-sensitive and mode-selective behavior makes them well-suited for characterizing a variety of quantum states, including non-classical states. Single-photon and photon number-resolving (PNR) detectors are also common tools for state characterization and have been used to generate and measure of states with Wigner negativity [11, 12, 13, 14, 15, 16]. While homodyne and PNR detection are powerful techniques for probing quantum states of interest, their speed is ultimately constrained by the bandwidth of the electronics used to physically realize these detectors, which are limited to the GHz range.

To overcome the speed limitations of electronics, we demonstrate chip-scale all-optical Wigner tomography of squeezed vacuum (SV) using a nanophotonic optical parametric amplifier (OPA). In our previous work [17], we measured the average photon number at the output of an OPA to calculate squeezing levels. In this work, we use a fast photodetector to measure each pulse and resolve the statistical information necessary to recover the Wigner function of the input SV. We design our OPA to have low dispersion at both the pump and signal wavelengths, allowing for the distortion-free propagation and amplification of femtosecond pulses. Such an OPA-based circuit supports a maximum measurement repetition rate (i.e. clock speed) of 6.5 THz. Increased clock speeds offers crucial benefits for QIP in photonic time-multiplexed systems as faster clocks lead to shorter processing times while also increasing the maximum circuit size which can be realized for a given system [18, 19, 20]. Our results highlight nanophotonic OPAs as an important building block for chip-scale ultrafast quantum information processing systems at room temperature.

6.2 Parametric Amplifiers as Quantum Measurement Devices

Early proposals of OPAs as quantum measurement devices demonstrated loss-tolerance and detector inefficiency mitigation [21]. OPAs are particularly well-suited for this task as their phase-sensitive amplification is in principle noiseless unlike phase-insensitive amplifiers such as erbium-doped fibers and semiconductor gain media [22]. OPA-assisted balanced homodyne detection has been used to characterized fiber-based sources of SV over 43 GHz of electronic bandwidth [23]. A similar technique has also been demonstrated using the $\chi^{(3)}$ nonlinearity [24]. Other experiments have shown quantum-enhanced sensing using an SU(1,1) interferometer constructed from two OPAs for state readout [25, 26]. OPAs have also been used to

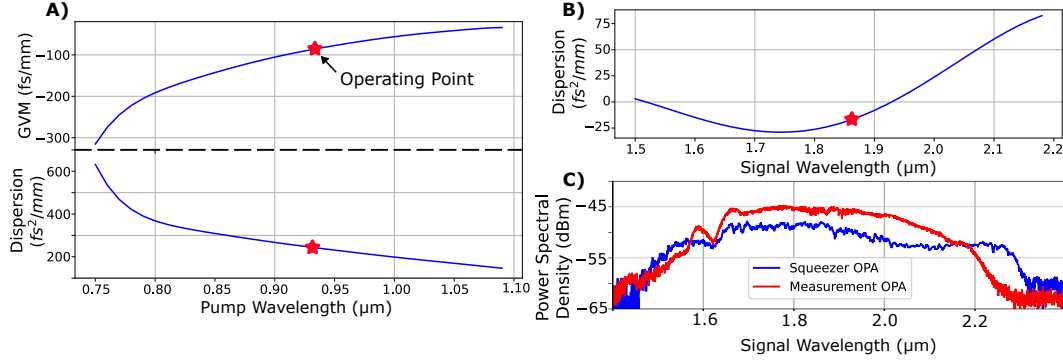


Figure 6.2: A) Pump dispersion and group-velocity mismatch (calculated at degeneracy and plotted at the pump wavelength) for our OPA. B) Signal dispersion vs wavelength. C) Parametric generation (vacuum amplification) spectra of our measurement and squeezer OPAs.

amplify weak spatially-varying signals and detect quantum correlations for imaging applications [27, 28]. All-optical feed-forward, a technique used to surpass the constraints of electronics in feed-forward schemes for quantum information processing, has been demonstrated using 3 OPAs [29]. Wigner-tomography of squeezed states using bulk OPAs has been experimentally realized [30]. OPA-based techniques have also been extended to squeezing across multiple spatial modes where direct detection is used to disentangle and analyze each mode independently [31].

Quadrature Measurement

Figure 6.1 depicts the scheme used to measure the Wigner function of a SV state encoded in a femtosecond pulse. When the SV enters the nanophotonic amplifier, its in-phase quadrature \hat{x}_ϕ is amplified by the pump while its out-of-phase quadrature \hat{p}_ϕ is deamplified. These quadratures map to the original operators of the state as [30]:

$$\hat{x}_\phi = \hat{x} \cos(\phi) + \hat{p} \sin(\phi) \quad (6.1)$$

$$\hat{p}_\phi = \hat{p} \cos(\phi) - \hat{x} \sin(\phi) \quad (6.2)$$

Where ϕ represents a relative phase between the pump and amplified signal induced by adjusting the time-delay (Δt) of the pump. After amplification, the output quadratures can be expressed as:

$$\hat{X}_\phi = \hat{x}_\phi e^g \quad (6.3)$$

$$\hat{P}_\phi = \hat{p}_\phi e^{-g} \quad (6.4)$$

where e^g , the gain of the amplifier, can be controlled by changing the pump power. The operator for the number of photons in the signal field at the output is then:

$$\hat{N}_\phi = \hat{X}_\phi^2 + \hat{P}_\phi^2 - \frac{1}{2} \quad (6.5)$$

For a large gain, the 2nd and 3rd terms of Eq.6.5 can be ignored such that:

$$\hat{N}_\phi \approx \hat{X}_\phi^2 \quad (6.6)$$

By measuring the signal intensity at the output of the OPA for each pulse, we can recover the marginal distribution $P(N, \phi)$, or the probability of detecting N photons at a measurement pump phase ϕ .

Because our OPA exhibits low dispersion over a broad bandwidth while operating in the type-0 phase matching configuration, it amplifies many orthogonal spectro-temporal modes simultaneously [32], all of which contribute to the measured $P(N, \phi)$. These modes can be calculated analytically by computing the joint spectral intensity (JSI) function of the signal and idler. Our JSI and the corresponding modes are computed and plotted in the supplementary using the dispersion parameters calculated from the waveguide geometry and the Heisenberg propagators derived in [33]. Because our JSI is inseparable ($JSI(\omega_s, \omega_i) \neq \phi(\omega_s)\phi(\omega_i)$), it is composed of multiple independent modes $\Phi(\omega_s, \omega_i)$ of the form $\Phi(\omega_s, \omega_i) = \phi(\omega_s)\phi(\omega_i)$.

At the photodetector, we use a combination of a 1700-nm long-pass filter and 1950-nm short-pass filter to suppress contributions from higher order modes. Using the measured $P(N)$ for vacuum amplification (i.e. when no signal field is sent into the OPA), we calculate a Schmidt number of 1.35 modes after filtering from the definition of $g^{(2)}$ in [34]. Contributions from the higher-order modes are quantified and separated by fitting a 2-mode photon number distribution to determine the gain of the fundamental mode as a function of ϕ . As our Schmidt number of 1.35 is close to single-mode (i.e. 1), we limit our fit to just the first two modes as contributions from higher order modes are relatively small. For a single mode, the photon number distribution is

$$P_{\langle N \rangle}^{[1]}(N, \phi) = \frac{1}{\sqrt{2\pi N \langle N(\phi) \rangle}} e^{-\frac{N}{2\langle N(\phi) \rangle}} \quad (6.7)$$

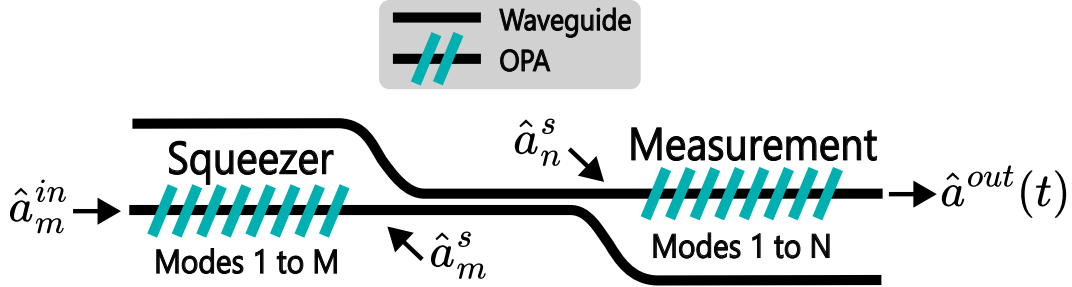


Figure 6.3: A diagram of the squeezer and measurement OPA circuit.

where $\langle N(\phi) \rangle$ is the squeezing-dependent average photon number. Convolving this distribution with itself yields the 2-mode distribution [35]:

$$P^{[2]}(N, \phi) = \int_0^\infty P_{\langle N_1 \rangle}^{[1]}(N - n, \phi) P_{\langle N_2 \rangle}^{[1]}(n, \phi) dn \quad (6.8)$$

This convolution is the probability of detecting a total of N photons across both modes as the photodetector cannot distinguish between photons arriving from different modes. These fitted distributions are then sampled and used as inputs to a maximum-likelihood reconstruction algorithm to recover the density matrix and Wigner function [36].

Multimode Cascaded Squeezing in the Heisenberg picture

We use the formalism of [37] to derive the output of a two cascaded multimode OPAs: a squeezer OPA and a measurement OPA. Figure 6.3 shows the circuit diagram. We begin with the state after the squeezer OPA (denoted with superscript s) and decompose the annihilation operator into the squeezer OPA's eigenmodes (denoted by subscript m):

$$\begin{aligned} \hat{a}^s(t) &= \sum_m \psi_m^{s*}(t) \hat{a}_m^s \\ &= \sum_m \psi_m^{s*}(t) (\cosh r_m^s \hat{a}_m^{in} + \sinh r_m^s \hat{a}_m^{in\dagger}) \end{aligned} \quad (6.9)$$

where r_m^s is the squeezing parameter of mode m . To simplify later expressions, we assume that $r_m^s = r_m^s(\phi)$ where ϕ is the phase of the squeezed vacuum relative to the measurement pump. Each eigenmode of the squeezer OPA is independently squeezed. In our experiment, we inject vacuum into the squeezer OPA, and so $\hat{a}^{in} \equiv \hat{a}^{vac}$.

After the squeezer OPA, the state is placed into the measurement OPA (superscript ms and mode subscript n) and the resulting output operator is labeled $\hat{a}^{out}(t)$. The measurement OPA amplifies its own modes as independent single-mode OPAs:

$$\begin{aligned}\hat{a}^{out}(t) &= \sum_n \psi_n^{ms*}(t) \hat{a}_n^{out} \\ &= \sum_n \psi_n^{ms*}(t) (\cosh r_n^{ms} \hat{a}_n^s + \sinh r_n^{ms} \hat{a}_n^{s\dagger})\end{aligned}\quad (6.10)$$

We can write the squeezed operators in the measurement OPA basis as a function of the mode overlaps between the measurement OPA's and squeezer OPA's eigenmodes $\sigma_{mn} = \int dt \psi_n^{ms}(t) \psi_m^{s*}(t)$

$$\begin{aligned}\hat{a}_n^s &= \int_{-\infty}^{\infty} dt \psi_n^{ms}(t) \hat{a}^s(t) \\ &= \int_{-\infty}^{\infty} dt \psi_n^{ms}(t) \sum_m \psi_m^{s*}(t) \hat{a}_m^s \\ &= \sum_m \sigma_{mn} \hat{a}_m^s\end{aligned}\quad (6.11)$$

The output annihilation operator is then

$$\begin{aligned}\hat{a}^{out}(t) &= \sum_{mn} \psi_n^{ms*}(t) (\cosh r_n^{ms} \sigma_{mn} \hat{a}_m^s + \sinh r_n^{ms} \sigma_{mn}^* \hat{a}_m^{s\dagger}) \\ &= \sum_{mn} \psi_n^{ms*}(t) (\cosh r_n^{ms} \sigma_{mn} (\cosh r_m^s \hat{a}_m^{in} + \sinh r_m^s \hat{a}_m^{in\dagger}) \\ &\quad + \sinh r_n^{ms} \sigma_{mn}^* (\cosh r_m^s \hat{a}_m^{in\dagger} + \sinh r_m^s \hat{a}_m^{in}))\end{aligned}\quad (6.12)$$

For large measurement OPA gains, we use the approximation $\cosh r_n^{ms} \approx \sinh r_n^{ms} \approx \frac{1}{2} \exp(r_n^{ms})$, when $e^{r_n^{ms}} \gg 1 \gg e^{-r_n^{ms}}$. Then, the output operator becomes:

$$\hat{a}^{out}(t) = \sum_{mn} \frac{e^{r_n^{ms}}}{2} \psi_n^{ms*}(t) (\sigma_{mn} (\cosh r_m^s \hat{a}_m^{in} + \sinh r_m^s \hat{a}_m^{in\dagger}) \quad (6.13)$$

$$+ \sigma_{mn}^* (\cosh r_m^s \hat{a}_m^{in\dagger} + \sinh r_m^s \hat{a}_m^{in})) \quad (6.14)$$

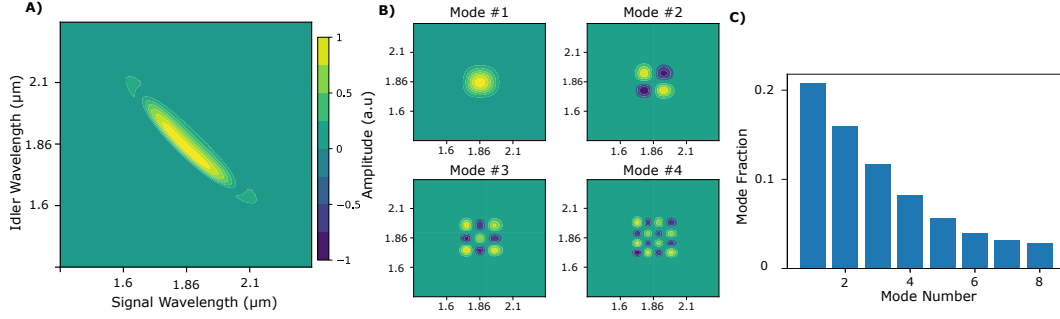


Figure 6.4: A) Joint-spectral intensity function of the squeezed vacuum produced by our OPA. B) The first four modes of the JSI calculated via the Bloch-Messiah decomposition. C) Plot of the mode number vs proportion of mode present in the JSI.

We can write the photon number operator for an individual pulse as

$$\begin{aligned}
\hat{N} &= \int_{-\Delta t}^{\Delta t} dt \hat{a}^{out\dagger}(t) \hat{a}^{out}(t) \\
&= \int dt \sum_{m,m',n,n'} \frac{e^{r_n^{ms} + r_{n'}^{ms}}}{4} \left(\psi_n^{ms}(t) (\sigma_{mn}^* (\cosh r_m^s \hat{a}_m^{in\dagger} + \sinh r_m^s \hat{a}_m^{in}) \right. \\
&\quad \left. + \sigma_{mn} (\cosh r_m^s \hat{a}_m^{in} + \sinh r_m^s \hat{a}_m^{in\dagger})) \right) \\
&\quad \left(\psi_{n'}^{ms*}(t) (\sigma_{m'n'} (\cosh r_{m'}^s \hat{a}_{m'}^{in} + \sinh r_{m'}^s \hat{a}_{m'}^{in\dagger}) \right. \\
&\quad \left. + \sigma_{m'n'}^* (\cosh r_{m'}^s \hat{a}_{m'}^{in\dagger} + \sinh r_{m'}^s \hat{a}_{m'}^{in})) \right) \\
&= \sum_{m,n} e^{2r_n^{ms}} (\text{Re}[\sigma_{mn}] e^{r_m^s} \hat{x}_m^{in} - \text{Im}[\sigma_{mn}] e^{-r_m^s} \hat{y}_m^{in})^2
\end{aligned} \tag{6.15}$$

where the integral over Δt captures the total time-duration of the pulse, and we have used the orthonormality of modes ($\int dt \psi_n(t) \psi_{n'}^*(t) = \delta_{nn'}$) to insert $\delta_{nn'}$ and $\delta_{mm'}$ and resolve m' and n' in the summation as the modes are uncorrelated in the OPA's squeezing basis.

Bandpass filtering around degeneracy suppresses the imaginary component of σ_{mn} as imaginary contributions arise from phase walk-off in the JSI away from degeneracy. Taking $\text{Im}[\sigma_{mn}] e^{-r_m^s} \ll \text{Re}[\sigma_{mn}] e^{r_m^s}$, we have:

$$\hat{N} = \sum_{m,n} \frac{e^{2r_n^{ms} + 2r_m^s}}{4} \sigma_{mn} (\hat{a}_m^{in} + \hat{a}_m^{in\dagger})^2 \tag{6.16}$$

If we take a compare to the case of no squeezing from the squeezer OPA ($\sigma_{mn} =$

$\delta_{mn}, r_m^s = 0 \forall m$):

$$\hat{N} = \sum_n \frac{e^{2r_n^{ms}}}{4} (\hat{a}_n^{in} + \hat{a}_n^{in\dagger})^2 \quad (6.17)$$

and assume M squeezer modes and N measurement modes, we show that there are now MN modes with effective squeezing parameters $r_{m,n}^{eff} = r_n^{ms} + r_m^s$, whose contributions are weighted by σ_{mn} . From here, we can use the quadrature $\hat{X} = \frac{1}{\sqrt{2}}(\hat{a} + \hat{a}^\dagger)$ to re-write Eq.6.16 as:

$$\hat{N} = \sum_{m,n} \frac{e^{2r_n^{ms} + 2r_m^s}}{8} \sigma_{mn} (\hat{X}_m^{in})^2 \quad (6.18)$$

In our experiment, we make the assumption that only the first two modes provide significant contributions to the measured statistics as our Schmidt number after filtering is 1.35, and so we truncate m and n to the range [1,2]. Furthermore, we know that σ_{mn} where m and n are of different parity are zero. This simplifies Eq.6.18 to:

$$\hat{N} = \frac{e^{2r_1^{ms} + 2r_1^s}}{8} \sigma_{11} (\hat{X}_1^{in})^2 + \frac{e^{2r_2^{ms} + 2r_2^s}}{8} \sigma_{22} (\hat{X}_2^{in})^2 \quad (6.19)$$

This allows us to model the measured photon number distribution as the sum of two independent photon number distributions. During the experiment, we treat the fast photodetector as a macroscopic photon number resolving detector such that $N \propto I_d$ where I_d is the current measured on the detector integrated over a single pulse. We connect this analysis to the measured photon number distributions in section 6.4.

Dispersion Engineering

A key advantage of using nanophotonics is the ability to control the dispersive properties of the waveguides used to realize photonic circuits. Figure 6.5 depicts our ridge waveguide geometry and material stack used for our OPAs. We fabricate our OPAs on a thin-film lithium niobate (TFLN) on silica on silicon wafers available from NanoLN. By adjusting the width, etch depth, and thin-film thickness of the waveguide, we can manipulate its dispersive properties to achieve low group velocity dispersion (GVM) at the pump and signal wavelengths while simultaneously minimizing the walk-off from group velocity mismatch (GVM) between the pump and signal [5]. Figures 6.2A-B plot the GVD for the signal/pump and GVM at degeneracy for the waveguide geometry in Fig. 6.5A. The operating wavelengths are marked with a red star. This regime of operation allows for our OPA to exhibit

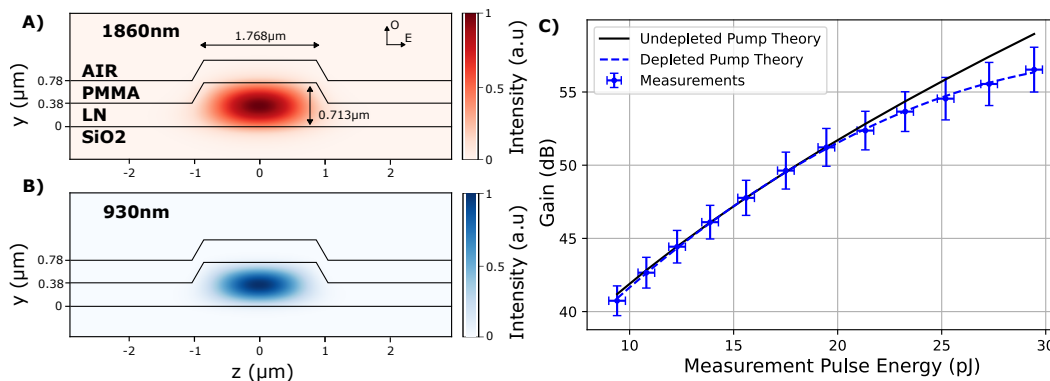


Figure 6.5: A) Signal spatial mode within our waveguide. Text on the right denotes the material stack-up with air, poly methyl methacrylate (PMMA), lithium niobate (LN) and silicon dioxide (SiO₂). Dimensions are indicated by the vertical and horizontal measurements. The ordinary and extraordinary crystal axes are denoted at the top right. B) Pump spatial mode. C) OPA gain versus measurement pump energy. Error bars are calculated from pump and signal coupling stability measurements taken before gain measurements. The depleted pump theory is taken from the Gaussian limit defined in [38].

high gain over a broad bandwidth, making it an ideal tool for studying quantum states encoded in ultrafast pulses. Our waveguide geometry achieves a GVD of $-17.3 \text{ fs}^2/\text{mm}$ at our signal wavelength of 1860 nm, $244 \text{ fs}^2/\text{mm}$ at our pump wavelength of 930 nm, and a GVM of $-87 \text{ fs}/\text{mm}$. By comparison, bulk lithium niobate has a GVD of $13.3 \text{ fs}^2/\text{mm}$ at 1860 nm, a GVD of $341 \text{ fs}^2/\text{mm}$ at 930 nm, and a GVM of $203 \text{ fs}/\text{mm}$. A thin layer of poly-methyl methacrylate (PMMA) is deposited via spin-coating on top of the waveguide which acts to perturb the effective refractive index of the waveguide and offer some tunability of the phase matching condition during fabrication. We note that our design is not perfectly optimal, and that geometries with lower dispersion have been demonstrated [5].

Figure 6.2C shows the parametric generation (i.e. vacuum amplification) spectra for the 2.5-mm OPA used for SV generation and the 5-mm OPA used for measurement. These spectra are taken at a pump pulse energy of 30 pJ. Both OPAs exhibit a 3-dB gain over $> 20 \text{ THz}$ as a result of low GVD at the signal wavelength and signal gains $> 40 \text{ dB}$ thanks to low GVM. Compared to the squeezer, the measurement OPA has a slightly narrower and more intense gain spectrum as the extra 2.5-mm of propagation allows for greater walk-off far from degeneracy and more interaction time near degeneracy.

Operating with low dispersion allows us to utilize ultrafast femtosecond pulses at

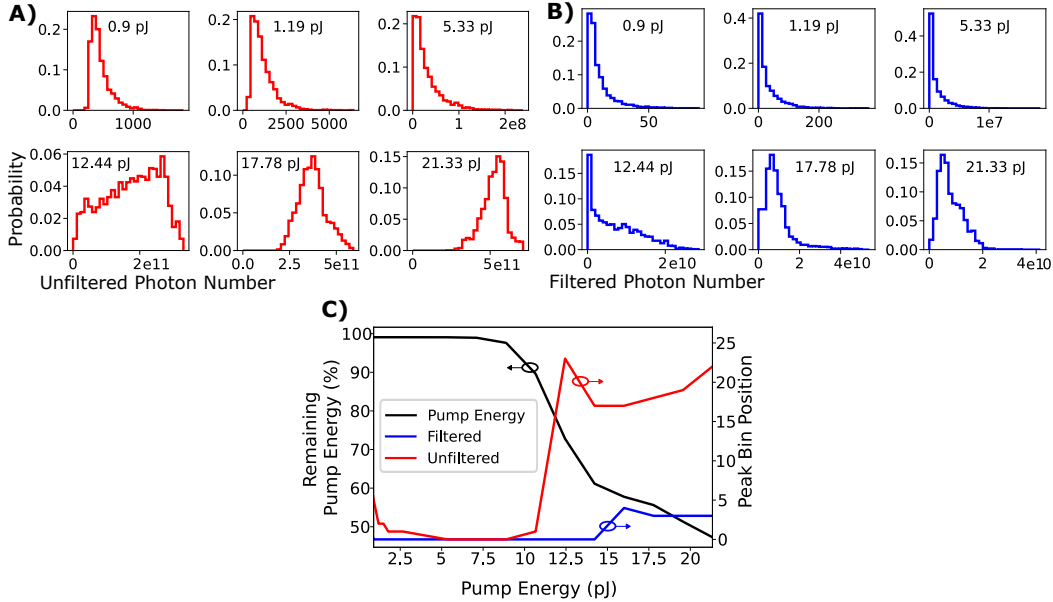


Figure 6.6: A) Simulated photon number distributions for unfiltered detection across different pump energies. B) Simulated photon number distributions for 20-nm bandpass filtered detection across different pump energies. C) A plot of the remaining pump energy after pulse propagation (lower remaining energy is a more depleted pump), and the peak histogram bin for the unfiltered and filtered simulations.

both the pump and signal frequencies. Shorter pulses are advantageous for nonlinear processes such as OPA because the high peak power from temporal confinement can achieve a stronger nonlinear interaction for the same pulse energy. This interaction is also enhanced by the tight spatial mode confinement offered by ridge waveguides. Furthermore, by shortening the length of the pump and signal pulses in the time domain, subsequent pulses can be packed closer together in time, enabling a significant boost in clock speeds for time-multiplexing. This boost also allows larger quantum circuits to be realized in cluster state architectures [18, 19, 20]. Based on the dispersive properties of our 5-mm measurement OPA and our 70-fs pump source, we estimate an upper bound on the temporal length of our SV of 154.3 fs, which gives a theoretical maximum of 6.5 THz for our clock rate [37]. This clock rate can be increased further by using a shorter OPA and a higher pump power, or more advanced dispersion engineering.

Calculation of the Joint Spectral Intensity and its Modes

Figure 6.4A shows the joint-spectral intensity function (JSI) of the squeezed vacuum we measure. We calculate our JSI using the dispersive parameters obtained

from mode simulations, the input pump pulse energy, and the resources from [33]. The modes of the JSI are found by performing the Bloch-Messiah decomposition which calculates the modes such that the correlations between pairs of modes are minimized. The first four modes are plotted in Fig. 6.4B and the fraction of the first eight modes comprising the JSI is shown in Fig. 6.4C. The JSI decomposition reveals a Schmidt mode number of 7.1. This same calculation can be repeated for the measurement OPA resulting in a Schmidt number of 3.9. Filtering before detection reduces this number to 1.35.

Pump Depletion

An important consideration for OPAs as quantum measurement devices is the depletion experienced by the pump during amplification. As the pump energy increases, the nonlinear interaction becomes more efficient, causing the pump pulse to deplete while propagating in the OPA and the gain to saturate. Figure 6.5C shows measured on-chip OPA gain vs the input pump energy. The black line represents the theoretical undepleted pump gain $G_{dB} = 10 \log_{10}(e^{b\sqrt{E}})$ where E is the pump energy in Joules and b is a found by fitting the pump energy vs gain curve in the undepleted regime. The dashed blue line represents the theoretical gain when accounting for pump depletion up to 2nd order in the Gaussian limit [38]. Around 20 pJ, the measured gain begins to saturate relative to the theoretical gain due to pump depletion effects.

Pump depletion impacts our measurement in two ways. First, the larger photon number components of the state being measured experience less gain than smaller photon number components. This phenomenon, often known as gain saturation for classical amplifiers, suppresses the larger photon number contributions to the measured distributions and distorts our measurement. This distortion can be mitigated by improving output coupling losses to allow operation at a lower pump power. We investigate this distortion experimentally in section 6.4. Second, pump depletion can be thought of as a semi-deterministic transfer of energy from the pump pulse to the signal pulse. This causes the peak of the photon number distribution to shift away from $N = 0$. We observe this effect in classical simulations which use a split-step Fourier method to simulate single-mode and multimode vacuum measurements. These simulations are detailed in the supplementary. This effect has also been observed in single-mode quantum simulations [38] and experimentally [34]. We address this issue when fitting our data with 2-mode distributions by fitting a constant offset along the N axis, leading to good agreement between the measured data and fitted distributions.

Pump Depletion in Simulation

As discussed in the main text, we model the effects of pump depletion as a shift in the peak of the photon number distribution. Figure 6.6 shows semi-classical simulation results of vacuum amplification in our OPA generated via a split-step Fourier method. As pump energy increases, the pump pulse depletes more efficiently given the peak-power-enhanced nonlinear interaction, and causes the peak of $P(N)$ to shift away from 0. Fig. 6.6B shows simulated $P(N)$ with 20-nm bandpass filtering at degeneracy before measurement. In this case, the dominant contribution to the peak shift is pump depletion as multimode effects are suppressed. The difference can be seen in Fig. 6.6A where in the unfiltered case, peak shifting is more prominent thanks to strong multimode contributions. Peak shifting as a result of pump depletion has recently been studied in single-mode quantum simulations [38] and experimentally observed [34].

Pump Depletion and Multimode Amplification in Experiment

To investigate the impact of multimode behavior and pump depletion, we measure the photon number distributions (PNDs) with and without bandpass filtering for two different devices: a 2 mm OPA and a 5 mm OPA. Both OPAs are pumped at 1045 nm with the same source as in 4 and both bandpass measurements use a 48-nm filter centered at 2090 nm. Our 5 mm OPA is the same OPA used in chapter 4 where its dispersive properties are shown in figure 4.2 and listed in section 4.1. Our 2 mm OPA has slightly lower dispersion with a GVD of $78.3 \text{ fs}^2/\text{mm}$ at 1045 nm, a GVD of $15.8 \text{ fs}^2/\text{mm}$ at 2090 nm, and a GVM of $2.6 \text{ fs}/\text{mm}$. Figures 6.7A and 6.7B show PNDs for the 2-mm device. In both the filtered and unfiltered cases, the PNDs begin to broaden as pump energy increases from both multimode and pump depletion effects. However, in the unfiltered case, the peak of the PND experiences a shift to higher photon numbers that is not observed on the filtered case. While both pump depletion and multimode amplification can lead to this behavior, we conclude that the dominant contribution to peak-shifting in the unfiltered case is multimode amplification as the bandpass filter used in Fig. 6.7B suppresses these contributions. Figures 6.7C and 6.7D show the same experiment performed on the 5-mm device where similar behavior is seen. However, the peak shifting in Fig. 6.7C is much more prominent. This is likely due to supercontinuum generation enabled both by high pump powers as well as a longer device which permits the phase walk-off needed to induce the back-and-forth conversion and generate supercontinuum.

In Figure 6.7E, we use the measured PNDs to calculate the Schmidt number using

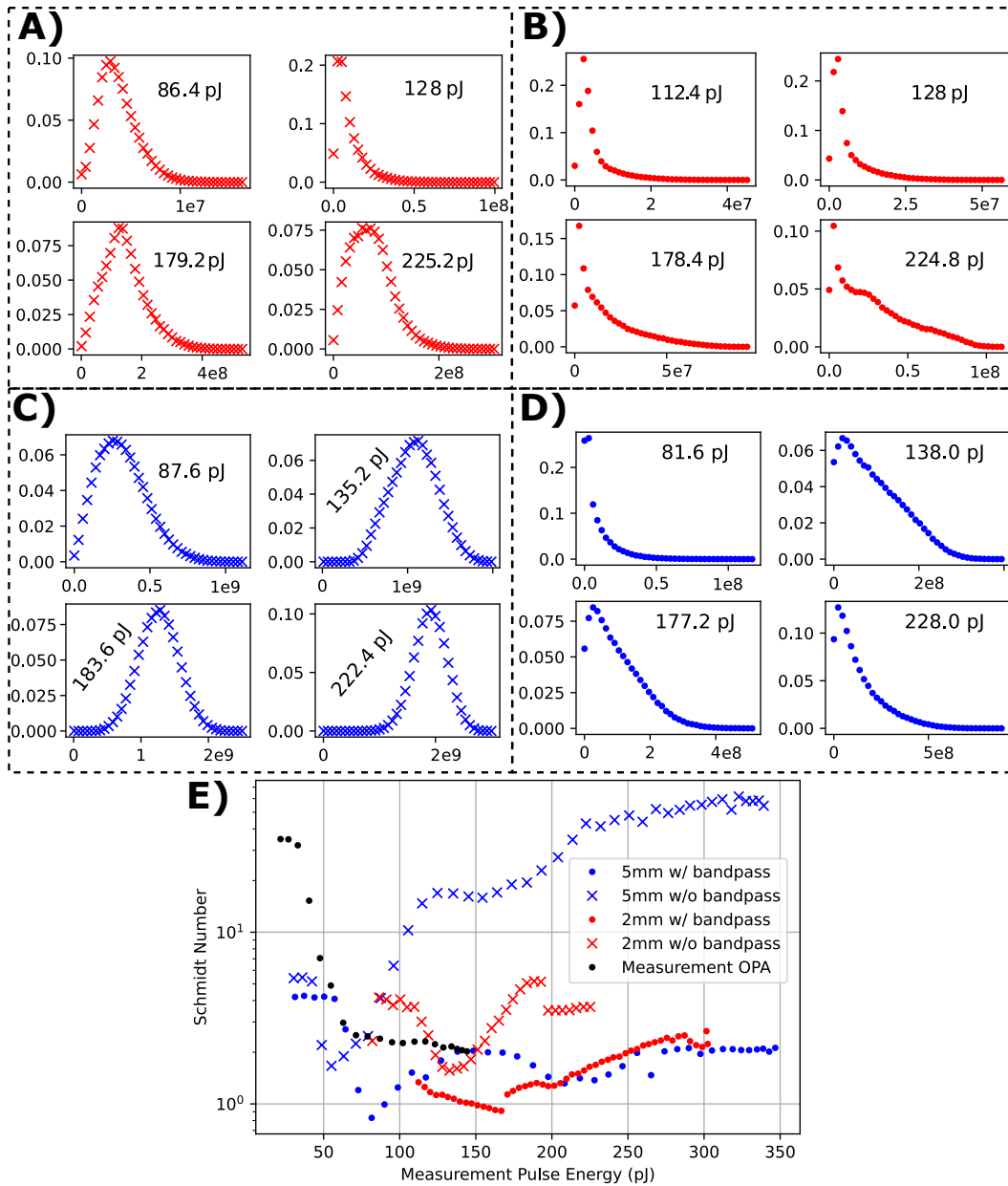


Figure 6.7: A) Photon number distributions for a 2-mm OPA with no filtering. B) Photon number distributions for a 2-mm OPA with bandpass filtering. C) Photon number distributions for a 5-mm OPA with no filtering. D) Photon number distributions for a 5-mm OPA with bandpass filtering. E) Mode number vs measurement (input) pulse energy for the 4 cases shown above as well as the measurement OPA used for tomography.

the definition in [34]. For measurements taken without filtering, we see similar behavior in which the mode number initially decreases before reaching a minimum and then increasing again. This initial decrease is seen in full quantum simulations

and can be thought of conceptually as the JSI beginning to expand along the line $\omega_s = \omega_i$ [39]. As the JSI becomes more circular, the Schmidt number decreases. We also observe this behavior when analytically calculating the JSIs for our squeezer and measurement OPAs in section 6.2. The cause behavior of the Schmidt number vs pump power after the Schmidt minima is still under investigation, but we hypothesize that this is a result of supercontinuum generation. At high pump powers, higher-order nonlinear processes turn on inside our waveguide, causing its output spectrum to become very broad and the generation of light in different modes which no longer correspond to the modes of the JSI as these are solely calculated from $\chi^{(2)}$ effects. These higher-order nonlinear processes, including effective $\chi^{(3)}$ effects from back-and-forth conversion increase the mean of the PND in such a way that the calculated $g^{(2)}(0)$ trends towards 1, causing the Schmidt number to increase. Future experiments in which output spectra are measured at every point of Fig. 6.7 could be used to verify this argument.

6.3 Experimental Setup

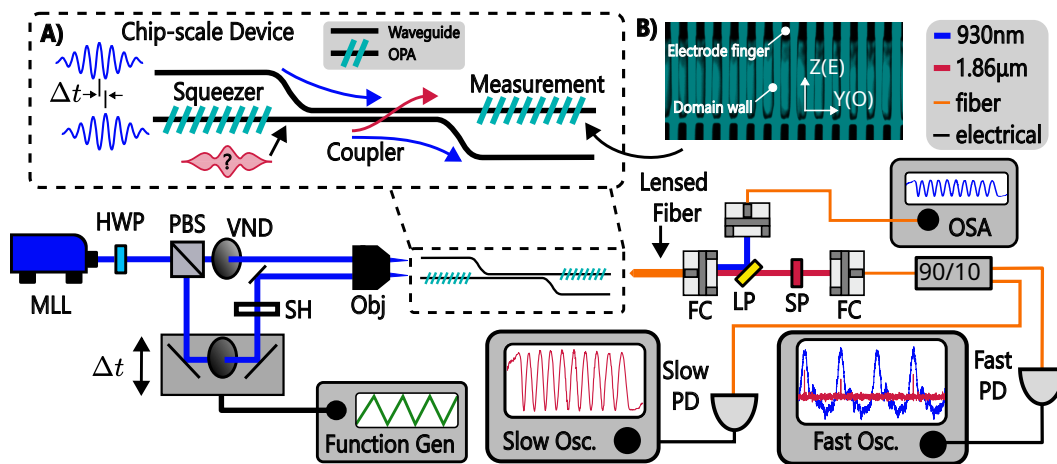


Figure 6.8: Experimental setup. MLL: Titanium:sapphire tunable mode-locked laser. PBS: polarizing beamsplitter. VND: variable neutral density filter. SH: mechanical shutter. Obj: reflective objective. FC: reflective fiber collimator. LP and SP: long-pass and short-pass wavelength filters. 90/10: fiber splitter with 90% going to the fast detector and 10% going to the slow detector. PD: photodetector. Fast Osc: 80 GSps 40 GHz oscilloscope. Slow Osc: 100 MSPS 10 MHz oscilloscope.

Figure 4.4 shows the experimental setup. An 80 MHz mode-locked titanium-sapphire laser (MLL) sends 70-fs pulses to a half-wave plate (HWP) and polarizing beamsplitter (PBS) combination to control the power splitting between the measurement and squeezer beam paths. Pump light for the squeezer OPA is sent to a

delay stage used to scan ϕ in equation 6.1. A shutter is also placed in this path to block the squeezer beam for shot-noise calibration. Two continuously-variable neutral density filters (VND) are used in both paths to fine-tune the input power. The paths are combined on a reflective objective (Obj) and focused onto the waveguide inputs for the OPAs. Figure 4.4A shows the layout of the nanophotonic circuit. In the squeezer OPA, the vacuum field around 1860 nm is squeezed by the pump to generate squeezed vacuum (SV). The SV and the remaining pump light enter an adiabatic coupler which passes at least 55% of the SV and 5% of the pump into the measurement OPA. Inside the measurement OPA, the SV is amplified by a strong pump pulse (40 pJ) to macroscopic photon levels detectable by a fast photodetector. A lensed fiber collects light from the output of the measurement OPA and directs it to a series of free-space filters used to remove remaining pump light, including the previously mentioned 1700-nm long pass and a 1950-nm short pass for limiting the measured mode number. From here, the filtered SV is collected into single-mode fiber and enters a 90/10 splitter where 90% is sent to a fast (10 GHz) photodetector and fast (80 GSPS 40 GHz) oscilloscope used to resolve individual pulses while the remaining 10% is sent to a slow (1 MHz) detector and slow (100 MSPS 10 MHz) oscilloscope used to detect the amplification fringe and determine the measurement phase ϕ .

6.4 Data Analysis

Shot-noise Calibration

To calibrate our squeezing and anti-squeezing measurements, we measure the ϕ -dependent shot noise using the slow (1 MHz) photodetector and an optical spectrum analyzer (OSA) which replaces the fast detector in Fig. 4.4. The coupler in Fig. 4.4A couples some of the 930-nm pump light used to drive the squeezer into the measurement OPA, causing it to interfere with the pump light sent into the upper port of Fig. 4.4A. Because of this interference, the gain inside the measurement OPA, and hence the shot noise, is dependent on ϕ .

Data from the shot-noise calibration procedure is shown in figure 6.9A. During calibration, the mechanical shutter is initially left open. As the relative delay of the squeezer path is scanned, the measurement amplifier oscillates between measuring squeezed (with destructive pump interference) and anti-squeezed (with constructive pump interference) quadratures, resulting in the black curve in Fig. 6.9A. The remaining pump light collected from the output is monitored on a second OSA to determine the strength of the pump interference. The shutter is then closed and the

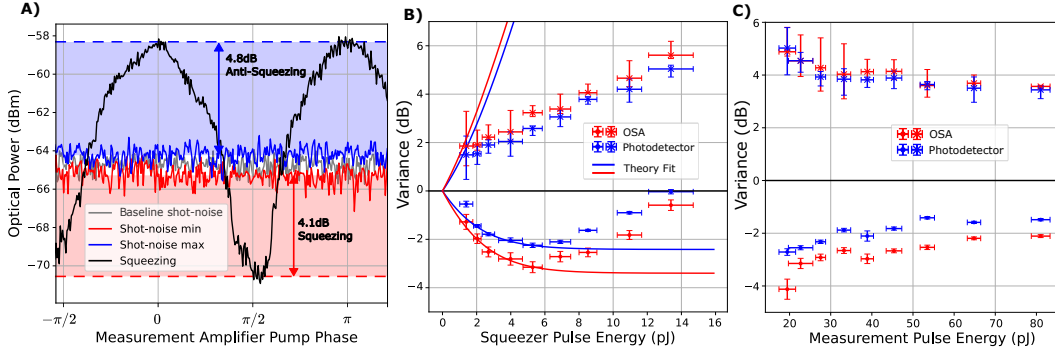


Figure 6.9: A) Squeezing measurement taken on the OSA. The black curve is the amplification fringe produced from squeezed vacuum amplified in the measurement OPA. The grey curve is the baseline shot noise at the pump power used to measure the black curve. The red and blue curves are the corrected shot-noise levels to account for pump interference in the measurement OPA. B) Variance relative to vacuum vs squeezer pulse energy with a measurement pulse energy of 30 pJ. C) Variance relative to vacuum vs measurement pulse energy. Error bars are calculated from shot-noise variations during each measurement.

baseline shot noise is measured by the OSA resulting in the gray curve in Fig. 6.9A. To find the shot-noise level corresponding to destructive pump interference (i.e. the shot-noise minimum), the intensity of the measurement OPA pump is lowered until the measured power at the pump OSA matches the minima of the previously measured pump interference. The shot-noise minimum is then measured on the slow photodetector and OSA resulting in the red curve in Fig. 6.9A. This same procedure is repeated for the shot-noise maximum to calibrate the anti-squeezing and obtain the blue curve. The pump OSA is set to measure around 970 nm to minimize any pump depletion effects. After shot-noise calibration, the squeezing is calculated as:

$$S_{\pm}^{\phi} [dB] = 10 \log_{10} \left[\frac{\langle N(\phi) \rangle}{\langle N_{vac} \rangle} \right] \quad (6.20)$$

where $\langle N(\phi) \rangle$ is proportional to the current measured at the detector, and $\langle N_{vac} \rangle$ is the calibrated shot noise. We note that the variance of the measured quadrature is proportional to the average photon number for a state with zero mean field such as SV [17].

Slow Photodetector Measurements

Figure 6.9B shows the measured squeezing on the slow photodetector and OSA as a function of the input pulse energy for the squeezer waveguide with a measurement

pulse energy of 30 pJ. For these measurements, the 1950-nm long-pass filter is removed to accentuate the impact of multiple modes (a Schmidt number of 2.8). Because the OSA uses a 2-nm bandpass filter, it can better suppress higher-order modes to isolate the squeezing in the fundamental mode [17, 33]. For the photodetector, the presence of higher-order modes with less squeezing reduces overall measured squeezing as the photodetector is not mode-sensitive and measures the squeezing as averaged over all modes.

At low squeezer pulse energies, the measured squeezing is limited by the gain available in the squeezer OPA and grows as the pulse energy is increased. After 5 pJ, the observed squeezing begins to decrease with increasing pulse energy. Two phenomena contribute to this behavior. First, the finite phase noise of the pump laser causes a portion of the anti-squeezed quadrature to leak into the measurement of the squeezed quadrature. Raising the squeezer gain increases the contribution of the anti-squeezing to the measurement and reduces the measured squeezing. This increased gain produces more squeezing, but the noise reduction in the squeezed quadrature is asymptotically limited by the finite efficiency of the coupler while the noise of the anti-squeezed quadrature is not (see solid theory curves in Fig. 6.9B). Second, gain saturation in the measurement amplifier increases with input power and further degrades measured squeezing.

The effects of gain saturation on measured squeezing can be more easily seen in Fig. 6.9C which plots the squeezing values vs the measurement pulse energy for a fixed squeezer energy of 5 pJ. As the measurement pulse energy is decreased, the behavior of the measurement OPA becomes more linear with less gain compression, leading to higher measured squeezing and anti-squeezing. In the undepleted pump regime, measured squeezing and anti-squeezing will follow Eq.6.21 and remain unchanged with small changes in pump energy. Hence, we know all measurements in Fig. 6.9B are taken in the pump depletion regime as the measured anti-squeezing deviates from the theoretical model calculated using the efficiency of the coupler. This is also confirmed from Fig. 6.5C where pump depletion effects take hold around 20 pJ. Below 20 pJ, the shot noise no longer clears the electronic noise floor of the OSA, preventing squeezing measurements at lower measurement pump energies. For this reason, data points in Fig. 6.9B are taken at a pump energy of 30pJ to improve SNR and shrink vertical error bars while sacrificing some measurable squeezing (3 dB at 30 pJ pump compared to 4.1 dB at 20 pJ pump in Fig. 6.9B and C respectively).

The solid lines plotted in Fig. 6.9B are calculated from the theoretical measured

squeezing as a function of the coupling loss from the squeezer to measurement OPA. As SV passes through the coupler, some of the light is lost as a result of fabrication imperfections in the coupler. This light is replaced with vacuum noise, causing lower squeezing and anti-squeezing values to be measured [40]. For a measurement efficiency η , the measured squeezing can be modeled as:

$$S_{\pm}^{\eta} [dB] = 10 \log_{10} [(1 - \eta) + \eta e^{\pm 2r}] \quad (6.21)$$

where r is the on-chip squeezer gain in natural log units. Using this fit, we estimate an effective η of 55% at 1860 nm. This fit includes squeezing lost to inefficiencies in our coupler as well as losses to nonlinear behavior in the measurement OPA. We expect η to be dominated by the coupler losses given the characterization measurements taken previously of this device [17]. The vacuum noise injected from losses contaminates the SV, resulting in a state with reduced squeezing and anti-squeezing measured by the measurement OPA.

Equation 6.21 also allows us to calculate the expected anti-squeezing, however, the measured data has a stark divergence from the expected trend. This is a result of gain-compression in the measurement OPA. Because the measurement OPA operates in the pump-depleted regime, the anti-squeezed vacuum cannot be sufficiently amplified to reflect the true anti-squeezing entering the OPA. The same is true for the squeezing measurements as the shot-noise level becomes compressed, leading to lower measured squeezing.

Pulse-to-pulse Measurements

Fast photodetector measurements resolve the pulse-to-pulse intensity and provide the statistical information necessary to resolve $P(N, \phi)$ and recover the Wigner function. During a fast measurement, the shutter is initially left open, and the fast oscilloscope is triggered using the voltage applied to the piezo driving the squeezer's delay stage to coincide with the middle of the ϕ scan. Data from the slow oscilloscope is used to determine ϕ and estimate the coupling stability based on measurement-to-measurement variations in the shot noise. After recording data, the shutter is closed to block the squeezer and the measurement is repeated to find the calibrated shot-noise level.

Figure 6.10 shows results gathered from fast photodetector measurements for a squeezer pulse energy of 5 pJ and a measurement pulse energy of 45 pJ. This mea-

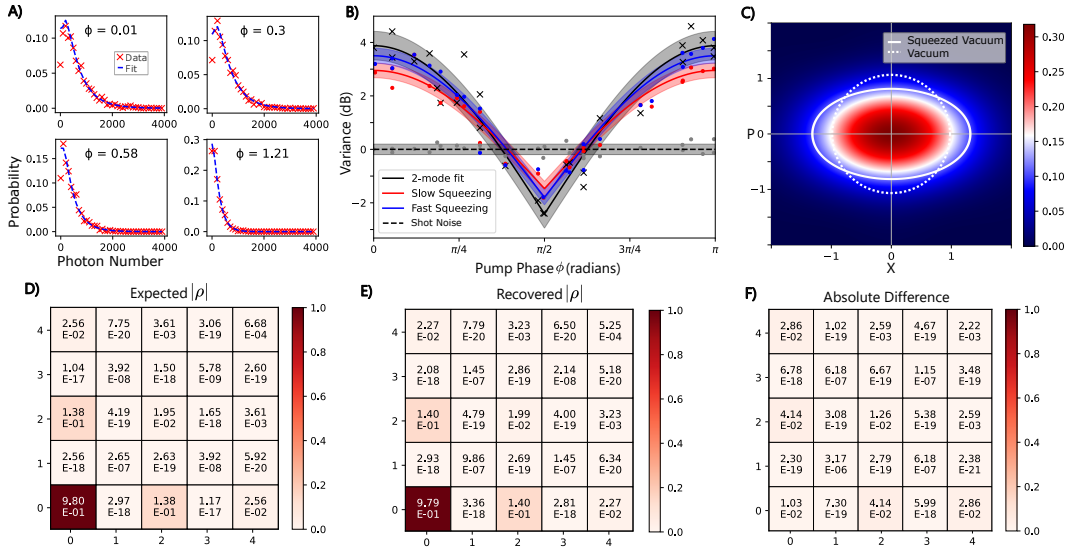


Figure 6.10: A) Sample photon number distributions from fast measurements at different ϕ . Red points are data, and the blue curve is a 2-mode fit. B) Photon number variance vs ϕ for slow, fast (pulse-to-pulse) measurements and the 1st mode of a 2-mode fit. Solid lines are the expected cosine dependence taken from [30]. C) Recovered squeezed vacuum Wigner function. Solid and dashed white lines lie along the $1/(e\pi)$ contours. D) Expected density matrix (ρ) based on measured squeezing and anti-squeezing. E) Recovered ρ . F) Absolute difference between expected and recovered ρ .

surement pulse energy was chosen to satisfy SNR requirements at the fast photodetector given the loss between the chip and detector. Sample measured histograms at 4 different phases are plotted in Fig. 6.10A. Each histogram corresponds to a single data point in Fig. 6.10B. For each measurement, we fit a 2-mode photon number distribution model to extract the variance of the fundamental mode as a function of ϕ . Figure 6.10B shows these measurements for three cases: slow photodetector measurements, fast photodetector measurements, and the 2-mode fit. Slow measurement values are calculated from the slow oscilloscope trace using the method outlined in section 6.4. Because of the photon number offset resulting from pump depletion, the numerator and denominator of Eq.6.20 have a small but constant offset, resulting in the measured squeezing and anti-squeezing being underestimated. Fast measurement values are calculated using the variance of the photon numbers measured at the fast detector. This overcomes the offset problem and measures more squeezing and anti-squeezing, but these measurements are still contaminated with remaining contributions from higher-order modes. The 2-mode fit addresses this problem by isolating the variance as a function of ϕ for the fundamental mode,

leading to higher measured squeezing and anti-squeezing. After performing this fit for all measurements, the distributions are re-sampled and fed into a maximum likelihood algorithm which calculates the Wigner function (Fig. 6.10C). We extract a squeezing in the fundamental mode of 2.41 ± 0.34 dB and an anti-squeezing of 3.87 ± 0.61 dB. Figure 6.10E shows the recovered density matrix corresponding to the Wigner function plotted in Fig. 6.10C. We show the expected density matrix given the measured squeezing and anti-squeezing in Fig. 6.10D, and the absolute difference between the expected and recovered in Fig. 6.10F where we calculate a fidelity of 0.9998 ± 0.0001 . This fidelity serves as a sanity-check to ensure our data analysis is not introducing distortions into the measurement. While our fitting strategy limits us to states with known distributions, we can overcome this limitation with tighter bandpass filtering to better reject higher-order modes. Our losses between the chip and fiber (10 dB) and from our filter setup (6 dB) currently prevent us from tighter filtering as the remaining light is no longer intense enough to provide a sufficient signal-to-noise ratio at the fast photodetector.

6.5 Conclusion

We have demonstrated OPA-based Wigner tomography for squeezed vacuum in the ultrafast regime using dispersion-engineered TFLN. This is, to the extent of the knowledge of the authors, the first demonstration of all-optical quantum state tomography on-chip. The low dispersion of our OPA design allows operation with ultra-short pulses to exceed the bandwidth of traditional measurement techniques and access a new regime of THz repetition-rate measurement and computation. Achieving THz clock rates is a fundamental advancement for time-multiplexed systems such as cluster states and measurement-based quantum computation as higher clock rates translates to faster computation and allows for larger quantum circuits to be realized.

Our THz claim is based on dispersion calculations derived from the waveguide geometry measured using atomic force microscopy. We also note that similar dispersion-engineered OPAs with faster clock rates than the one presented here have been experimentally characterized [41]. Speed limitations imposed by the photodetector bandwidth are present in our experiment, but can be overcome with fast demultiplexing schemes which we elaborate in the supplementary.

Because we only measure intensity, our current experimental implementation is limited to tomography of states with zero mean field. However, OPA-based state

tomography can be generalized to any arbitrary state by implementing either homodyne detection or a displacement scheme at the output, both of which are mature technologies [42, 11, 43, 44, 45]. As discussed in earlier sections, experimental limitations stemming from high losses between the chip and fast photodetector introduce measurement distortion from pump depletion and multimode effects. Both of these problems can be solved with narrower bandpass filtering and modest improvements in detection efficiency to allow for the measurement OPA to operate in the undepleted pump regime.

To conclude, we show that dispersion-engineered nanophotonic OPAs can serve as quantum measurement devices, paving the way for ultrafast quantum information processing to be realized in a room-temperature chip-scale platform.

6.6 Acknowledgements

Device nanofabrication was performed at the Kavli Nanoscience Institute (KNI) at Caltech. The authors gratefully acknowledge support from ARO grant no. W911NF-23-1-0048, NSF grant no. 1918549, AFOSR award FA9550-23-1-0755, DARPA award D23AP00158, the Center for Sensing to Intelligence at Caltech, the Alfred P. Sloan Foundation, and NASA/JPL.

References

- [1] Christian L Degen, Friedemann Reinhard, and Paola Cappellaro. “Quantum sensing”. In: *Reviews of modern physics* 89.3 (2017), p. 035002.
- [2] Nicolas Gisin and Rob Thew. “Quantum communication”. In: *Nature photonics* 1.3 (2007), pp. 165–171.
- [3] Horowitz Mark, Grumblin Emily, National Academies of Sciences Engineering, Medicine, et al. *Quantum computing: progress and prospects*. The National Academies Press, 2019.
- [4] Lars Thylén and Lech Wosinski. “Integrated photonics in the 21st century”. In: *Photonics Research* 2.2 (2014), pp. 75–81.
- [5] Luis Ledezma, Ryoto Sekine, Qiushi Guo, Rajveer Nehra, Saman Jahani, and Alireza Marandi. “Intense optical parametric amplification in dispersion-engineered nanophotonic lithium niobate waveguides”. In: *Optica* 9.3 (2022), pp. 303–308.
- [6] Christian Leefmans, Avik Dutt, **James Williams**, Luqi Yuan, Midya Parto, Franco Nori, Shanhui Fan, and Alireza Marandi. “Topological dissipation in a time-multiplexed photonic resonator network”. In: *Nature Physics* 18.4 (2022), pp. 442–449.

- [7] Gordon HY Li, Midya Parto, Jinhao Ge, Qing-Xin Ji, Maodong Gao, Yan Yu, **James Williams**, Robert M Gray, Christian R Leefmans, Nicolas Englebert, et al. “All-optical computing with beyond 100-GHz clock rates”. In: *arXiv preprint arXiv:2501.05756* (2025).
- [8] Yunping Bai, Xingyuan Xu, Mengxi Tan, Yang Sun, Yang Li, Jiayang Wu, Roberto Morandotti, Arnan Mitchell, Kun Xu, and David J Moss. “Photonic multiplexing techniques for neuromorphic computing”. In: *Nanophotonics* 12.5 (2023), pp. 795–817.
- [9] Warit Asavanant, Kota Nakashima, Yu Shiozawa, Jun-Ichi Yoshikawa, and Akira Furusawa. “Generation of highly pure Schrödinger’s cat states and real-time quadrature measurements via optical filtering”. In: *Optics Express* 25.26 (2017), pp. 32227–32242.
- [10] Jonathan Roslund, Renné Medeiros De Araujo, Shifeng Jiang, Claude Fabre, and Nicolas Treps. “Wavelength-multiplexed quantum networks with ultrafast frequency combs”. In: *Nature Photonics* 8.2 (2014), pp. 109–112.
- [11] Rajveer Nehra, Aye Win, Miller Eaton, Reihaneh Shahrokhshahi, Niranjana Sridhar, Thomas Gerrits, Adriana Lita, Sae Woo Nam, and Olivier Pfister. “State-independent quantum state tomography by photon-number-resolving measurements”. In: *Optica* 6.10 (2019), pp. 1356–1360.
- [12] Kaisa Laiho, Katiúscia N Cassemiro, David Gross, and Christine Silberhorn. “Probing the negative Wigner function of a pulsed single photon point by point”. In: *Physical review letters* 105.25 (2010), p. 253603.
- [13] Kan Takase, Jun-ichi Yoshikawa, Warit Asavanant, Mamoru Endo, and Akira Furusawa. “Generation of optical Schrödinger cat states by generalized photon subtraction”. In: *Physical Review A* 103.1 (2021), p. 013710.
- [14] Thomas Gerrits, Scott Glancy, Tracy S Clement, Brice Calkins, Adriana E Lita, Aaron J Miller, Alan L Migdall, Sae Woo Nam, Richard P Mirin, and Emanuel Knill. “Generation of optical coherent-state superpositions by number-resolved photon subtraction from the squeezed vacuum”. In: *Physical Review A* 82.3 (2010), p. 031802.
- [15] Jun-ichi Yoshikawa, Warit Asavanant, and Akira Furusawa. “Purification of photon subtraction from continuous squeezed light by filtering”. In: *Physical Review A* 96.5 (2017), p. 052304.
- [16] Demid V Sychev, Alexander E Ulanov, Anastasia A Pushkina, Matthew W Richards, Ilya A Fedorov, and Alexander I Lvovsky. “Enlargement of optical Schrödinger’s cat states”. In: *Nature Photonics* 11.6 (2017), pp. 379–382.
- [17] Rajveer Nehra, Ryoto Sekine, Luis Ledezma, Qiushi Guo, Robert M Gray, Arkadev Roy, and Alireza Marandi. “Few-cycle vacuum squeezing in nanophotonics”. In: *Science* 377.6612 (2022), pp. 1333–1337.

- [18] Warit Asavanant, Yu Shiozawa, Shota Yokoyama, Baramée Charoensombutamon, Hiroki Emura, Rafael N Alexander, Shuntaro Takeda, Jun-ichi Yoshikawa, Nicolas C Menicucci, Hidehiro Yonezawa, et al. “Generation of time-domain-multiplexed two-dimensional cluster state”. In: *Science* 366.6463 (2019), pp. 373–376.
- [19] Mikkel V Larsen, Xueshi Guo, Casper R Breum, Jonas S Neergaard-Nielsen, and Ulrik L Andersen. “Deterministic generation of a two-dimensional cluster state”. In: *Science* 366.6463 (2019), pp. 369–372.
- [20] Lars S Madsen, Fabian Laudenbach, Mohsen Falamarzi Askarani, Fabien Rortais, Trevor Vincent, Jacob FF Bulmer, Filippo M Miatto, Leonhard Neuhaus, Lukas G Helt, Matthew J Collins, et al. “Quantum computational advantage with a programmable photonic processor”. In: *Nature* 606.7912 (2022), pp. 75–81.
- [21] Carlton M Caves. “Quantum-mechanical noise in an interferometer”. In: *Physical Review D* 23.8 (1981), p. 1693.
- [22] Alberto M Marino, NV Corzo Trejo, and Paul D Lett. “Effect of losses on the performance of an SU (1, 1) interferometer”. In: *Physical Review A—Atomic, Molecular, and Optical Physics* 86.2 (2012), p. 023844.
- [23] A. Inoue, T. Kashiwazaki, T. Yamashima, N. Takanashi, T. Kazama, K. Enbutsu, K. Watanabe, T. Umeki, M. Endo, and A. Furusawa. “Toward a multi-core ultra-fast optical quantum processor: 43-GHz bandwidth real-time amplitude measurement of 5-dB squeezed light using modularized optical parametric amplifier with 5G technology”. In: *Applied Physics Letters* 122.10 (Mar. 2023), p. 104001. ISSN: 0003-6951, 1077-3118. DOI: 10.1063/5.0137641. URL: <https://pubs.aip.org/apl/article/122/10/104001/2879083/Toward-a-multi-core-ultra-fast-optical-quantum>.
- [24] Yaakov Shaked, Yoad Michael, Rafi Z Vered, Leon Bello, Michael Rosenbluh, and Avi Pe’er. “Lifting the bandwidth limit of optical homodyne measurement with broadband parametric amplification”. In: *Nature communications* 9.1 (2018), p. 609.
- [25] G. Frascella, E. E. Mikhailov, N. Takanashi, R. V. Zakharov, O. V. Tikhonova, and M. V. Chekhova. “Wide-field SU(1,1) interferometer”. In: *Optica* 6.9 (Sept. 2019), pp. 1233–1236. DOI: 10.1364/OPTICA.6.001233. URL: <https://opg.optica.org/optica/abstract.cfm?URI=optica-6-9-1233>.
- [26] Florian Hudelist, Jia Kong, Cunjin Liu, Jietai Jing, ZY Ou, and Weiping Zhang. “Quantum metrology with parametric amplifier-based photon correlation interferometers”. In: *Nature communications* 5.1 (2014), p. 3049.
- [27] Michael L Marable, Sang-Kyung Choi, and Prem Kumar. “Measurement of quantum-noise correlations in parametric image amplification”. In: *Optics Express* 2.3 (1998), pp. 84–92.

- [28] Yi Sun, Haohua Tu, Sixian You, Chi Zhang, Yuan-Zhi Liu, and Stephen A Boppart. “Detection of weak near-infrared optical imaging signals under ambient light by optical parametric amplification”. In: *Optics letters* 44.17 (2019), pp. 4391–4394.
- [29] Taichi Yamashima, Takahiro Kashiwazaki, Takumi Suzuki, Rajveer Nehra, Tomohiro Nakamura, Asuka Inoue, Takeshi Umeki, Kan Takase, Warit Asavanant, Mamoru Endo, et al. “All-optical measurement-device-free feedforward enabling ultra-fast quantum information processing”. In: *arXiv preprint arXiv:2410.20693* (2024).
- [30] Mahmoud Kalash and Maria V Chekhova. “Wigner function tomography via optical parametric amplification”. In: *Optica* 10.9 (2023), pp. 1142–1146.
- [31] Ismail Barakat, Mahmoud Kalash, Dennis Scharwald, Polina Sharapova, Norbert Lindlein, and Maria Chekhova. “Simultaneous measurement of multi-mode squeezing through multimode phase-sensitive amplification”. In: *Optica Quantum* 3.1 (2025), pp. 36–44.
- [32] Alfred B U’Ren, Christine Silberhorn, Reinhard Erdmann, Konrad Banaszek, Warren P Grice, Ian A Walmsley, and Michael G Raymer. “Generation of pure-state single-photon wavepackets by conditional preparation based on spontaneous parametric downconversion”. In: *arXiv preprint quant-ph/0611019* (2006).
- [33] Martin Houde and Nicolás Quesada. “Waveguided sources of consistent, single-temporal-mode squeezed light: The good, the bad, and the ugly”. In: *AVS Quantum Science* 5.1 (2023).
- [34] Jefferson Flórez, Jeff S Lundeen, and Maria V Chekhova. “Pump depletion in parametric down-conversion with low pump energies”. In: *Optics Letters* 45.15 (2020), pp. 4264–4267.
- [35] Noah Lordi, Eugene J Tsao, Alexander J Lind, Scott A Diddams, and Joshua Combes. “Quantum theory of temporally mismatched homodyne measurements with applications to optical-frequency-comb metrology”. In: *Physical Review A* 109.3 (2024), p. 033722.
- [36] William Bidle. “Optical Quantum State Tomography”. In: *Department of Physics & Astronomy* (2023).
- [37] Wojciech Wasilewski, Alexander I Lvovsky, Konrad Banaszek, and Czesław Radzewicz. “Pulsed squeezed light: Simultaneous squeezing of multiple modes”. In: *Physical Review A* 73.6 (2006), p. 063819.
- [38] Karthik Chinni and Nicolás Quesada. “Beyond the parametric approximation: Pump depletion, entanglement, and squeezing in macroscopic down-conversion”. In: *Physical Review A* 110.1 (2024), p. 013712.

- [39] Martin Houde, Liam Beaudoin, Kazuki Hirota, Rajveer Nehra, and Nicolás Quesada. “Ultrashort-pulse-pumped, single-mode type-0 squeezers in lithium niobate nanophotonics”. In: *arXiv preprint arXiv:2412.17708* (2024).
- [40] Charles H Henry and Rudolf F Kazarinov. “Quantum noise in photonics”. In: *Reviews of Modern Physics* 68.3 (1996), p. 801.
- [41] Qiushi Guo, Ryoto Sekine, Luis Ledezma, Rajveer Nehra, Devin J Dean, Arkadev Roy, Robert M Gray, Saman Jahani, and Alireza Marandi. “Femtojoule femtosecond all-optical switching in lithium niobate nanophotonics”. In: *Nature Photonics* 16.9 (2022), pp. 625–631.
- [42] Rajveer Nehra, Changhun Oh, Liang Jiang, and Alireza Marandi. “All-optical loss-tolerant distributed quantum sensing”. In: *arXiv preprint arXiv:2407.13654* (2024).
- [43] Kaisa Laiho, Katiúscia N. Casseiro, David Gross, and Christine Silberhorn. “Probing the Negative Wigner Function of a Pulsed Single Photon Point by Point”. In: *Phys. Rev. Lett.* 105 (25 Dec. 2010), p. 253603. DOI: 10.1103/PhysRevLett.105.253603. URL: <https://link.aps.org/doi/10.1103/PhysRevLett.105.253603>.
- [44] Mikkel V Larsen, Xueshi Guo, Casper R Breum, Jonas S Neergaard-Nielsen, and Ulrik L Andersen. “Deterministic multi-mode gates on a scalable photonic quantum computing platform”. In: *Nature Physics* 17.9 (2021), pp. 1018–1023.
- [45] Akito Kawasaki, Ryuhoh Ide, Hector Brunel, Takumi Suzuki, Rajveer Nehra, Katsuki Nakashima, Takahiro Kashiwazaki, Asuka Inoue, Takeshi Umeki, Fumihiko China, et al. “Broadband generation and tomography of non-Gaussian states for ultra-fast optical quantum processors”. In: *Nature Communications* 15.1 (2024), p. 9075.

Chapter 7

OUTLOOK

"If I had more time, I would have written a shorter thesis."

7.1 Challenges with TFLN and the Future of Nonlinear Photonics

The ultrafast technology studied in this thesis has been made possible by thin-film lithium niobate (TFLN), a versatile platform for nonlinear photonics. While a variety of useful devices and circuits have been demonstrated on TFLN, many engineering challenges still exist. Compared to CMOS foundrys, fabrication techniques for TFLN are still in their infancy. One of the more pressing challenges is etching. While propagation losses of around 0.2 dB/cm have been demonstrated [1], these losses are still large compared to Si and SiN platforms which have achieved losses as low as 0.06 dB/cm [2]. This is not a significant problem for classical operation, but quantum signals are severely impacted by loss, and many advanced techniques for quantum information processing including non-demolition measurements require a nonlinear coupling to loss ratio (i.e. $\frac{g}{\kappa}$) greater than 1 [3]. Furthermore, physical etch processes such as ion milling or inductively-coupled plasma reactive ion etching (ICP-RIE) currently hold the record for waveguide losses. Because these processes are physical, the etched LN is not carried away and is instead redeposited near the waveguide and on adjacent devices. This redeposition presents challenges as its removal is nontrivial and often requires aggressive chemical cleaning techniques which can damage or destroy devices and waveguides.

For nonlinear devices, achieving phase-matching at a desired wavelength remains experimentally difficult. Small variations in the thickness of the thin-film can lead to large changes in the phase-matching wavelength. Some groups have addressed this problem by measuring the thin-film thickness along the length of the target waveguide region and then adjusting either the waveguide width or poling period to compensate for thickness variations [4, 5]. In **Chapter 6**, we used a thin-layer of PMMA to tune the phase matching condition. However, this solution was somewhat of an inconvenience as it also caused an undesirable increase in the dispersion of the waveguide. We also had the convenience of using a tunable ultrafast laser to find the phase matching. Other groups have tuned phase-matching by selectively etching the LN or depositing SiO₂ on top until the device operates at the desired

wavelength [6]. While phase-mismatched nonlinear devices can still be made to work by changing the input wavelength, this strategy limits system operation overall as now other components, which may have been designed to operate at the target phase-matching wavelength, must now also operate at this new wavelength.

While LN is prized for its large $\chi^{(2)}$ coefficient, it is otherwise not an optically-active material. To create sources or detectors on TFLN, other active materials such as semiconductors must be heterogeneously integrated with passive TFLN devices. This has been demonstrated for III-V gain media [7, 8] as well as other passive platforms such as SiN [9] and silicon-based photodetectors [10]. However, heterogeneous integration is also difficult to develop and implement successfully. This raises an obvious question: is it easier to integrate other platforms onto TFLN, or is it easier to integrate TFLN onto other platforms? Other groups have begun to take the latter approach by creating "coupons" of TFLN which are then bonded to other platforms [11]. This avoids difficulties in fabricating low-loss waveguides through direct etching, but introduces challenges in reducing losses as light enters and exits the coupon region. Based on the fabrication challenges in TFLN and the need for optically-active features enabled by different materials, it is likely that the future of integrated nonlinear photonics will trend towards some form of heterogeneous integration. Just as early electronics designers dreamed of the day they could implement millions of diverse functional blocks on a single platform, so do we now for photonics.

7.2 Lifting the Electronic Bandwidth

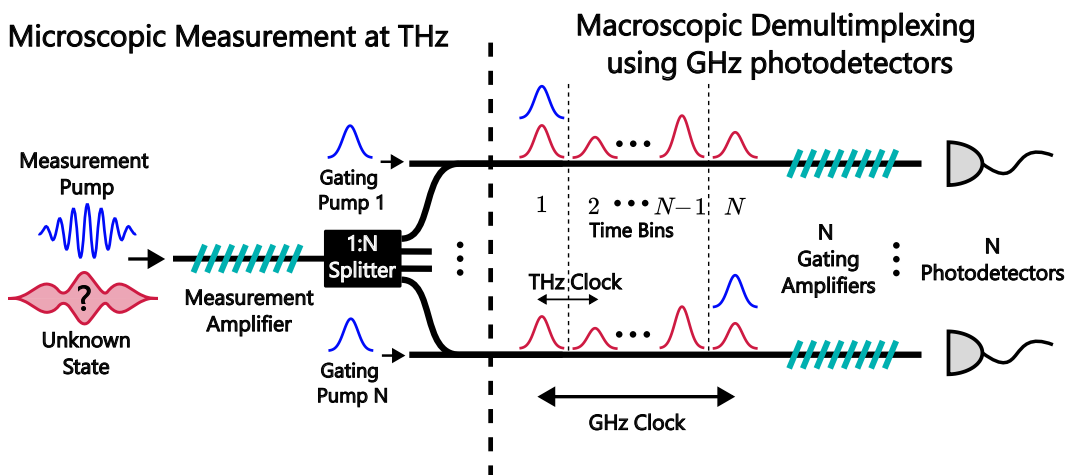


Figure 7.1: A demultiplexing circuit used to transition from a clock rate f to a clock rate $\frac{f}{N}$.

We've made the claim that our OPAs can operate at clock speeds faster than 1 THz, well beyond what is achievable with conventional electronics. However, in every experiment, we have employed electronic detection to measure optical signals and translate them into digital data. This problem of needing to return to the electronic domain will continue to exist until we use an all-optical computer to process experimental data [12].

To overcome this, we can employ OPAs as fast switches to demultiplex a clock rate of f down to $\frac{f}{N}$ using N OPAs and photodetectors. Figure 7.1 shows an example demultiplexer circuit design. An unknown quantum state is amplified and measured inside of the measurement OPA. After measurement, we are left with classical information robust to losses which we split into N channels. Once N clock cycles elapse, we have N pulses in each of the N channels. For each channel, a second pump pulse dubbed the "gating pump" is sent in to pump the gating amplifier. To achieve demultiplexing, each gating pump is time delayed such that in channel i , the i 'th pulse will be amplified in the gating amplifier while all other pulses will remain unamplified. While each of the N photodetectors will see a THz stream of pulses, only one out of every N of these pulses will be amplified enough to produce an electronic signal at the photodetector output. Hence, by correctly setting the delays of the gating pump pulses, we can selectively send each pulse to a different photodetectors and effectively lower the system clock rate by a factor of N . The feasibility dispersion-engineered OPAs as switches for ultrafast demultiplexing was first studied in [13], however similar schemes have also been presented elsewhere in literature [12].

References

- [1] Guanyu Chen, Nanxi Li, Jun Da Ng, Hong-Lin Lin, Yanyan Zhou, Yuan Hsing Fu, Lennon Yao Ting Lee, Yu Yu, Ai-Qun Liu, and Aaron J Danner. "Advances in lithium niobate photonics: development status and perspectives". In: *Advanced Photonics* 4.3 (2022), pp. 034003–034003.
- [2] Xingchen Ji, Yoshitomo Okawachi, Andres Gil-Molina, Mateus Corato-Zanarella, Samantha Roberts, Alexander L Gaeta, and Michal Lipson. "Ultra-Low-Loss Silicon Nitride Photonics Based on Deposited Films Compatible with Foundries". In: *Laser & Photonics Reviews* 17.3 (2023), p. 2200544.
- [3] Ryotatsu Yanagimoto, Rajveer Nehra, Ryan Hamerly, Edwin Ng, Alireza Marandi, and Hideo Mabuchi. "Quantum nondemolition measurements with optical parametric amplifiers for ultrafast universal quantum information processing". In: *PRX Quantum* 4.1 (2023), p. 010333.

- [4] Junjie He, Lian Liu, Mianjie Lin, Houhong Chen, and Fei Ma. “Efficient second-harmonic generation in adapted-width waveguides based on periodically poled thin-film lithium niobate”. In: *Micromachines* 15.9 (2024), p. 1145.
- [5] Pao-Kang Chen, Ian Briggs, Chaohan Cui, Liang Zhang, Manav Shah, and Linran Fan. “Adapted poling to break the nonlinear efficiency limit in nanophotonic lithium niobate waveguides”. In: *Nature Nanotechnology* 19.1 (2024), pp. 44–50.
- [6] Tom Vandekerckhove, Tom Vanackere, Jasper De Witte, Günther Roelkens, Stéphane Clemmen, and Bart Kuyken. “Deterministic Phase-Matching of Micro-Transfer-Printed Periodically-Poled Lithium Niobate Waveguides”. In: *CLEO: Science and Innovations*. Optica Publishing Group. 2024, STh3F–5.
- [7] Xian Zhang, Xiaoyue Liu, Lin Liu, Ya Han, Heyun Tan, Liu Liu, Zhongjin Lin, Siyuan Yu, Ruijun Wang, and Xinlun Cai. “Heterogeneous integration of III–V semiconductor lasers on thin-film lithium niobate platform by wafer bonding”. In: *Applied Physics Letters* 122.8 (2023).
- [8] Theodore J Morin, Jonathan Peters, Mingxiao Li, Joel Guo, Yating Wan, Chao Xiang, and John E Bowers. “Coprocesed heterogeneous near-infrared lasers on thin-film lithium niobate”. In: *Optics Letters* 49.5 (2024), pp. 1197–1200.
- [9] Siddhartha Ghosh, Siva Yegnanarayanan, Dave Kharas, Matthew Ricci, Jason J Plant, and Paul W Juodawlkis. “Wafer-scale heterogeneous integration of thin film lithium niobate on silicon-nitride photonic integrated circuits with low loss bonding interfaces”. In: *Optics Express* 31.7 (2023), pp. 12005–12015.
- [10] Huangpu Han, Shuangchen Ruan, and Bingxi Xiang. “Heterogeneously integrated photonics based on thin film lithium niobate platform”. In: *Laser & Photonics Reviews* 19.1 (2025), p. 2400649.
- [11] Tom Vanackere, Tom Vandekerckhove, Maximilien Billet, Ying Tan, Margot Niels, Tingting Zhai, Antonietta Parracino, Valeria Bonito, Jorik Withoutck, Günther Roelkens, et al. “Towards scalable heterogeneous integration of thin-film lithium niobate on silicon photonics using micro-transfer printing”. In: *Integrated Photonics Platforms III*. Vol. 13012. SPIE. 2024, pp. 58–62.
- [12] Gordon HY Li, Midya Parto, Jinhao Ge, Qing-Xin Ji, Maodong Gao, Yan Yu, **James Williams**, Robert M Gray, Christian R Leefmans, Nicolas Englebert, et al. “All-optical computing with beyond 100-GHz clock rates”. In: *arXiv preprint arXiv:2501.05756* (2025).
- [13] Qiushi Guo, Ryoto Sekine, Luis Ledezma, Rajveer Nehra, Devin J Dean, Arkadev Roy, Robert M Gray, Saman Jahani, and Alireza Marandi. “Femtojoule femtosecond all-optical switching in lithium niobate nanophotonics”. In: *Nature Photonics* 16.9 (2022), pp. 625–631.